# Synthesis and Characterization of Graphene and Graphitized Nanocarbons

# グラフェンおよび黒鉛化ナノカーボンの合成と評価

**Balaram Paudel Jaisi**

**A thesis submitted to the Graduate School of Engineering for the acquisition of the Doctoral Degree of Engineering**

**Department of Physical Science and Engineering**

**Nagoya Institute of Technology**

**Japan**

**Supervisor: Prof. Dr. Masaki Tanemura**

**March, 2021**

***Dedicated to my beloved parents, teachers friends, brothers, wife and son!***

# Declaration

Here I confirm that the work discussed in this thesis is my own. Where I have consulted the work of others, it has been clearly stated.

# Abstract

The world today is progressing day by day in every aspect that make our life smarter and easier by one or more ways. One major aspect that directly inhibits our living is the information technology based on the electronics. With advancing thoughts and lifestyle, the search of new materials to continue the pace of this advancement is also being critical. As the era of silicon based electronics technology is in the verge of its peak performance, the exploration of these new materials becomes more essential. Graphene and other graphitized nanocarbons like carbon nanotubes (CNTs) and carbon nanofibers (CNFs) can be significant for this, due to their promising properties and their potential applications. With the introduction of chemical vapor deposition (CVD), scalable synthesis of these novel materials is widely increasing. But the presence of graphene grain boundaries in the CVD graphene is a major issue to be tackled to get the full electrical output in this material. In this work, this issue is tackled by tuning the growth from anisotropic to isotropic, and also the other graphitization techniques, such as direct graphitization of amorphous carbons, are dealt with to overcome the costly and crucial CVD process.

Chapter 1 includes the introduction to the novel material graphene, the recent progress in its synthesis techniques, its properties and the potential applications. It also includes the brief explanation to the synthesis, properties, applications and the graphitization techniques of amorphous nanocarbons in the form of CNFs.

Chapter 2 briefly explains the methodology adopted in the synthesis and characterization of graphene and CNFs with the brief introduction of the materials and devices used during this study.

Chapter 3 introduces the unique technique in the solid source CVD system to tune the graphene growth into anisotropic and isotropic. Controlling the isotropic and anisotropic graphene growth in a CVD process is a critical aspect to understand the growth dynamics for synthesizing large-area single crystals. The effect of carrier gas flow rate and controllability on isotropic and anisotropic graphene growth was established using a solid carbon source for atmospheric pressure CVD method. It was found that the idea not only tuned the graphene growth process but also increased the growth rate of isotropic crystals by about 10 times than that of anisotropic crystals without hindering the graphene quality. This understanding of the growth rate of round and hexagonal-shaped crystals can be essential to achieve faster growth of large single crystals to avoid the degradation of electrical properties of graphene due to the presence of graphene grain boundaries.

Chapter 4 discusses briefly with the growth of Mo included CNFs (Mo-CNFs) and graphitization of amorphous carbon in the form of CNFs under the catalysis of Mo during Joule heating in in situ transmission electron microscopy (TEM) processing. For the fabrication of graphene-based nano-scale interconnects, precise control over their position and proper nanoscale soldering are essential. Compared to metals like Cu, Mo is less subjected to electromigration and brittleness, making it suitable for high temperature electronics. Amorphous CNFs were effectively found to be converted to highly crystalline few-layered graphene during the electromigration of Mo nanoparticles (NPs). It was also found that during the graphene formation process, agglomerated Mo particles can be effectively channeled to the end of graphene by voltage-driven electromigration and acted as a soldering agent, providing the prospect of the further exploration of Mo as a nanoscale soldering material. This work explored the double role of Mo: As a catalyst for graphene synthesis and as a soldering material.

Chapter 5 explores the use of low melting point metal Ga in the synthesis of Ga incorporated CNFs and their consecutive graphitization by Joule heating during in situ TEM as well as under

normal vacuum annealing. For the first time, the graphitization temperature was explored to be about 600 $^{o}$C for the material system of the mixture of Ga NPs and amorphous carbon matrix. Increasing the temperature, agglomeration and evaporation of Ga NPs took place together with the graphitization at the periphery of Ga NPs at the surface region. At the same time, in-situ TEM processing led to the accelerated increase in electrical conductivity with the structural change from amorphous to graphitization. This combination of the in-situ and ex-situ TEM observations is considered as a lead step to understand deeper the graphitization process and provide the information in nanoscale.

Chapter 6 summarizes the whole work of my study and explores the future prospects.

# Acknowledgement

Learning in fact is a never ending process and is inherited to one from wide variety of people and throughout the life. There are several people who directly or indirectly provide continuous or instantaneous support in my Ph. D. research. So, I want to express my humble acknowledgement to all of them whose names may not be tabulated in this acknowledgement.

While remembering with names, I want to mention my academic supervisor, Professor **Masaki Tanemura** as my first and the foremost source of inspiration. His continuous guidance, advice, parental support and supervision helped not only to complete my research but also sharpened my level of knowledge to generate the new ideas and methodologies. Once again, I heartily thank to Professor **Tanemura** for providing me the scientific vision and molding me a responsible and dedicated researcher.

Then my sincere thanks go to my Co-supervisor, Associate Professor **Golap Kalita** for his continuous guidance and inspirations throughout my Ph. D. tenure. The direction to perform the experimental research and the direct support provided by him in academic writing became the main pillars for the acquisition of my Ph. D.

I am extremely indebted to Professor **Tetsuo Soga** and Professor **Toshio Kawahara** for their valuable comments and suggestions in reviewing my thesis. Their valuable time provided for the correction and the improvement of this thesis will be always remembered with due respect.

I would like to express my sincere thanks to Dr. **Kamal Prasad Sharma** and Dr. **Subash Sharma** for their continuous support and tutorials throughout my Ph. D. My sincere thanks also go to Dr. Rakesh Mahyabanshi, Dr. Mona Araby Ibrahim, Dr. Mohammad Saufi Bin Roshmi, Dr. Ritesh Vishwakarma, Dr. Remi Pappon, Dr. Munisamy Subramaniam, Dr. Chisato Takahashi, Dr. Yazid Yaakob, Dr. Amr Attia Abuelwafa, Dr. Mohammad Emre Ayhan, Mrs.

Sahar Elnobi, Mr. Pradeep Desai, Mr. Ajinkya Ranade, Mrs. Aliza Khaniya Sharma, Mr. Bal Singh Chaudhari, Mr. Kodai Ogawa, Mr. Hiroyuki Ogura, Mr. Kazunari Takahashi, Mr. Shoya Matsuno, Mr. Kento Oyamada, Mr. Takuma Shibata, Mr. Testuya Osugi, Mr. Yuki Kato, Miss Hikaru Ozeki, Mr. Takumi Yoshida, Mr. Ryoichi Kizu, Mr. Shinsuke Ozeki, Mr. Takuya Furunaga, Mr. Yuya Kashiwagi, Mr. Ryoji Miyachi, Mr. Masaki Kimura and all of my senior and junior lab mates for their valuable suggestions and methodological instructions to handle the different devices. After all, I can't forget the suggestions and instructions acquired from Mrs. Yoshimi Kato and Miss Norimi Yamashita while selecting the different courses and official registrations.

My dedicated thanks go to my parents, Mr. **Hari Prasad Paudel Jaisi** and Mrs. **Murali Paudel** for their life long supports and appreciations in my study and also to my uncle, aunt, brothers and sisters for their continuous appreciations.

At last, I want to indebt my sincere thanks to my lovely wife Mrs. **Shobha Sapkota Paudel** for her selfless support in my work and my son **Pranaya Paudel** for refreshing me every time with his smiles and childish behavior.

# Table of Contents

# Chapter 1

# Introduction

The world today is advancing itself day by day in every field. Referring to the electronics technology, probably it's the area which is being advanced most rapidly. Back to the days of late 19$^{th}$ and early 20$^{th}$ century, the vacuum tubes were invented by John Ambrose Fleming in 1904 based on the principle of thermionic emission.[1] The first computer, the best representative of which viz. ENIAC (Electronic Numerical Integrator And Computer -1946 AD) was made using these vacuum tubes (17468 vacuum tubes weighing 27 metric tons and occupying the space of about 200 square meters). That was of course of very large occupying the space of large room rather than their sizes at present that we can even adjust them in our pockets.[2,3] But the invention itself could be taken as the first step of the advancement of the present electronic technology. It was essential to search for such a technology that could occupy as far as little space and could run with its least power. So, based on the semiconductor as a basic unit, the transistors were invented which could be employed as a rectifier, oscillator and for other purposes for which the vacuum tubes were ordinarily used.[4] For their researches on the semiconductors and their discovery of the transistor effect, Bardeen, Brattain and Schottky were jointly awarded with the Nobel prize in Physics in 1956. According to Gordon E. Moore viz. Moore's law, in order to maintain the advancement of present solid electronics, the number of transistors per chips should be doubled in nearly every two years which is possible either by increasing the number of transistors per chips or by shrinking the size of each transistor.[5,6] The concept of integrated circuitry on the semiconductor chips nearly followed the pace of Moore's prediction for about the five decades of its prediction. However, the limit of atomic size starts to create a problem when the separation of neighboring transistors in an integrated chip comes

in the range of about 10 nm or less with the effect of quantum tunneling creating the problem of thermal dissipation in the space of nanoscales.

The silicon based technology is in its verge of suspension physically due to its limitations of speed and density, design complexity, non-recurring nature and high cost, and most evidently of its power consumption and heat dissipation.[7] Although the attempts are being made within the silicon technology like the researches on the development of quantum computers, molecular computers and by other ways like the development of optical computers and DNA computers but none of these have such significant evidence to replace this conventional silicon technology. So, to keep the pace of the demands of future technology, the use of one or more applicable novel materials is being must in the field of electronics.

The discovery of carbon based nanomaterials like the zero dimensional (0D) hollow carbon sphere viz. $C_{60}$ buckyballs or fullerene in 1985[8] and one dimensional (1D) extended hollow cylindrical carbon viz. carbon nanotubes (CNTs) in 1991[9] opened a doorway for the consideration of existence of their two-dimensional (2D) counterpart viz. graphene which was initially supposed to be thermodynamically unstable and couldn't exist in nature.[10] But, almost a century later that of the discovery of electron, Andre Geim realized the necessity of a single atomic layered metal with very high induced carrier concentration for field effect property on metals. The idea led the ground breaking concept that graphene, the single layered semi metal could exist and could be thermodynamically stable in the ambient conditions.[11] The discovery of graphene in 2004 not only solved the problem of the field effect property on metal but also became the milestone for the discovery of hundreds of other 2D materials.[12] Among the list, Graphene, hexagonal boron nitride (h-BN) and transition metal dichalcogenides (TMDCs like $MoS_2$, $WS_2$ etc.) are realized as a conductor, insulator and semiconductors respectively.[13,14]

## 1.1 Carbon and its allotropes

Carbon, an element with atomic number 6 and mass number 12 is placed in 2$^{nd}$ period and 4$^{th}$ group in modern periodic table. The word carbon itself is derived from the Latin derivative 'carbo' which is primarily meant to charcoal. With its four valence electrons, it can form varieties of compounds with other metallic as well as non-metallic elements and can also bond with other carbon atoms to exist in different physical forms which is known as allotropy. Diamond, the strongest crystal and graphite, the one of the best lubricants are two crystalline allotropes of carbon known from a long time to human society. In diamond, the four valence electrons of carbon bond with other four carbon atoms leaving no electrons to be free making it a bad conductor of electricity and giving it a tetrahedral crystalline structure. On the other hand, in graphite, out of four valence electrons, only three get bonded with other three carbon atoms in hexagonal pattern leaving one electron free which provides it a good electrical conductivity.[15,16] Several hexagonal layers of carbon atoms in a graphite crystal attach to each other with weak Vander Waal's interaction providing a slippery nature. Charcoal, black carbon etc. are some amorphous forms of carbon.

Although the use of carbon in different forms is as old as the human civilization, its use in the Avogadro's definition of mole in 18$^{th}$ century and being as the backbone of the molecules in organic compounds shows its versatile nature.[17] Its unique ability to form robust covalent bond with other carbon atoms in different hybridized states or with other nonmetallic elements enables it to form a wide range of structures, from small molecule to a long chain called polymerization. The primary nanoallotropes of carbon include mainly two types of covalent bonds between the C atoms, first the graphenic nanostructures which primarily consist of $sp^2$ hybridization like in 0D onion like C-nanospheres, fullerenes and carbon dots, 1D CNTs and nanohorns, and 2D graphene, whereas the second group consists of both the $sp^2$ and $sp^3$ C atoms like in nanodiamond. **Fig. 1.1** illustrates the structure of different nanoallotropes of

carbon.[18] Besides these too, there are another category of carbon nanoallotropes which resemble almost with the CNTs called carbon nanofibers (CNFs) and exist both in graphitic and amorphous forms.

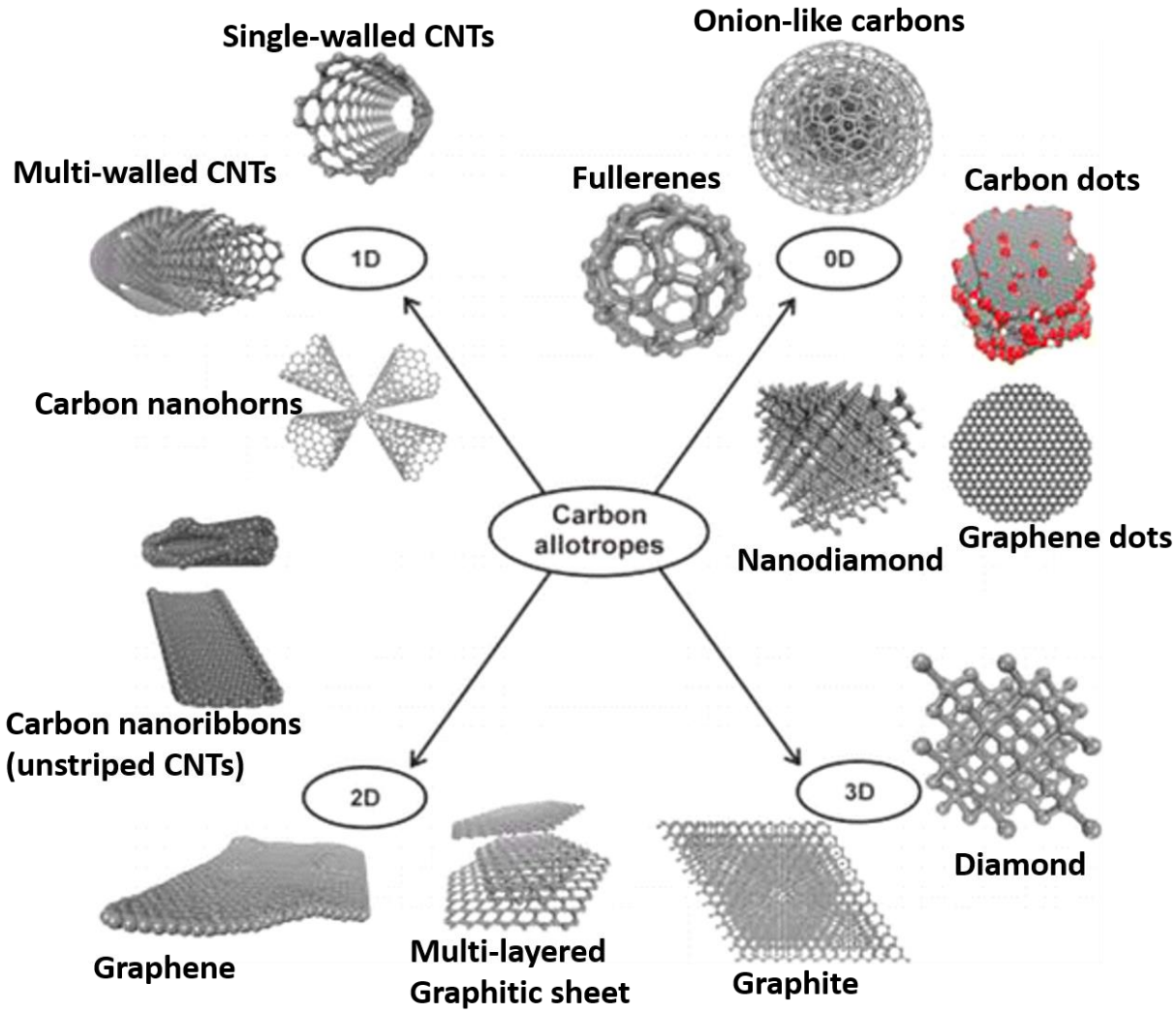


**Figure 1.1** The geometrical illustration of various allotropes (nanoallotropes) of carbon.[18]

## 1.2. Graphene

The word graphene refers to the crystalline modification of carbon in which the suffix –ene is attached to resemble the polycyclic aromatic hydrocarbons like naphthalene, anthracene, corocene, ovalene and graphene for a single layer of carbon atoms of the graphitic structure as

the final member of the infinite size of this series.[19] More precisely, graphene is a single atomically thick sheet of hexagonally arranged, $sp^2$ bonded carbon atoms capable of free suspension or can adhere to a foreign substrate.[20] In fact, graphene is a single layer of 3D graphite when flattened forms graphene layer, when rolled to a cylindrical structure forms CNTs and when wrapped in spherical structure forms fullerenes.[21] **Fig. 1.2** illustrates how a peeled layer of graphene from graphite can form the fullerene, CNT and graphite convincing itself as the mother of these materials.

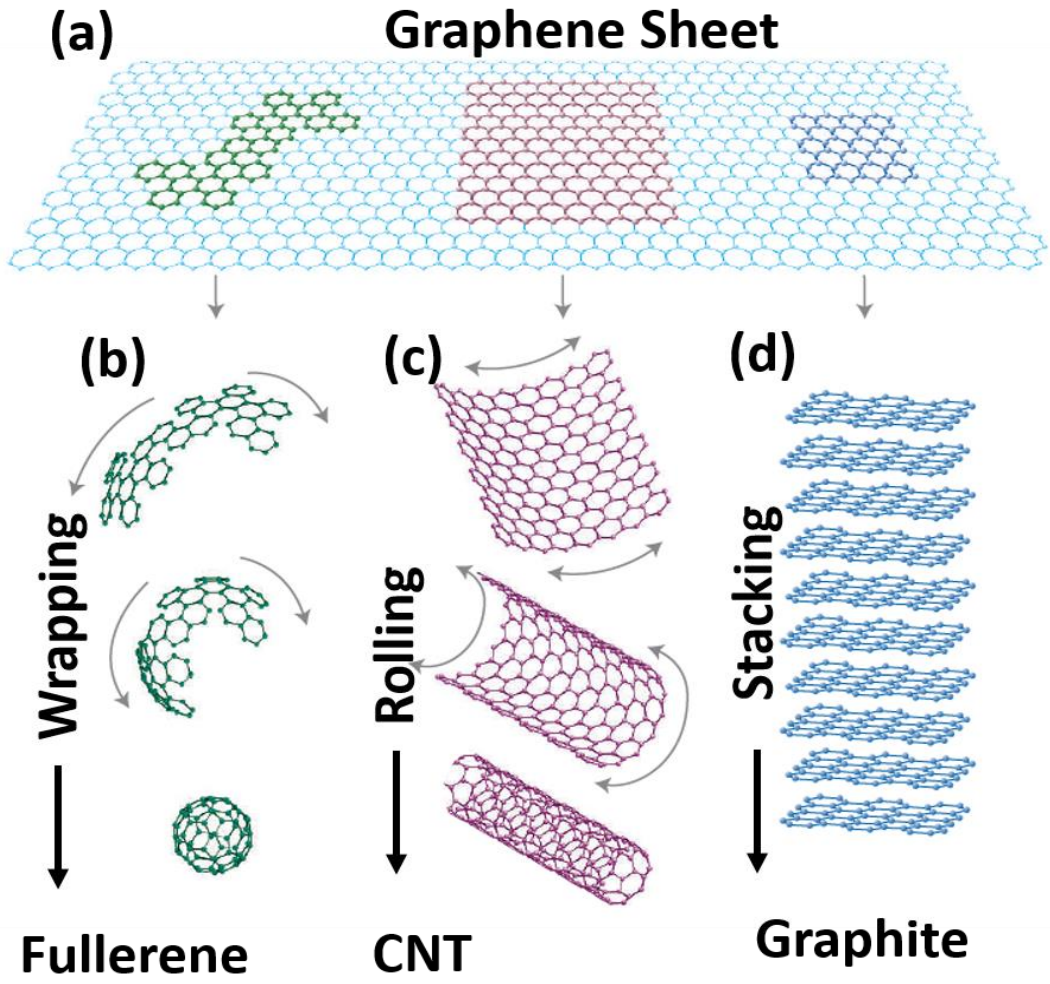


**Figure 1.2** Schematic illustration to show how a (a) graphene layer can be (b) wrapped into 0D fullerene, (c) rolled to 1D CNT and (d) stacked into 3D graphite.[21]

### 1.2.1 Graphene synthesis techniques

#### 1.2.1.1 Mechanical exfoliation

This is the technique first used by A. K. Geim and K. S. Novoselov which turned itself into the discovery of the novel material graphene. They simply used a sticky tape on a highly ordered pyrolytic graphite (HOPG) and the attached flake in the tape was repeatedly exfoliated and finally attached to a viable substrate like $SiO_2$.[11] (see **Fig. 1.3(a))** It adhered several multilayered graphene flakes on the $SiO_2$ substrate, some of which were even of monolayer composition and size ranging up to few of tens of micrometers. They significantly measured the thickness of the stacked layers which even approached to nearly 0.4 nm which was the milestone in the discovery of the existence of 2D material graphene. Prior to them, the attempt to show the existence of this novel material was also done by R. S. Ruoff et al. in 1999 by somewhat different approach but not succeeded.[22] Though the extent of size of monolayer graphene with this technique was limited to micron size during its introduction, several other attempts showed the size extended to the millimeter and sub-centimeter scale required for the device fabrication.[23,24] Due to its simplicity and superior in quality, the technique is being used in graphene production for the research purposes even the extension of flake size is difficult as well as non-recurring.

#### 1.2.1.2 Liquid phase exfoliations

With the term itself, it refers to the exfoliation of HOPG in some special solvents which minimize the interfacial tensions between the liquid and graphene flakes. This technique can be completed generally in three steps viz. i) graphite dispersion in the solvent, ii) exfoliation and iii) purification.[25] In this technique, HOPG is simply dispersed in the chemical solvents like N- methyl pyrrolidone (NMP), dimethyl formamide (DMF), benzyl benzoate, γ-

butyrolactone (GBL), acetone, chloroform, isopropanol, etc. followed by ultra-sonication to provide the homogeneity of the exfoliated graphite particles in the solvent (see **Fig. 1.3(b)**). The solution is then purified or concentrated by the techniques like centrifugation which also separates the flakes in terms of layer numbers.[26,27] With this method, the graphene flakes produced are of the dimension ranging from few nanometers to few micrometers suspended in the liquid solvent. The fluid then can be deposited on viable substrates like $SiO_2$ by spin coating to get the graphene flakes on the substrate for various characterizations. Being scalable and economic, thus produced graphene can be used in composite materials, conductive inks etc.

#### 1.2.1.3 Reduction of graphene oxide (GO)

Besides the general dispersion, the liquid phase exfoliation technique can be applied to get the GO by treating HOPG in the chemical mixtures like potassium chlorate ($KClO_3$) and concentrated nitric acid ($HNO_3$), $KClO_3$ and concentrated sulphuric acid ($H_2SO_4$), and mixture of potassium permanganate ($KMnO_4$), sodium nitrate ($NaNO_3$) and $H_2SO_4$ etc.[28-30] The GO is then reduced into pristine graphene by treating with the chemicals like hydrazine, hydrides, p-phenylene, hydroquinone and also by dehydration and thermal reduction.[25] This method is an economic and efficient way for the large scale graphene production though the limitations arise due to the use of hazardous chemicals during the process.

#### 1.2.1.4 Epitaxial growth on silicon carbide (SiC)

The techniques of graphene synthesis discussed earlier themselves start with some pre-existing graphitic materials and look like the deposition on a viable substrate. Such methods are termed as top-down approach for graphene synthesis and lack with the precise configuration of the graphene.[31] The techniques like epitaxial growth on SiC and chemical vapor deposition

are termed as the bottom-up approaches for the graphene synthesis and are useful in the graphene synthesis with precise configuration and orientation.

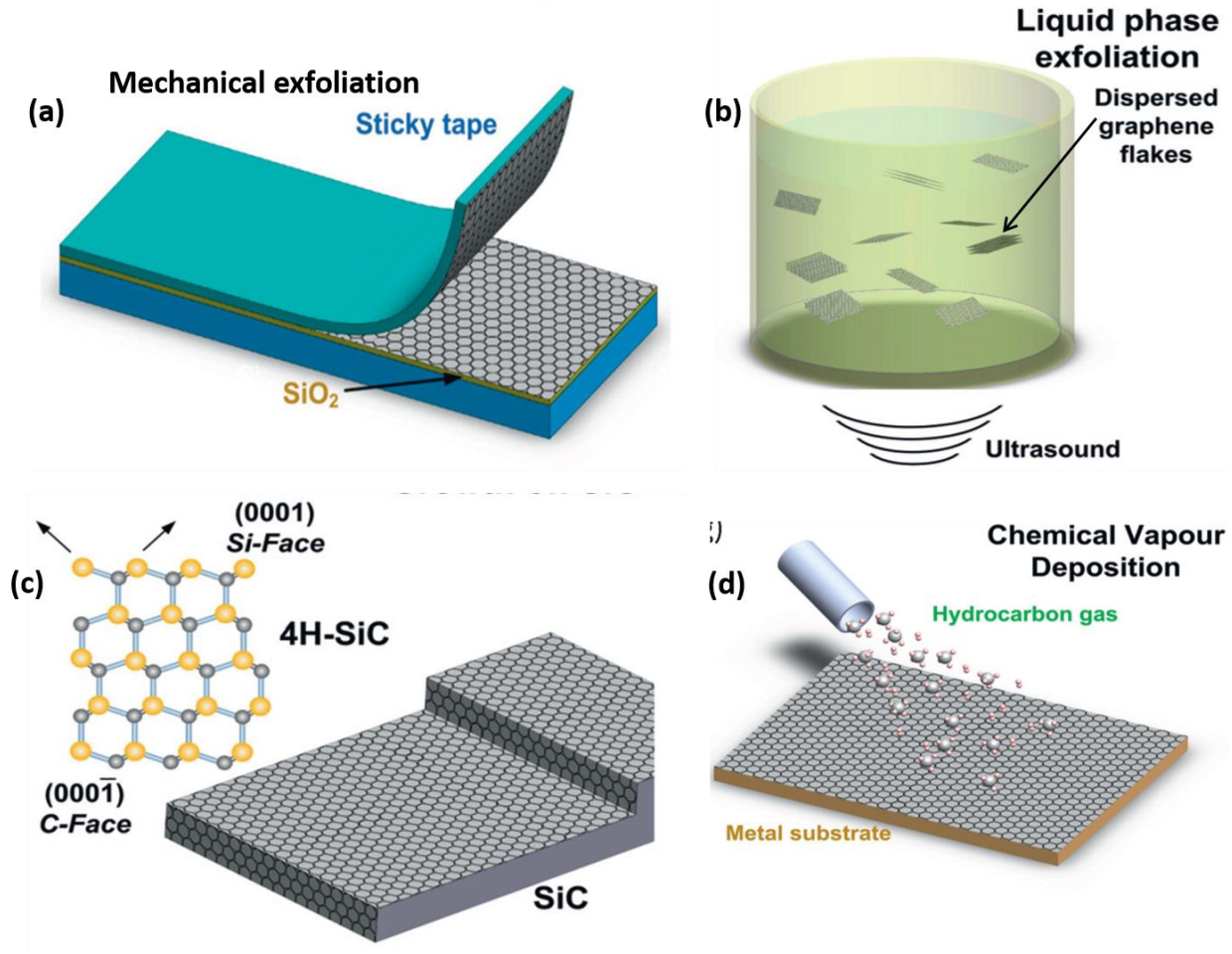


**Figure 1.3** Graphical illustration to show different graphene synthesis techniques (a) Mechanical exfoliation technique, (b) Liquid phase exfoliation technique, (c) Epitaxial growth on SiC and (d) Chemical vapor deposition technique.[25]

This epitaxial growth on SiC method comprises the heating of SiC surface to a high temperature (>1000 $^{o}$C) either in vacuum or in the supply of inert gases like Argon.[32] The differences in the vapor pressure of C and Si in SiC leads the evaporation of the Si at the surface leaving behind the carbon atoms and those carbon atoms rearrange themselves in hexagonal lattice as graphene (see **Fig. 1.3(c)**).[33,34] The epitaxial graphene grown on Si-terminated SiC (0001) is quite epitaxial while that on C-terminated SiC (000$\bar{1}$) is with many rotational domains

or even with sprouts nanotubes which account for the low degree of order of few layer graphene on this surface.[34,35] Though the graphene flakes can be grown with this technique are limited up to centimeter scale, the transfer free graphene can be obtained directly on the Si substrate makes it easy for the application in power electronics.

#### 1.2.1.5 Chemical Vapor Deposition (CVD)

It is the technique of deposition of thin film on a catalytic surface in which the surface called the substrate is exposed to the volatile materials called precursors generally at the high temperature. It is considered as the most convincing method for the controlled growth of uniform and large area graphene film. Generally, the transition metals like Cu, Ni, Ru, Co, Pt, Ru, Pd etc.[36-42] are used as the substrate under the exposer of thermally decomposed species of carbonaceous sources (either gases, liquids or solids )[43-46] under high temperature, at ambient or low pressure, in the supply of one or both carrier gases $H_2$ and Ar (see **Fig. 1.3(d)**).

M. Losurdo et al.[47] and C. M. Seah et al.[48] explained the mechanism of CVD graphene formation on the metals Ni and Cu. The carbon solubility in Ni is very high than compared to that in Cu which leads bulk mediated growth in Ni whereas surface mediated growth in Cu. The graphitization is completed in following steps i) in-diffusion of H atoms in the catalytic surface and chemisorption of hydrocarbon radicals ($CH_4$), ii) dissociation of the chemisorbed $CH_4$ radical to form $CH_3$ radical by dehydrogenation, iii) dissolution of carbon adatoms in the metal bulk, iv) nucleation of graphitization and v) segregation to form the graphene.[47,48] This mechanism of graphitization is illustrated in **Fig. 1.4**.

This work mainly focuses on the CVD synthesis of graphene on polycrystalline Cu substrate using solid hydrocarbons as precursor. The actual method of synthesis is described in detail in chapter 2 and chapter 3. However, the lower carbon solubility in copper and its mild catalytic activity makes it a dominant substrate to grow large area monolayer graphene film in

meter scale with a roll-to roll production technique[49] as well as makes the growth self-limiting to obtain high quality and uniform monolayer graphene.[43,50] Furthermore, liquid Cu surface as a catalytic substrate for graphene growth is established for the growth of graphene single crystals in various shapes by varying the composition and ratio of carrier gases Ar and $H_2$.[51]

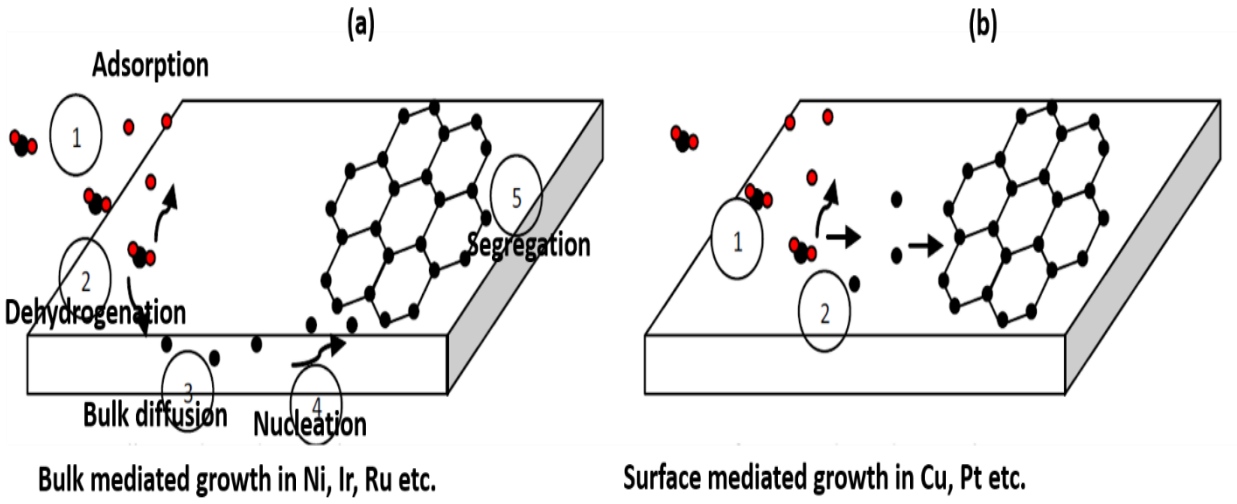


**Figure 1.4** Graphical illustration of mechanism of graphene formation during the CVD process (a) the bulk mediated growth and (b) the surface mediated growth.[47,48]

### 1.2.2 Properties of Graphene

#### 1.2.2.1 Mechanical properties

Graphene is one of the strongest materials known which is considered to be more than 300 times stronger than stainless steel. It has tremendous elasticity with Young's modulus approaches to 1 TPa and the fracture strength to be 130 GPa, much higher than that of any other materials reported.[52] This behavior of graphene is found to be helpful to reinforce the strength of other materials in the composite materials with graphene.[53,54]

#### 1.2.2.2 Thermal properties

Graphene has enormous thermal conductivity at room temperature which is even higher than that of copper.[55] Balandin et al. measured the thermal conductivity of the suspended single layer graphene at room temperature approximately to 5000 $Wm^{-1}K^{-1}$.[56]

#### 1.2.2.3 Optical properties

Graphene is almost transparent with the coefficient of transmittance as 0.977 for the optically visible light independent to the frequency.[57] Optical transparency may be one of the best part of graphene for its potential application as in the manufacture of transparent and flexible electrodes in photodetectors, solar cells and touch screen based displays.[58,59]

#### 1.2.2.4 Electronic properties

Graphene is chemically inert due to its strong $sp^2$ hybridized honeycomb structure.[52] In $sp^2$ hybridization, of the four valence electrons of C atom residing in the 2s and 2p ($p_x$, $p_y$ and $p_z$) orbitals, the one s-orbital and two p-orbital interact in the influence of those of other three C atoms forming covalent σ-bonds. The next p-orbital perpendicular to this hybridized plane provide weak Van der Waal's interaction between the different layers in a bulk graphite and contributes for the π-bond. In tight-binding approach, the C-C distance between the neighboring atoms is 1.42 Å which leads to a triangular lattice with two atoms per unit cell (**Fig. 1.5(a)**) and lattice constant 2.46 Å. The two points K and K' at the corners of graphene Brillouin zone (**Fig. 1.5(b)**) are named as the Dirac points (**Fig. 1.5(c)**).[60,61]

The electronic dispersion diagram in **Fig. 1.5(c)** clearly shows the conduction band and the valence band touch each other at six Dirac points (zero band gap) rising the Dirac cones

similar to that for the mass less particles leading the relativistic behavior to the electrons near the Dirac points resulting into the high mobility in graphene.[61] Experimentally, Bolotin et al.[62] and Du et al.[63] measured the carrier mobility in suspended graphene approaching to the high value of 200,000 $cm^2V^{-1}s^{-1}$. In addition to this extreme mobility, graphene possesses high carrier concentration upto $10^{13}$ $cm^{-2}$ with simultaneously tuning between electrons and holes,[11] quantum hall effect,[64] Casimir effect,[65] Klein tunneling effect,[66] and the breakdown of the adiabatic Born-Oppenheimer approximation.[67]

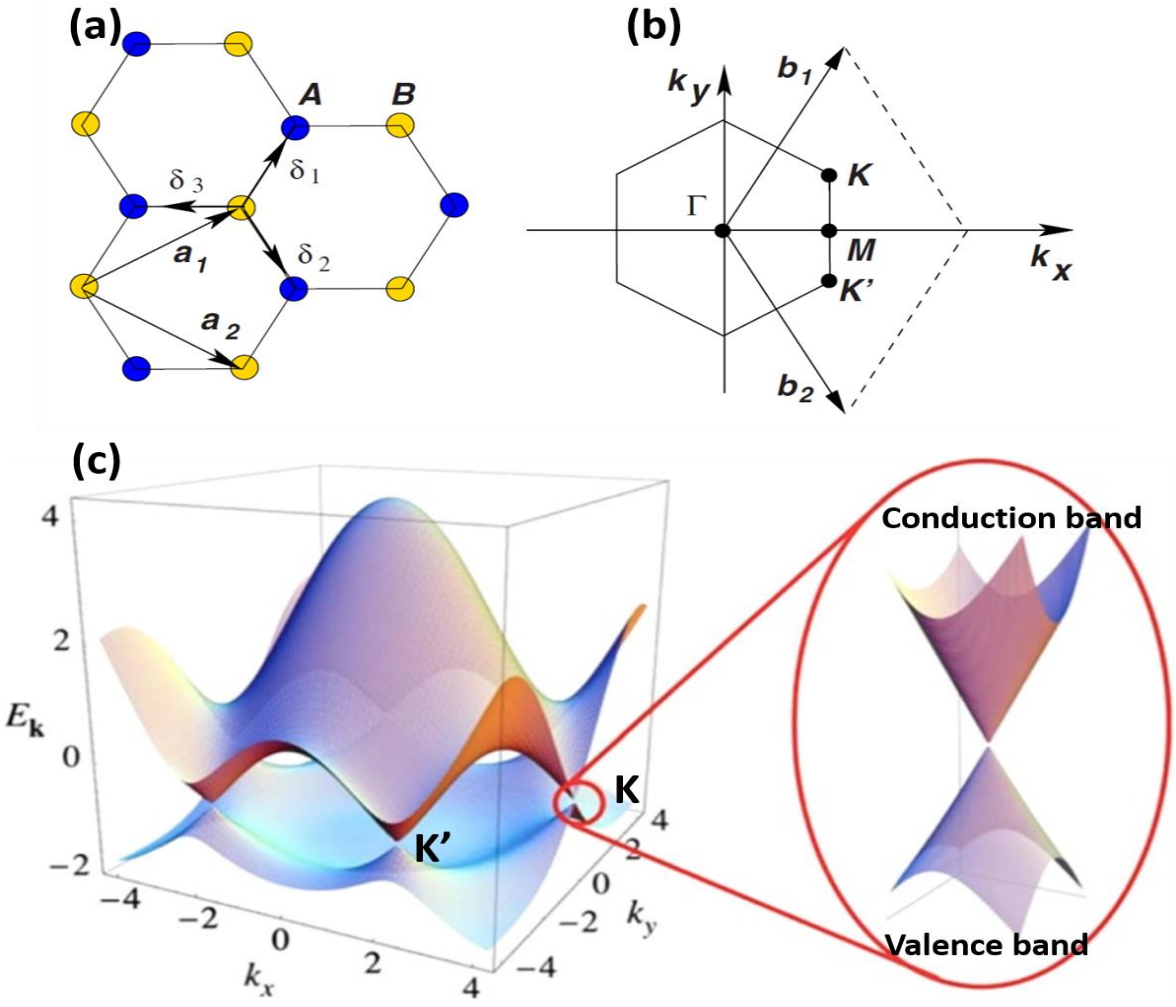


**Figure 1.5** (a) Lattice structure of graphene with $\boldsymbol{\delta}_i$, (i = 1, 2, 3) being the nearest neighbor vectors ($|\boldsymbol{\delta}_i| = 1.42$ Å) and $\mathbf{a}_1$, $\mathbf{a}_2$ being the lattice unit vectors ($|\mathbf{a}| = 2.46$ Å) (b) the corresponding Brillouin zone with K and K' being the location of Dirac cones and (c) electronic dispersion in honeycomb lattice with the energy band close to Dirac point enlarged.[61]

### 1.2.3 Potential applications of graphene

Based on the novel properties of graphene mentioned in the chapter 1.2.2, graphene has many potentials to be applied in various disciplines of science. Among those countless potential applications, some are tabulated in the **Table 1.1**.

**Table 1.1** Some observed applications of graphene

| **Related field** | **Potential Applications with explanation** |
|---|---|
| Electronics | Flexible and transparent electrodes and displays.[59,68,69]- With highly elastic, transparent and high carrier mobility.<br>Ultra-fast transistors (100 GHz).[70]- Due to the atomic dimensions and high carrier mobility. |
| Medicines | Drug delivery system in the treatment of cancers.[71] - Due to its chemical inertness, nanodimensions and easily detectable. |
| Light processing | Ultrathin lenses with 3D subwavelength focusing.[72] – Due to its high transparency, flexibility. |
| Energy and Storage | Photovoltaics (solar cells).[73] –Due to high flexibility, transparency and conductivity.<br>Super capacitors with specific capacitance 135 $Fg^{-1}$.[74] – Due to its very high surface area to mass ratio, high conductivity leading wide voltage performance range. |

The applications shown in **Table 1.1** are only a few among the countless applications of graphene which are experimentally shown. In addition to them, graphene with its hardest nature, can be used as anti-corrosion coating in aviation and mechanical sensors. Its ultra-high conductivity and surface to mass ratio provides potential applications in memory devices, and the high thermal conductivity can be utilized in preparing interconnects in the thermal and electrical devices.

## 1.3 Direct graphitization of nanocarbons

In chapter 1.2.1, the various techniques of graphene synthesis were discussed. Those are the methods in which graphene is synthesized either by the exfoliation from a bulk (graphite) or by the application of large amount of heat (high temperature) on some hydrocarbons under the catalysis of metals on those metal surfaces. As discussed earlier, the exfoliation techniques result into the synthesis of short-range graphene usually in micrometer scale. Furthermore, the exfoliation techniques seem to be easier but are not recurrent specially for the formation of monolayer graphene. On the other hand, the graphene synthesis with CVD process leads in the large scale production,[49,59] but the CVD graphene before its utilization should go under the tedious transfer process on the viable substrates.[75] During this transfer process, there is not only the probability of mechanical damage but also the degradation of its quality due to the contamination arose by the chemicals used in the transfer process.

In order to get rid of this limitation of CVD graphene caused due to the transfer process, attempts were made for the direct growth of graphene on the dielectric substrate without the metallic catalyst either through the thermal CVD[76,77] or by plasma enhanced CVD (PECVD).[78,79] With this initiation, though, in some cases, the temperature of synthesis is decreased tuning the growth towards low temperature growth,[76] the monolayer quality and uniformity to the large area synthesis is not maintained. Contrary to these CVD processes, Hirano et al.[80] and Vishwakarma et al.[81] showed the synthesis of transfer free graphene directly on the $SiO_2$ substrate by the direct graphitization of amorphous carbon (αC) with simple annealing under the catalytic effect of thin layer of Co and Sn respectively. They easily eliminated the metallic layer with simple chemical etching to get the graphene on the $SiO_2$ substrate.

Transmission electron microscopy (TEM) is the technique used in the characterization of nanoparticles either thin enough to transmit the electron beam or being suspended so that they can be observed from a side. To establish these methods of direct graphitization of αC, the graphitization mechanism is to be understood first and for this propose, TEM is the best option. In this work, the graphitization mechanism is being explored in nanoscale using TEM starting with the αC in the form of carbon nanofibers (CNFs) and cones synthesized using the ion beam bombardment method at room temperature and subsequently graphene layers with long range (up to micrometers) was found to be synthesized under TEM.

### 1.3.1 Fabrication of CNFs and cones

The elongated nanocarbons like CNTs and CNFs are generally synthesized using the methods like arc discharge, laser ablation and CVD which require high temperature. On the other hand, CNFs can also be directly fabricated on the tip of an AFM probe or at the edge of a thin graphite sheet even at room temperature by the bombardment of ions ($Ar^+$) which are amorphous in crystalline state and can be directly utilized for TEM study without any post treatment. The growth mechanism of these CNFs is proposed schematically in **Fig. 1.6(a)** along with SEM image of a typical CNF grown at the tip of a cantilever is shown in **Fig. 1.6(b)**.[82]

To observe the catalytic effect of different elements in the graphitization of αC, the CNFs and cones can be incorporated with the nanoparticles (NPs) of the respective elements by co-sputtering them perpendicular to the substrate during the ion beam bombardment process.

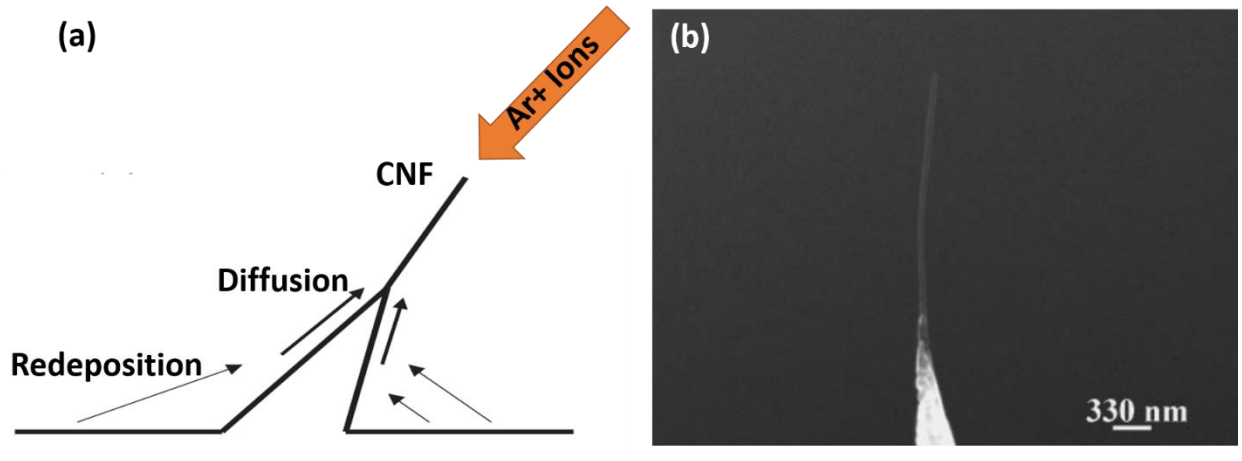


**Figure 1.6** (a) Schematic of formation mechanism of a single CNF and (b) SEM image of a typical CNF grown at the tip of a cantilever.[82]

### 1.3.2 Graphitization through Joule heating during in situ TEM

When a biasing voltage is applied across the tip of a CNF and the conducting surface of the substrate with a special arrangement inside a TEM, the resistance offered by the CNF leads the heating effect known as Joule heating. Sim et al.[83] studied the field emission (FE) from a single CNF with in situ SEM and measured a maximum FE current of 15 μA before it got damaged due to the resistive heating. The in situ processing for the FE measurement of the CNFs incorporated with the several metals like Fe,[84] Cu,[85] Ag,[86] Au,[87] and Si and Ge [88] showed not only the improvement in the FE current but also demonstrated the transformation of the metal incorporated CNFs from amorphous carbon to the bamboo like capped CNTs and thick graphene layers. This mechanism of graphitization with Joule heating is well explained in the schematics of **Fig. 1.7**.

Thus, the incorporation of foreign element during the ion beam fabrication of CNFs plays a catalytic role during graphitization. In this work, the same effect of the metals like Mo

and Ga which are otherwise studied less for this propose is explored in the field of graphene synthesis.

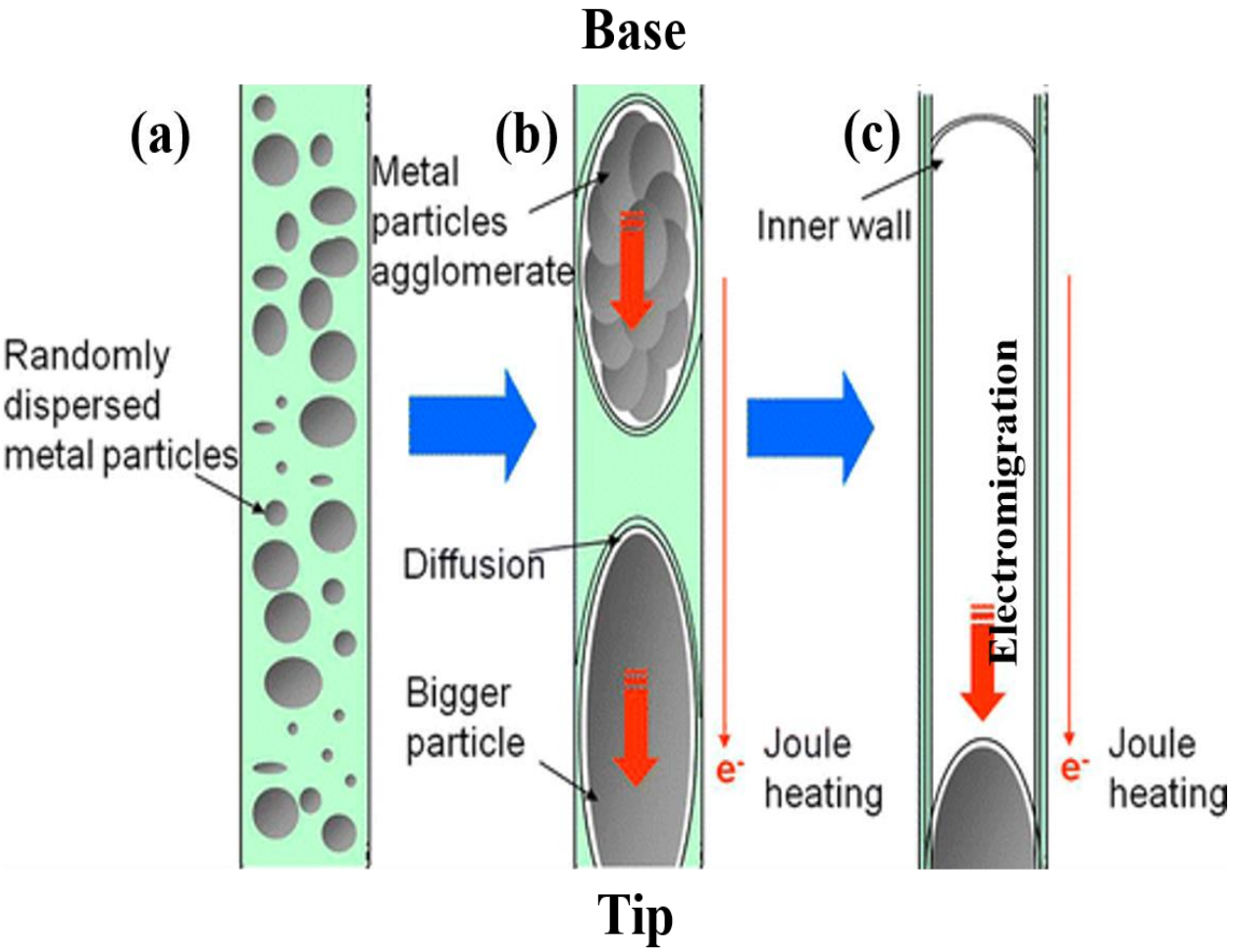


**Figure 1.7** Schematic diagram to show the formation process of bamboo-like CNT during FE process under in situ TEM. (a) Initial structure of metal incorporated CNF before FE process, (b) agglomeration of metal NPs and graphitization through C-diffusion induced by Joule heating and (c) electromigration of agglomerated metal particles forming bamboo like CNT.[84]

### 1.3.3 Graphitization on direct heating

Based on the studies done by Hirano et al.[80] and Vishwakarma et al.[81] to synthesize the graphene directly on ordinary heating of αC deposited on $SiO_2$, Araby et al.[82] followed the same route for the metal In with low melting point and observed the αC to be graphitized as

low as the temperature of 150 $^{o}$C. Prior to this, they also observed partial graphitization in the indium incorporated CNFs prepared by ion irradiation method at an energy of 1 KeV without any intentional heating. This study showed that the metals with low melting point can be promising in the graphitization of αC. In this work, the graphitization mechanism of αC under the catalysis of another low melting point metal Ga is explored though Ga has very low carbon solubility at low temperature.

### 1.4 Motivation and purpose of the thesis

Graphene, from the day of its first observance proved itself as the best alternative material in the field of electronics and several other fields pioneered by its many novel characteristics. Though, many other 2D materials are shown in existence well after the graphene, the history of nature shows that carbon nanomaterials remained always in top at least in terms of their stability, inertness and even friendly to the livestock. These features along with its recently observed novel characteristics provide an approval for graphene to be used as potential future material. However, for any material to be used by replacing its conventional counterparts, its economic synthesis in mass scale is must and cannot be avoided. This thesis is directed towards the exploration of synthesis and characterization of this novel material graphene by different techniques.

Concerning this topic of graphene synthesis, CVD is the most convincing way for the synthesis of graphene as well as other 2D materials. The graphene grain boundaries in CVD graphene are the major reason of its degraded quality in comparison to the exfoliated one which urges to large single crystal growth in CVD. In what follows, the same issue is tempted to be solved by modifying the CVD parameters so that the growth is tuned to isotropic. This tuning provides a space for the smooth stitching between the smaller isotropic crystals leading towards

the growth of larger single crystals with the same other parameters compared to its anisotropic counterparts.

Similarly, the process of direct graphitization of αC can be another way to eliminate this issue of degradation of graphene quality due to the presence of grain boundaries as long range graphene synthesis is possible through this way. Furthermore, for the scalable growth of graphene, the graphitization mechanism must be understood in nanoscale. For this, TEM can be a promising tool of characterization but it is so difficult to prepare the TEM samples with CVD graphene as well as to observe the CVD process of graphitization under a TEM. So, this thesis aims in these different processes of graphene synthesis as well as the problem of understanding the graphitization mechanism in nanoscale is challenged either by well stablished in situ FE TEM process or by observing the graphitized nanocarbons under TEM graphitized by other route like direct heating.

### 1.5 Organization of the thesis

The isotropic graphene crystals growth and the nano analysis of graphitization of nanocarbons is described in detail in this thesis.

***Chapter 1*** deals with the introduction of graphene, its recent progresses in growth, properties and utilization. In the same manner, the other nanocarbons are introduced with their synthesizing techniques and graphitization techniques. At last, the motivation and the purpose of the work is also mentioned.

***Chapter 2*** includes the brief discussion of the methods mainly followed in this work for the synthesis and characterization of the synthesized materials with the brief introduction of the various tools used for the purpose.

***Chapter 3*** emphasizes on the modification on the CVD parameters for tuning the growth mechanism into isotropic growth to achieve the faster and larger crystals in comparison to their anisotropic counterparts.

***Chapter 4*** investigates the synthesis of graphene through the synthesis of Mo-CNFs and their graphitization along with their FE characteristics under in situ TEM processing. The graphitization mechanism is analyzed in nanoscale along with the structural changes in the NPs of high melting point metal Mo is observed to investigate its application in inter connect material.

***Chapter 5*** explores more on the issue of graphene synthesis by graphitization of nanocarbons using Ga-CNFs along with their FE characteristics under in situ TEM processing. The graphitization of nanaocarbons associated with Ga-CNFs was also observed by direct heating and analyzed under the TEM. The very contrasting characteristics of Ga NPs induces some strange behavior during the graphitization process.

***Chapter 6*** summarizes the whole work and recommends the future prospect.

**References of chapter 1**


[1] Michael Alba, Vacuum Tubes: The World Before Transistors. https://www.engineering.com/ElectronicsDesign/ElectronicsDesignArticles/ArticleID/16337/Vacuum-Tubes-The-World-Before-Transistors.aspx, (accessed 19 January 2018).

[2] R. I. Scace, Electronics, https://www.britannica.com/technology/electronics/The-semiconductor-revolution, (accessed 02 June 2020).

[3] J. Han, M. Meyyappan, Introducing the Vacuum Transistor: A Device Made of Nothing, https://spectrum.ieee.org/semiconductors/devices/introducing-the-vacuum-transistor-a-device-made-of-nothing, (accessed June 23, 2014)

[4] J. Barden and W. H. Bratain, *Phys. Rev.* 1948, **74**, 230-231.

[5] G. E. Moore, *Electronics*, 1965, **38 (8),** 114-117**.**

[6] G. E. Moore, *Dig. Tech Papers Int. Solid-State Circuits Conf.*, 2003, 20-23.

[7] S. Hassan, Humaira, M. Asghar, *IEEE Second Int. Conf. on Comm. Soft and Net.*, 2010, 559-561.

[8] H. W. Kroto, A. W. Allaf and S. P. Balm, *Chem. Rev.*, 1991, **91**, 1213-1235.

[9] S. Iijima, *Nature*, 1991, **354**, 56-57.

[10] L. Landau, *Nature*, 1936, 840-841.

[11] K. S. Novoselov, A. K. Geim, S. V. Morozov, D. Jiang, Y. Zhang, S. V. Dubonos, I. V. Grigorieva and A. A. Firsov, *Science*, 2004, **306**, 666-669.

[12] E. Gibney, *Nature*, 2015, **522**, 274-276.

[13] K. F. Mak, C. Lee, J. Hone, J. Shan and T. F. Heinz, *Phys. Rev. Lett.*, 2010, **105**, 136805 (4pp).

[14] C. Tan, X. Cao, X. J. Wu, Q. He, J. Yang, X. Zhang, J. Chen, W. Zhao, S. Han, G. H. Nam, M. Sindoro and H. Zhang, *Chem. Rev.* 2017, **117**, 6225-6331.

[15] P. Delhaes, J. P. Issi, S. Bonnamy and P. Launois, in *Understanding Carbon Nanotubes*, ed. A. Loiseau, P. Launois, P. Petit, S. Roche and J. P. Salvetat, *Springer*, 2006, **677**, ch. 1, pp. 1-47.

[16] H. O. Pierson, *Handbook of Carbon, Graphite, Diamond and Fullerenes*, Noyes Pub., NJ, 1994.

[17] A. Demming, *Nanotechnol.*, 2010, **21**, 300201 (2pp).

[18] V. Georgakilas, J. A. perman, J. Tucek and R. Zboril, *Chem. Rev*., 2015, **115**, 4744-4822.

[19] H. P. Boehm, R Setton and E. Stumpp, *Pure and Appl. Chem*., 1994, **66**, 1893-1901.

[20] A. Bianco, H. M. Cheng, T. Enoki, Y. Gogotsi, R. H. Hurt, N. Koratkar, T. Kyotani, M. Monthioux, C. R. Park, J. M. D. Tascon, J. Zhang, *Carbon*, 2013, **65**, 1-6.

[21] A. K. Geim and K. S. Novoselov, *Nat. Mater*., 2007, **6**, 183-191.

[22] X. Lu, M. Yu, H. Huang and R. S. Ruoff, *Nanotechnol.*, 1999, **10**, 269-272.

[23] Y. Huang, E. Sutter, N. N. Shi, J. Zheng, T. Yang, D. Englund, H. J. Gao and P. Sutter, *ACS Nano*, 2015, **9**, 10612-10620.

[24] A. K. Geim, *Science*, 2009, **324**, 1530-1534.

[25] F. Bonaccoroso, A. Lombardo, T. Hasan, Z. Sun, L. Colombo and A. Ferrari, *Mater. Today*, 2012, **15**, 564-589.

[26] Y. Hernandez, V. Nicolosi, M. Lotya, F. M. Blighe, Z. Sun, S. De, I. T. McGovern, B. Holland, M. Byrne, Y. K. Gun'ko, J. J. Boland, P. Niraj, G. Duesberg, S. Krishnamurthy, R. Goodhue, J. Hutchison, V. Scardaci, A. C. Ferrari and J. N. Coleman, *Nat. Nanotechnol.*, 2008, **3**, 563-568.

[27] A. O'Neill, U. Khan, P. N. Nirmalraj, J. Boland and J. N. Coleman, *J. Phys. Chem. C*, 2011, **115**, 5433-5428.

[28] B. C. Brodie, *Q. J. Chem. Soc. London*, 1860, **12**, 261-268.

[29] L. Staudenmaier, *Eur. J. Inorg. Chem*., 1898, **31**, 1481-1487.

[30] W. S. Hummers and R. E. Offeman, *J. Am. Chem. Soc*., 1958, **80**, 1939 (1pp).

[31] Z. Zhang, A. Fraser, S. Ye, G. Merle and J. Barralet, *Nano Futures*, 2019, **3**, 042003 (32pp).

[32] C. Berger, Z. Song, X. Li, X. Wu, N. Brown, C. Nand, D. Mayou, T. Li, J. Hass, A.N. Marchenkov, E. H. Conrad, P. N. First and W. A. de Heer, *Science*, 2006, **312**, 1191-1196.

[33] K. V. Emtsev, A. Bostwick, K. Horn, J. Jobst, G. L. Kellogg, L. Ley, J. L. McChesney, T. Ohta, S. A. Reshanov, J. Rohrl, E. Rottenberg, A. K. Schmid, D. Waldmann, H. B. Weber and T. Seyller, *Nat. Mater.*, 2009, **8**, 203-207.

[34] K. V. Emtsev, F. Speck, T. Seyller and L. Ley, *Phys. Rev. B*, 2008, **77**, 155303 (10pp).

[35] P. N. First, W. A. de Heer, T. Seyller, C. Berger, J. A. Stroscio and J. S. Moon, *MRS Bulletin*, 2010, **35**, 296-305.

[36] A. Reina, X. Jia, J. Ho, D. Nezich, H. Son, V. Bulovic, M. S. Dresselhaus and J. Kong, *Nano Lett.*, 2009, **9**, 30-35.

[37] K. S. Kim, Y. Zhao, H. Jang, S. Y. Lee, J. M. Kim, K. S. Kim, J. H. Ahn, P. Kim, J. Y. Choi and B. H. Hong, *Nature*, 2009, **457**, 706-710.

[38] J. Coraux, A. T. N'Diaye, C. Busse and T. Michely, *Nano Lett.*, 2008, **8**, 565-570.

[39] P. W. Sutter, J. I. Flege and E. A. Sutter, *Nat. Mater.*, 2008, **7**, 406- 411.

[40] A. Varykhalov and O. Rader, *Phys. Rev. B*, 2009, **80**, 035437 (6pp).

[41] S. M. Wang, Y. H. Pei, X. Wang, Q. N. Meng, H. W. Tian, X. L. Zheng, W. T. Zheng and Y. C. Liu, *J. Phys. D: Appl. Phys.*, 2010, **43**, 455402 (6pp).

[42] P. Sutter, J. T. Sadowski and E. Sutter, *Phys. Rev. B*, 2009, **80**, 245411 (10pp).

[43] X. Li, W. Cai, J. An, S. Kim, J. Nah, D. Yang, R. Piner, A. Velamakanni, I. Jung, E. Tatuc, S. K. Banerjee, L. Colombo and R. S. Ruoff, *Science*, 2009, **324**, 1312-1314.

[44] X. Chen, P. Zhao, R. Xiang, S. Kim, J. Cha, S. Chiashi and S. Maruyama, *Carbon*, 2015, **94**, 810-815.

[45] Z. Sun, Z. Yan, J. Yao, E. Beitler, Y. Zhu and J. M. Tour, *Nature*, 2010, **468**, 549-552.

[46] S. Sharma, G. Kalita, R. Hirano, S. M. Shinde, R. Papon, H. Ohtani and M. Tanemura, *Carbon*, 2014, **72**, 66-73.

[47] M. Losurdo, M. M. Giangregorio, P. Capezzuto and G. Bruno, *Phys. Chem. Chem. Phys.*, 2011, **13**, 20836-20843.

[48] C. M. Seah, S. P. Chai and A. R. Mohamed, *Carbon*, 2014, **70**, 1-21.

[49] T. Kobayashi, M. Bando, N. Kimura, K. Shimizu, K. Kadono, N. Umezu, K. Miyahara, S. Hayazaki, S. Nagai, Y. Mizuguchi, Y. Murakami and D. Hobara, *Appl. Phys. Lett*., 2013, **102**, 023112 (4pp).

[50] P. Zhao, A. Kumamoto,, S. Kim, X. Chen, B. Hou, S. Chiashi, E. Einarsson, Y. Ikuhara and S. Maruyama, *J. Phys. Chem. C*, 2013, **117**, 10755-10763.

[51] B. Wu, D. Geng, Z. Xu, Y. Guo, L. Huang, Y. Xue, J. Chen, G. Yu and Y. Liu, *NPG Asia Mater.*, 2013, **5,** e36 (7pp).

[52] C. Lee, X. Wei, J. W. Kysar and J. Hone, *Science*, 2008, **321**, 385-388.

[53] C. L. P. Pavithra, B. V. Sarada, K. V. Rajulapati, T. N. Rao and G. Sundarajan, *Sci. Rep.*, 2014, **4**, 4049.

[54] Q. Wang, C. Wang, M. Zhang, M. Jian and Y. Zhang, *Nano Lett.*, 2016, **16**, 6695-6700.

[55] K. Saito, J. Nakamura and A. Natori, *Phys. Rev. B*, 2007, **76**, 115409 (4pp).

[56] A. A. Balandin, S. Ghosh, W. Bao, I. Calizo, D. Teweldebrhan, F. Miao and C. N. Lau, *Nano Lett.*, 2008, **8**, 902-907.

[57] R. R. Nair, P. Blake, A. N. Grigorenko, K. S. Novoselov, T. J. Booth, T. Stauber, N. M. R. Peres and A. K. Geim, *Science*, 2008, **320**, 1308 (1pp).

[58] X. Wang, L. Zhi and K. Müllen, *Nano Lett.*, 2008, **8**, 323-327.

[59] S. Bae, H. Kim, Y. Lee, X. Xu, J. S. Park, Y. Zheng, J. Balakrishnan, T. Lei, H. R. Kim, Y. I. Song, Y. J. Kim, K. S. Kim, B. Ozyilmaz, J. H. Ahn, B. H. Hong and S. Iijima, *Nat. Nanotechnol.*, 2010, **5**, 574-578.

[60] P. R. Wallace, *Phys. Rev.*, 1947, **71**, 622-634.

[61] A. H. Castro Neto, F. Guinea, N. M. R. Peres, K. S. Novoselov and A. K. Geim, *Rev. Mod. Phys.*, 2009, **81**, 109-162.

[62] K. I. Bolotin, K. J. Sikes, Z. Jiang, M. Klima, G. Fudenberg, J. Hone, P. Kim and H. L. Stormer, *Solid State Commun.*, 2008, **146**, 351-355.

[63] X. Du, I. Skachko, A. Barker and E. Y. Andrei, *Nat. Nanotechnol*., 2008, **3**, 491-495.

[64] Y. Zhang, Y. W. Tan, H. L. Stormer and P. Kim, *Nature*, 2005, **438**, 201-204.

[65] I. V. Fialkovsky, V. N. Marachevsky and D. V. Vassilevich, *Phys. Rev. B*, 2011, **84**, 035446 (10pp).

[66] M. I. Katsnelson, K. S. Novoselov and A. K. Geim, *Nat. Phys*., 2006, **2**, 620-625.

[67] S. Pisana, M. Lazzeri, C. Casiraghi, K. S. Novoselov, A. K. Geim, A. C. Ferrari and F. Mauri, *Nat. Mater.*, 2007, **6**, 198-201.

[68] J. H. Ahn and B. H. Hong, *Nat. Nanotechnol*., 2014, **9**, 737-747.

[69] X. Li, Y. Zhu, W. Cai, M. Borysiak, B. Han, D. Chen, R. D. Piner, L. Colombo and R. S. Ruoff, *Nano Lett.*, 2009, **9**, 4359-4363.

[70] Y. M. Lin, C. Dimitrakopoulos, K. A. Jenkins, D. B. Farmer, H.Y. Chiu, A. Grill and P. Avouris, *Science*, 2010, **327**, 662 (1pp).

[71] T. Jiang, W. Sun, Q. Zhu, N. A. Burns, S. A. Khan, R. Mo and Z. Gu, *Adv. Mater.*, 2015, **27**, 1021-1028.

[72] X. Zheng, B. Jia, H. Lin, L. Qiu, D. Li and M. Gu, *Nat. Commun*., 2015, **6**, 8433 (7pp).

[73] L. G. D. Arco, Y. Zhang, C. W. Schlenker, K. Ryu, M. E. Thompson and C. Zhou, *ACS Nano*, 2010, **4**, 2865-2873.

[74] M. D. Stoller, S. Park, Y. Zhu, J. An and R.S. Ruoff, *Nano Lett*., 2008, **8**, 3498-3502.

[75] J. W. Suk, A. Kitt, C. W. Magnuson, Y. Hao, S. Ahmed, J. An, A. K. Swan, B. B. Goldberg and R. S. Ruoff, *ACS Nano*, 2011, **5**, 6916-6924.

[76] M. H. Rümmeli, A. Bachmatiuk, A. Scott, F. Börrnert, J. H. Warner, V. Hoffman, J. H. Lin, G. Cuniberti and B. Büchner, *ACS Nano*, 2010, **4**, 4206-4210.

[77] J. Chen, Y. Wen, Y. Guo, B. Wu, L. Huang, Y. Xue, D. Geng, D. Wang, G. Yu and Y. Liu, *J. Am. Chem. Soc*., 2011, **133**, 17548-17551.

[78] L. Zhang, Z. Shi, Y. Wang, R. Yang, D. Shi and G. Zhang, *Nano Res.* 2011, **4**, 315-321.

[79] G. Kalita, S. Sharma, K. Wakita, M. Umeno, Y. Hayashi and M. Tanemura, *Phys. Status Solidi A*, 2012, **209**, 2510-2513.

[80] R. Hirano, K. Matsubara, G. Kalita, Y. Hayashi and M. Tanemura, *Nanoscale*, 2012, **4**, 7791-7796.

[81] R. Vishwakarma, M. S. Rosmi, K. Takahashi, Y. Wakamatsu, Y. Yaakob, M. I. Araby, G. Kalita, M. Kitazawa and M. Tanemura, *Sci. Rep.*, 2017, **7**, 43756 (8pp).

[82] M. Tanemura, M. Kitazawa, J. Tanaka, T. Okita, R. Ohta, L. Miao and S. Tanemura, *Jpn. J. Appl. Phys*., 2006, **45**, 2004-2008.

[83] H. S. Sim, S. P. Lau, L. K. Ang, G. F. You, M. Tanemura, K. Yamaguchi, M. Zamri and M. Yusop, *Appl. Phys. Lett*., 2008, **93**, 023131 (3pp).

[84] M. Z. M. Yusop, P. Ghosh, Y. Yaakob, G. Kalita, M. Sasase, Y. Hayashi and M. Tanemura, *ACS Nano*, 2012, **6**, 9567-9573.

[85] M. Zamri, P. Ghosh, Z. P. Wang, M. Kawagishi, A. Hayashi, Y. Hayashi and M. Tanemura, *J. Vac. Sci. Technol. B*, 2010, **28**, C2C9-C2C12.

[86] Y. Yaakob, M. Z. M. Yusop, C. Takahashi, M. S. Rosmi, G. Kalita and M. Tanemura, *RSC Adv*., 2015, **5**, 5647-5651.

[87] Y. Yaakob, M. Z. Yusop, C. Takahashi, G. Kalita, P. Ghosh and M. Tanemura, *Jpn. J. Appl. Phys.*, 2013, **52**, 11NL01 (4pp).

[88] Y. Yaakob, Y. Kuwataka, M. Z. M. Yusop, S. Tanaka, M. S. Rosmi, G. Kalita and M. Tanemura, *Phys. Status Solidi B*, 2015, **252**, 1345-1349.

[89] M. I. Araby, M. S. Rosmi, R. Vishwakarma, S. Sharma, Y. Wakamatsu, K. Takahashi, G. Kalita, M. Kitazawa and M. Tanemura, *RSC Adv*., 2017, **7**, 47353-47356.

# Chapter 2

# Materials and Methods

As graphene can be visualized as a peeled single layer of $sp^2$ hybridized carbon atoms from a bulk of graphite, it might be formed as the initial layer during the formation of graphite in rock formation. But its isolation from graphite is not an easy task at least for the larger size. In this chapter, among the various techniques of synthesis of graphene, chemical vapor deposition technique, the technique adopted in this research is explained in details. Further, the transfer of graphene in the arbitrary substrates and the instruments used in the characterization process are described in brief. In the similar manner, the synthesis technique of CNFs by ion beam irradiation and their graphitization, their characterization tools are discussed in detail.

## 2.1 Graphene synthesis by chemical vapor deposition (CVD)

As discussed earlier in chapter 1, CVD is the technique of deposition of thin film on a catalytic surface in which the surface called the substrate is exposed to the volatile materials called precursors generally at the high temperature. In general, graphene is synthesized using CVD in two ways; the low pressure CVD (LPCVD) in which the exhaust is connected to a vacuum pump and the atmospheric pressure CVD (APCVD) in which the exhaust is left to be open in the atmosphere with a tube nozzle or some time the nozzle of the exhaust tube is dipped in water in order to make sure that the gas is flowing. **Fig. 2.1 (a)** represents the schematics of a conventional CVD whereas **Fig 2.1 (b)** shows the photograph of the CVD used as APCVD for the work described in chapter 3. On the other hand, there can be used the precursors in all the three states gases, liquids and solids in a CVD with respect of which they can be named as

gas, liquid and solid sourced CVD respectively. In contrast to the gas sourced CVD, the solid and liquid precursors are kept inside the quartz tube prior to starting the heating process and

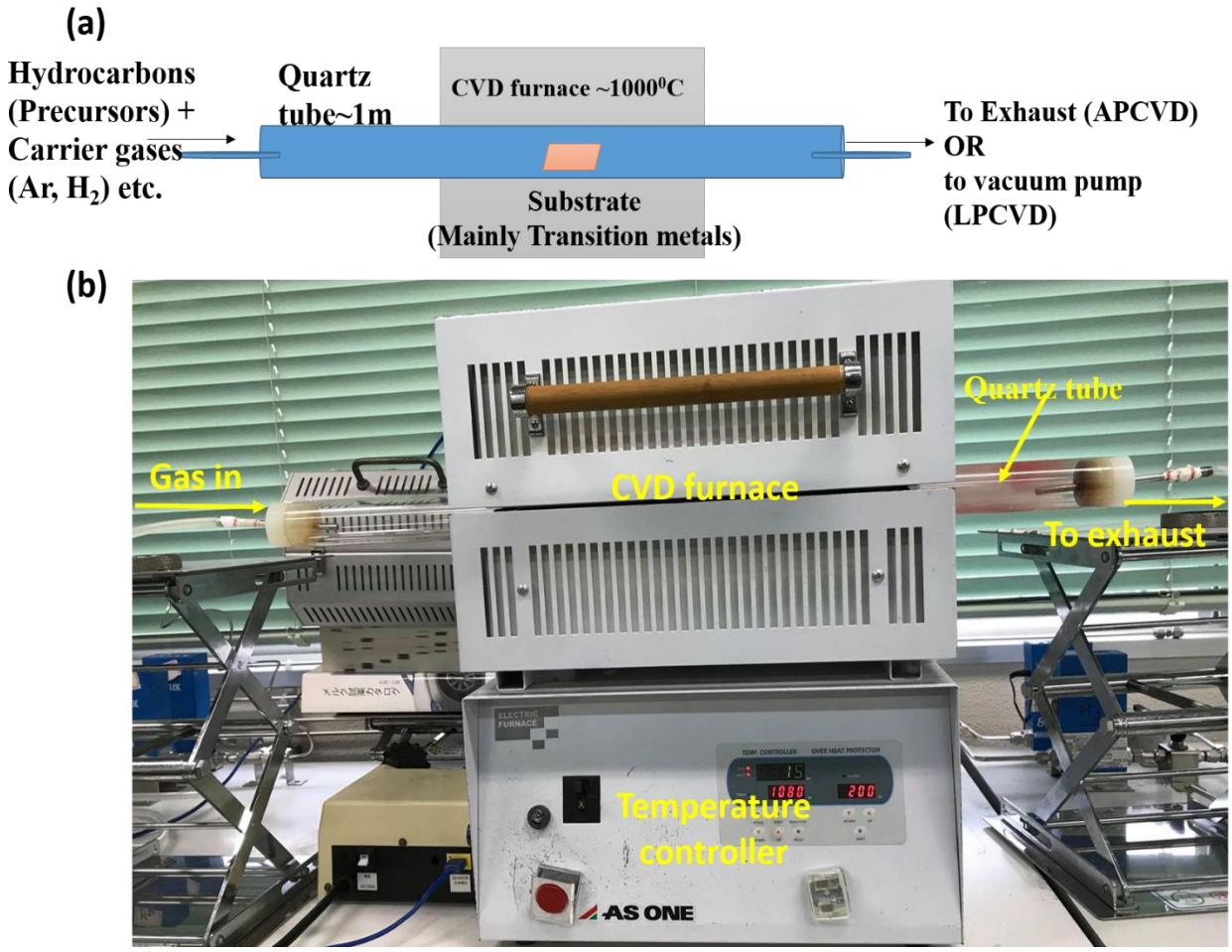


**Figure 2.1** Graphene synthesis using a CVD system, (a) Schematic of conventional CVD to show different components and (b) a photograph of CVD system in APCVD mode used for this work.

their pyrolysis is done either using a separate heating furnace or by a special magnetic sliding system by keeping the precursors in magnetic boat. In such sliding arrangement case as followed in the work described in chapter 3, the pyrolysis temperature is monitored on the basis of distance of the precursor from the CVD furnace followed by successive measurement of the temperature using infrared (IR) thermometer.

## 2.2 Graphene transfer techniques

As the graphene synthesized by CVD process is in the state adhered on the metallic substrates, it is to be transferred into the arbitrary substrate before its use and many characterizations. Conventionally, the Poly(methyl methacrylate) (PMMA) assisted transfer technique is used to transfer the graphene in any arbitrary substrate which can be either wet etching method[1-3] or the electrochemical delamination[4-6] also known as bubble transfer method. In the wet etching method, a layer of PMMA is spin coated on the graphene adhered to the metallic substrates followed by chemical etching of metal in the solutions of etchant like ferric chloride ($FeCl_3$), ferric nitrate($Fe(NO_3)_3$) and ammonium thiosulphate ($(NH_4)_2S_2O_8$). The graphene adhered to the PMMA is then rinsed in deionized (DI) water several times to remove the etchant contamination and then scooped on the arbitrary substrate on which it is to be transferred directly floated from the DI water. Finally, it is baked for some time to adhere the PMMA-graphene layer on the substrate and then the PMMA at the top is delaminated with acetone or acetone vapor. By its name, it is clear that the substrate metal is lost and also called metal sacrificial method. The graphical representation of different steps followed during this process is shown in schematics of **Fig. 2.2 (a)**. On the other hand, in electrochemical delamination method, the PMMA-graphene layer is detached from the metal substrate by the process of electrolysis in the dilute solution like NaOH without sacrificing the metal substrate which can be reused.[4,5] In this method, the PMMA-graphene-metal sheet is used as a cathode with an inactive anode (**Fig. 2.2 (b)**).

The transferred graphene by above methods is always associated with one or more of metallic substrate, etchant solution and PMMA contamination residues. The complete removal of these contamination is almost inevitable. Regan et al.[7] modified this standard wet etching transfer method without using the PMMA coating and successfully transferred well adhered graphene on a TEM grid (**Fig. 2.2 (c)**) and termed as the direct transfer technique. In addition

to these, the hot press technique to transfer the CVD graphene can also be promising as a polymer free technique.[8]

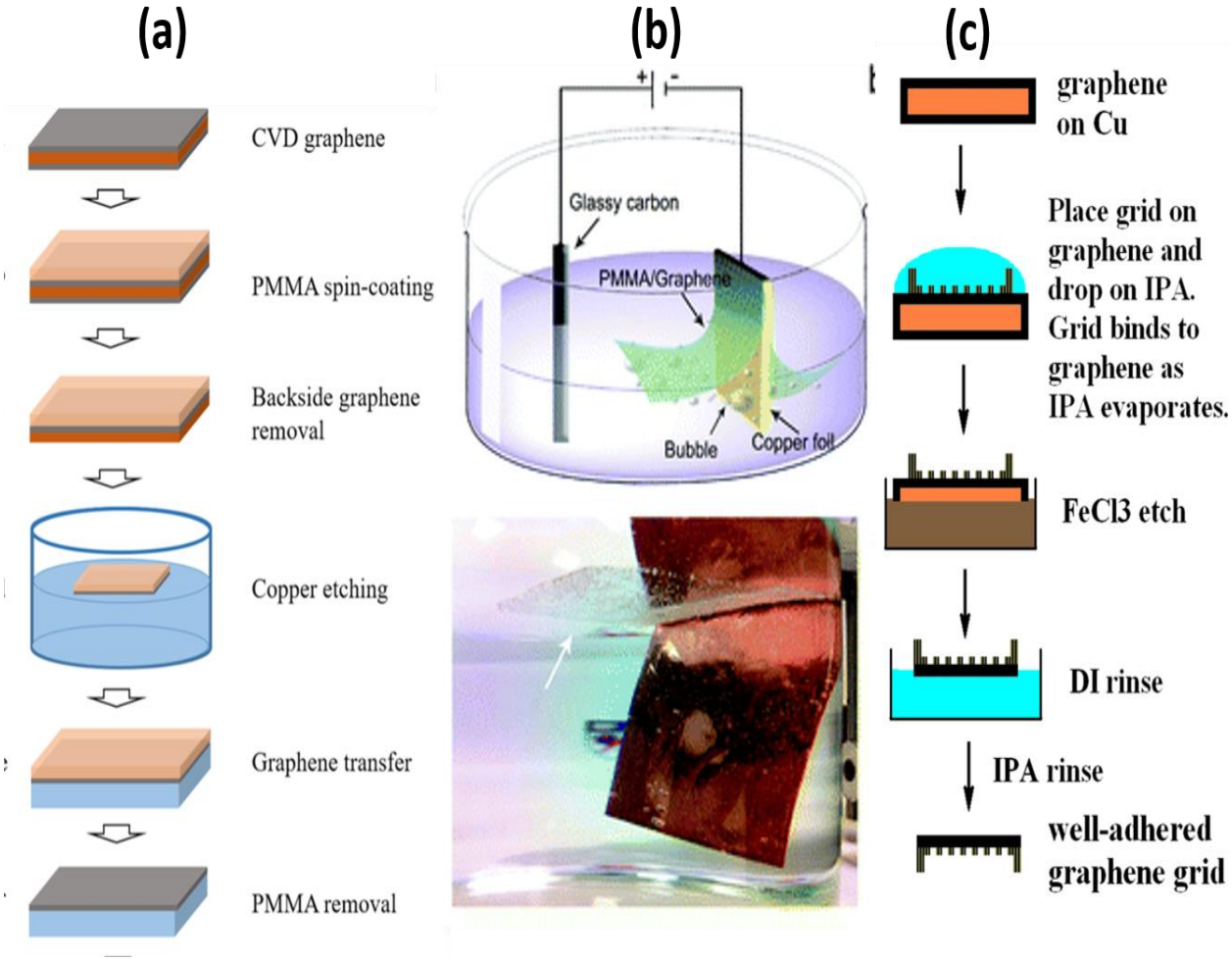


**Figure 2.2** Graphene transfer techniques, (a) schematics to show the different steps in a standard wet etching method,[9] (b) up: schematics, down: photographic image to show the electrochemical delamination[5] and (c) schematics of so-called direct polymer free transfer technique.[7]

## 2.3 Ion beam irradiation technique for CNF synthesis

The metal incorporated CNFs samples used in this study for the in situ TEM field emission (FE) characterization as well as for the vacuum annealing purposes are synthesized by using ion bombardment method. $Ar^+$ ions at an incident angle $45^o$ are used in bombardment

as the inclination is belived to be suitable for ion induced CNFs synthesis.[10] The vacuum system is managed using a rotary pump as well as a turbo molecular pump. The substrate and the source metal are kept mutually perpendicular to each other as shown in the shematics of **Fig. 2.3**. It should be noted that the position of the source and the substrate is just reversed in case of the metal Ga as it liquifies just above the room temperature. This inversion in the position doesn't alter the mechanism of CNF formation due to equal inclination of the ion beam to both the source and the substrate. The details of the experimental arrangemet is described in chapter 4 and 5.

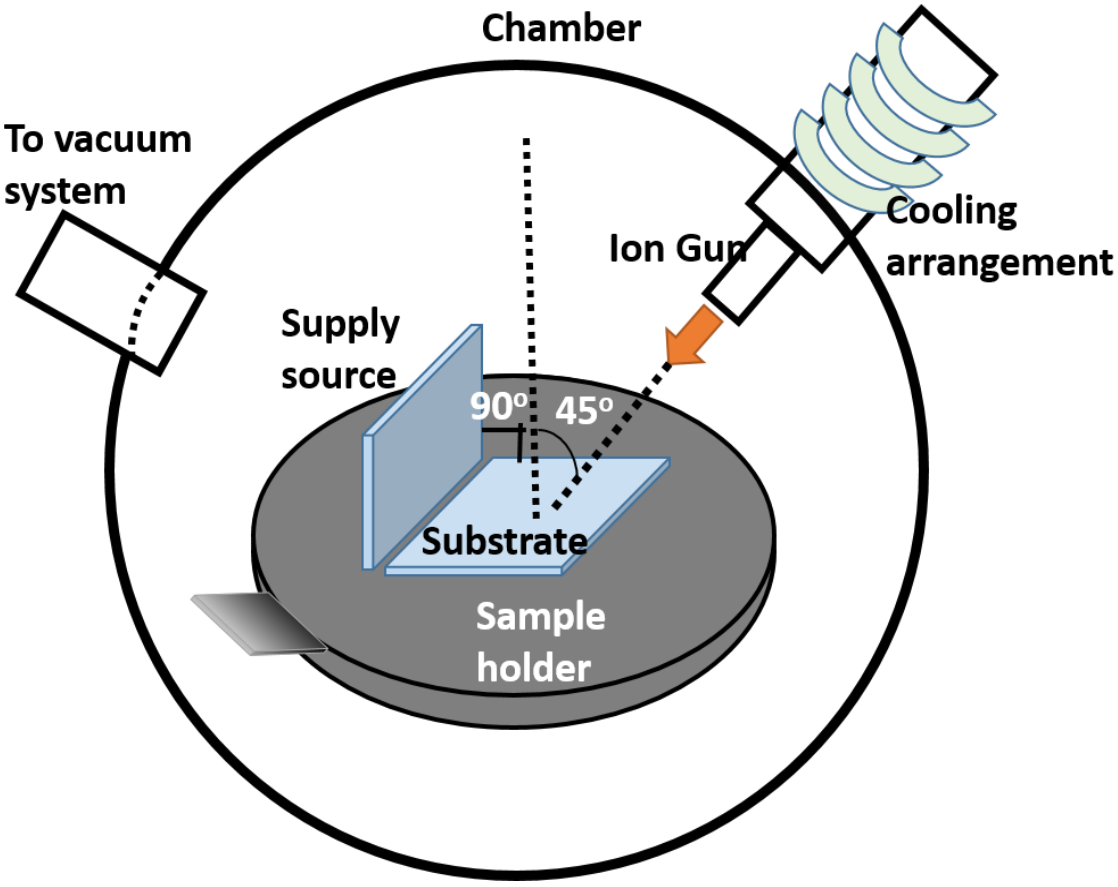


**Figure 2.3** Schematics of experimental set up for the ion beam bombardment method.

## 2.4 Vacuum annealing of gallium incorporated CNFs (Ga-CNFs)

For the graphitization of nanocarbons in the form of CNFs and cones, the Ga-CNFs samples prepared by the ion beam bombardment were heated directly in a vacuum heater at pressure about $5x10^{-3}$ Pa. Miller heater (MILA 3000) was used with the vacuum system supported by both rotary and turbo pump with the arrangement of proper cooling system.

## 2.5 Characterization techniques

### 2.5.1 Optical microscopy

As its name, an optical microscope can be used to get the direct and magnified image of a specimen both in transmittance as well as in reflectance modes. The graphene samples on an opaque substrate can be viewed optically in reflectance mode. Just after the CVD synthesis of graphene crystals on copper substrate, the foil is heated in open atmosphere to a temperature 150 $^{o}$C so that the bare copper surface gets oxidized to red in color whereas the surface covered with graphene (crystals) remains unaffected. This contrast in color helps to get the optical images of these crystals characterizing their shape and size. However the exfoliated graphene flakes and the CVD graphene after transfer on $SiO_2$/Si substrate with the $SiO_2$ thicknesses 300 nm and 90 nm can be characterized in terms of not only their shape and size but also the layer numbers can be compared with the difference in contrast between the adjacent flakes using an optical microscope.[11]

### 2.5.2 Scanning electron microscopy (SEM)

A SEM is a tool to characterize the surface topography and composition of a specimen by scanning the surface with a focused electron beam. The secondary scattered electrons from

the specimen are received by the SEM detector and form a high resolution image. **Fig. 2.4** shows a schematic to explain the working principle of a SEM.[12] Both the graphene crystals synthesized on the copper foil as well as the metal incorporated CNFs in this work can be analyzed under a SEM to get their morphology. Furthermore, a SEM can also be used to obtain the quantitative information on crystallographic orientation of the substrate in electron backscattered diffraction (EBSD) mode as done in this work.

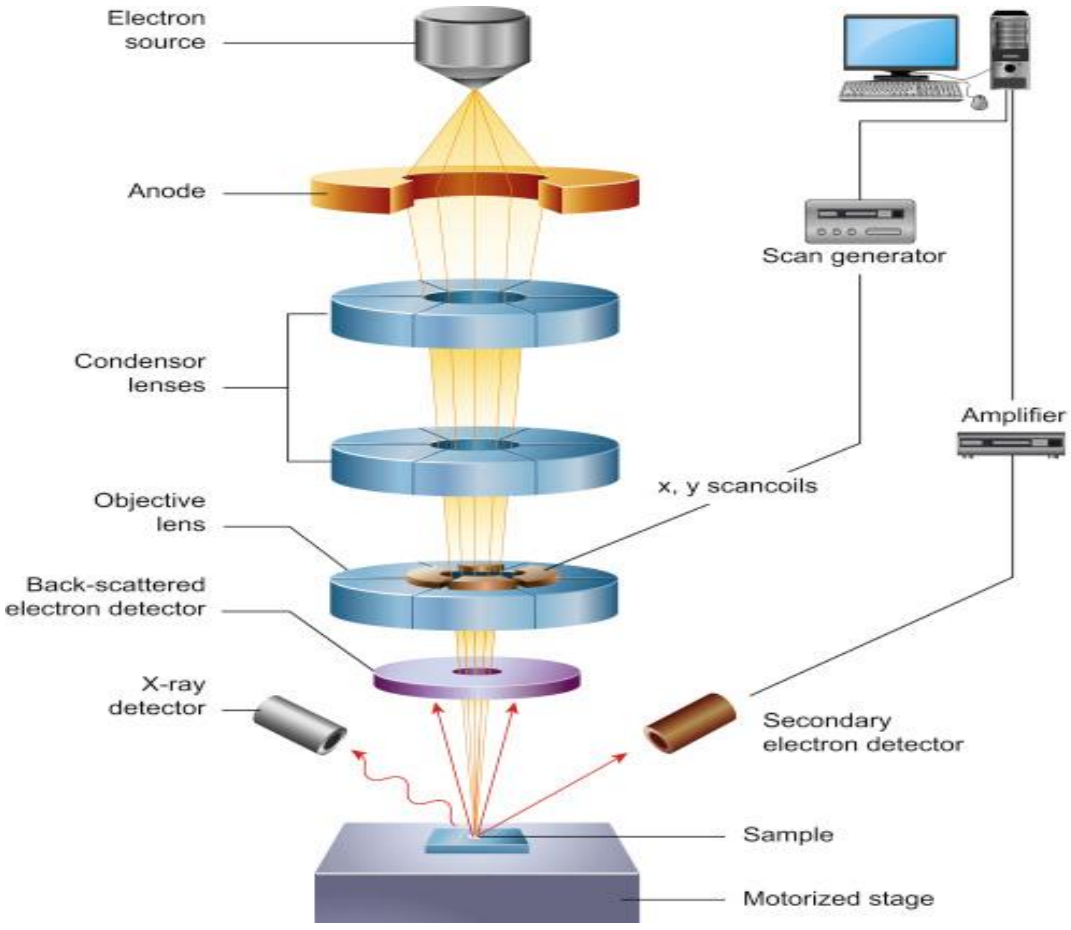


**Figure 2.4** Schematic diagram to show the working of a typical SEM.[12]

### 2.5.3 Transmission electron microscopy (TEM)

TEM is a characterizing technique of a specimen thin enough (up to 100 nm in thickness) to let an electron beam incident on it to pass and the transmitted electron beam after

its interaction with the specimen material is detected by a detector to form an image. Thus formed image is then magnified and focused on a fluorescent screen display. The crystal structure, morphology and the elemental composition of a specimen sample can be analyzed using a TEM. The CVD graphene can be transferred on a TEM grid before TEM analysis whereas the CNFs samples grown on the edge of a thin C-foil as in this work can be directly observed under TEM without any post treatment. **Fig. 2.5 (a)** shows a schematic of working of a basic TEM whereas **Fig 2.5 (b)** represents a photographic image of TEM: JEM-ARM200F (JEOL) used in the characterization in this work.

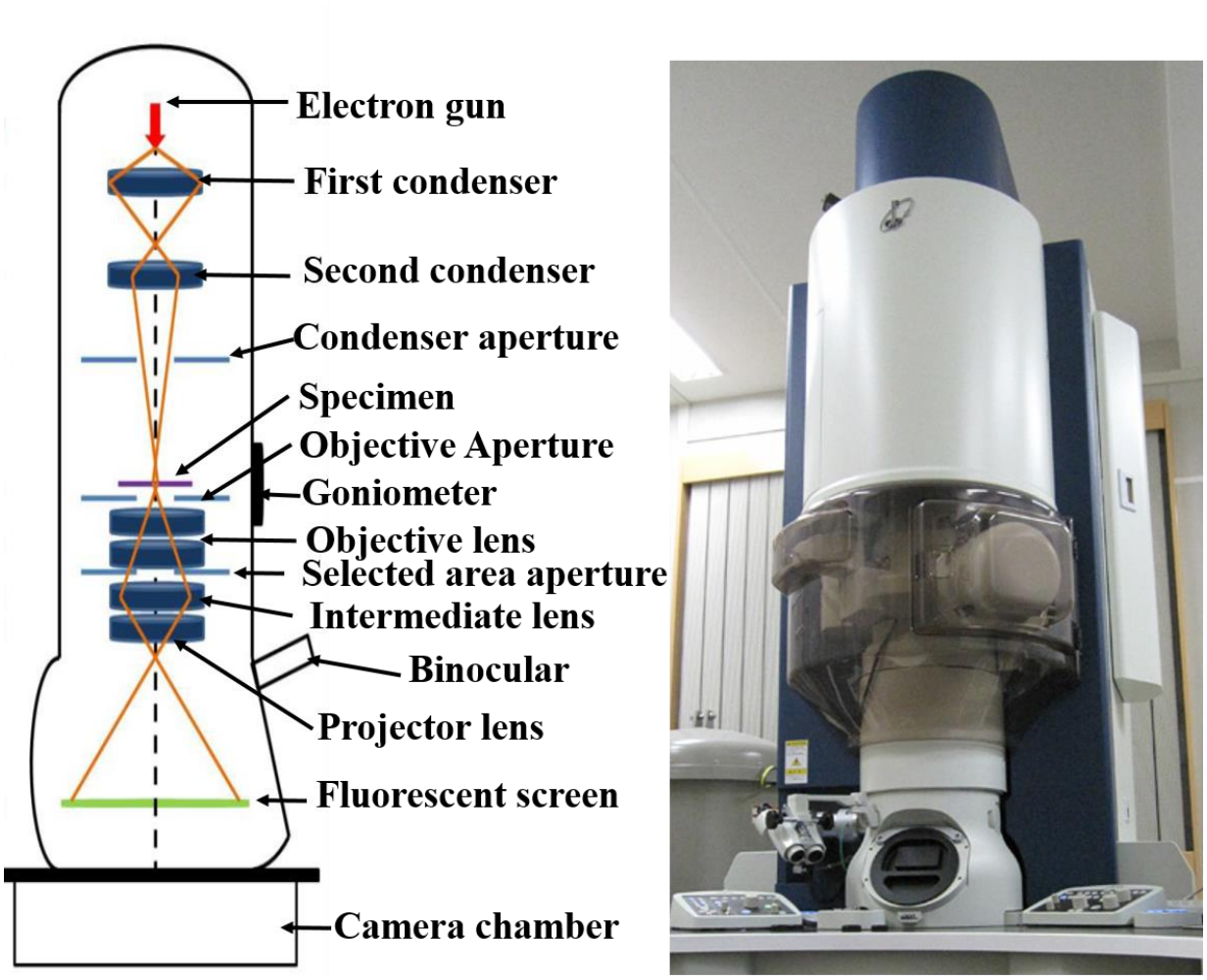


**Figure 2.5** (a) Schematic diagram to show the working of a basic TEM[13] and (b) a photographic image of TEM (JEOL JEM ARM200F).

In addition to the ultra-high magnification of a specimen region to analyze in atomic level, a TEM is also used to detect the composition of different constituent elements of the focused region in energy dispersive X-ray spectroscopy (EDS) mode. Furthermore, with some external arrangement, in situ functioning can be performed inside a TEM to measure the FE properties of single CNF and the corresponding current-voltage (I-V) characteristic curve can be plotted at the same time. A piezo driven TEM sample holder (JEOL; EM-Z02154T) connected to the external piezo system to control the sample movement in microscale and biasing voltage was used to explore the FE characteristics of Mo-CNFs and Ga-CNFs in the works described in chapter 4 and 5 respectively. In this process, a tungsten nanoprobe with tip diameter as low as 25 nm was used as an anode whereas the base of the respective CNFs was used as cathode. With the external piezo system, the tip of the nanoprobe can be brought in contact with the tip of the single CNF. When graduating bias voltage is passed through the system with time, the increasing voltage starts to produce heat across the CNF called Joule heating. The catalytic action of the NPs of the incorporated metals leads the nanocarbons in CNF to be graphitized which is indicated by a sudden increase in current in I-V measurement. Based on the metal NPs incorporated, there can occur the electromigration or evaporation of metal NPs forming CNT like graphitized structures. The increasing voltage then linearly increases the current through the CNF and finally breakdown occurs due to the excessive heat produced. **Fig. 2.6** shows the photographic images of different components used in in situ measurement process.

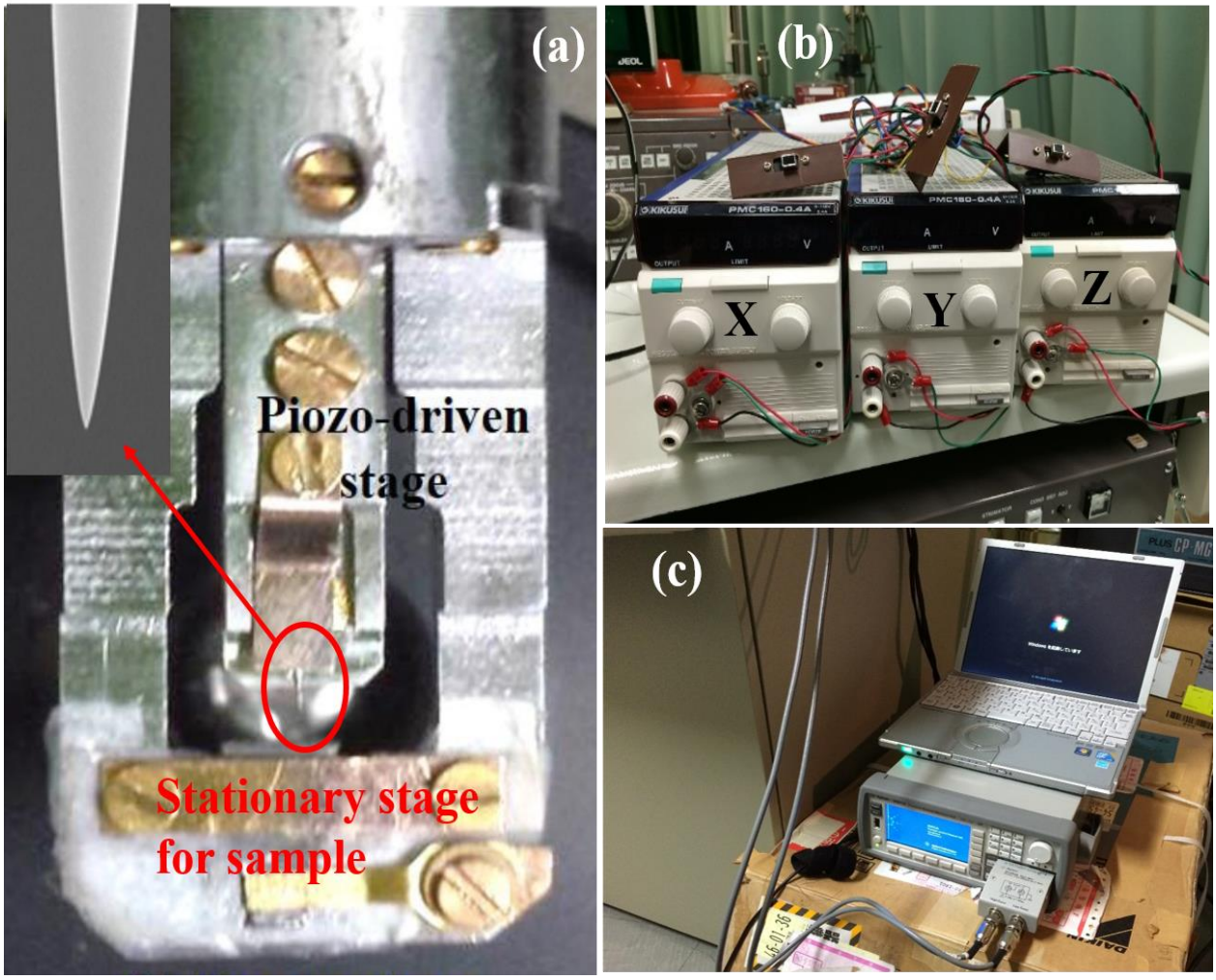


**Figure 2.6** The photographic images of (a) the sample stage of TEM sample holder (JEOL; EM-Z02154T) showing the tungsten nanoprobe (magnified image of the tip inset) in piezo-driven stage, (b) piezo system for the X (± 1 µm), Y (± 5 µm) and Z (± 5 µm) direction drive movement of nanoprobe and (c) set up for I-V measurement.

### 2.5.4 Raman spectroscopy

Raman spectroscopy is regarded as to provide a structural fingerprint for the identification of molecules in chemistry by utilizing inelastic scattering of monochromatic light from a specimen in vibrational mode. Being non-destructive and non-contacting technique, it can be performed simply in ambient pressure and at room temperature. Raman spectroscopy is widely used in the determination of number of layers in a graphene sample as well as to check

the qualitative information of graphene.[14-16] The Raman spectra of CVD graphene samples can be achieved either directly on the metallic substrate or after transferring into the $SiO_2$ substrate.

A Raman spectrum of graphene is dominantly recognized by three distinct peaks viz. D, G and 2D at around the positions 1350, 1590 and 2690 $cm^{-1}$ respectively.[15] The G peak, known as graphitic peak is associated due to the in-plane vibration of $sp^2$ bonding between the carbon atoms. The D peak also known as defect peak represents the amount of disorder present in the graphitic materials and is absent in a defect free graphene. Whereas, the 2D peak represents an overtone of D peak and is arisen from the inter-valley scattering of the electrons by the Brillouin zone boundary photons. Generally, the high value of 2D/G peak intensity ratio, low intensity of D peak and a steeper and narrower 2D peak are regarded as the characteristic features of a good quality graphene. Furthermore, the ratio of intensity of 2D to G peak is taken in account for the determination of number of layers in a graphene sample with $I_{2D}/I_G > 2$ for monolayer graphene, $2 > I_{2D}/I_G > 1$ for bilayer graphene and $I_{2D}/I_G < 1$ for higher number of layers.[17,18] **Fig. 2.7** represents a best example for this change in peak ratio with the graphene layer numbers.

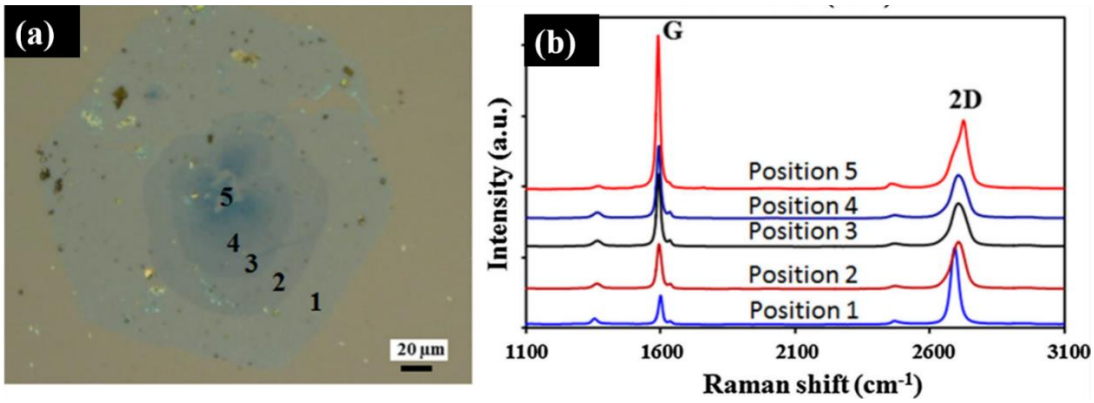


**Figure 2.7** (a) Optical image of a CVD graphene crystal transferred onto $SiO_2$ substrate and (b) Raman Spectra at different points indicated in fig. (a) indicating different number of graphene layers.[18]

### 2.5.5 Atomic force microscopy (AFM)

Atomic force microscopy is another technique to analyze the surface topography of a specimen sample in atomic scale. It works with the movement of the tip of a cantilever over the graphene sample surface either directly on the metal surface or on the surface of $SiO_2$ on which it is transferred in contact mode. This technique is widely used to measure the thickness of the graphene layer and hence is a tool to determine the number of graphene layers. Mostly the observed value of thickness of graphene with this method is slightly higher than the theoretical value due to the introduction of several impurities induced during the synthesis and transfer processes.[19,20]

## 2.6 References of chapter 2


[1] S. Bae, H. Kim, Y. Lee, X. Xu, J. S. Park, Y. Zheng, J. Balakrishnan, T. Lei, H. R. Kim, Y. I. Song, Y. J. Kim, K. S. Kim, B. Ozyilmaz, J. H. Ahn, B. H. Hong and S. Iijima, *Nat. Nanotechnol.*, 2010, **5**, 574-578.

[2] X. Li, Y. Zhu, W. Cai, M. Borysiak, B. Han, D. Chen, R. D. Piner, L. Colombo and R. S. Ruoff, *Nano Lett.*, 2009, **9**, 4359-4363.

[3] J. W. Suk, A. Kitt, C. W. Magnuson, Y. Hao, S. Ahmed, J. An, A. K. Swan, B. B. Goldberg and R. S. Ruoff, *ACS Nano*, 2011, **5**, 6916-6924.

[4] L. Gao, W. Ren, H. Xu, L. Jin, Z. Wang, T. Ma, L. P. Ma, Z. Zhang, Q. Fu, L. M. Peng, X. Bao and H. M. Cheng, *Nat. Commun.*, 2012, **3**, 699 (7pp).

[5] Y. Wang, Y. Zheng, X. Xu, E. Dubuisson, Q. Bao, J. Lu and K. P. Loh, *ACS Nano*, 2011, **5**, 9927-9933.

[6] C. T. Cherian, F. Giustiniano, I. M-Fernandez, H. Andersen, J. Balakrishan and B. Özyilmaz, *Small*, 2015, **11**, 189-194.

[7] W. Regan, N. Alem, B. Alemán, B. Geng, Ç. Girit, L. Maserati, F. Wang, M. Crommie and A. Zettl, *Appl. Phys. Lett*., 2010, **96**, 112102 (3pp).

[8] S. M. Shinde, G. Kalita, S. Sharma, Z. Zulkifli, R. Papon and M. Tanemura, *Surf. Coat. Techonol*., 2015, **275**,369-373.

[9] J. Sun, H. O. Finklea and Y. Liu, *Nanotechnol.*, 2017, **28**, 125703 (9pp).

[10] M. Tanemura, T. Okita, H. Yamauchi, S. Tanemura and R. Morishima, *Appl. Phys. Lett*., 2004, **84**, 3831-3833.

[11] P. Blake, E. W. Hill, A. H. Castro Neto, K. S. Novoselov, D. Jiang, R. Yang, T. J. Booth and A.K. Geim, *Appl. Phys. Lett.*, 2007, **91**, 063124 (3pp).

[12] B. J. Inkson, in Materials characterization using nondestructive evaluation (NDE) methods, ed. G. Huebschen, I. Altpeter, R. Tschuncky and H. G. Herrmann, Woodhead Publishing, Cambridge, 1st edn, 2016, ch. 2, pp. 17-43.

[13] D. B. Williams and C. B. Carter, *Transmission Electron Microscopy, Part I: Basics*, Springer Science, NY, 2009.

[14] A. C. Ferrari, *Solid State Commun*., 2007, **143**, 47-57.

[15] A. C. Ferrari, J. C. Meyer, V. Scardaci, C. Casiraghi, M. Lazzeri, F. Mauri, S. Piscanec, D. Jiang, K. S. Novoselov, S. Roth and A. K. Geim, *Phys. Rev. Lett*., 2006, **97**, 187401 (4pp).

[16] I. Childres, L. A. Jauregui, W. Park, H. Cao and Y.P. Chen, in *New Developments in Photon and Materials Research*, ed. J. I. Jang, Nova, NY, 1st edn, 2013, ch. 19, pp. 1-20.

[17] A. Reina, X. Jia, J. Ho, D. Nezich, H. Son, V. Bulovic, M. S. Dresselhaus and J. Kong, *Nano Lett*., 2009, **9**, 30-35.

[18] K. P. Sharma, S. M. Shinde, M. S. Rosmi, S. Sharma, G. Kalita and M. Tanemura, *J. Mater. Sci*., 2016, **51**, 7220-7228.

[19] K. S. Novoselov, D. Jiang, F. Schedin, T. J. Booth, V. V. Khotkevich, S. V. Morozov and A. K. Geim, *PNAS*, 2005, **102**, 10451-10453.

[20] C. Lee, Q. Li, W. Kalb, X. Z. Liu, H. Berger, R. W. Carpick, J. Hone, *Science*, 2010, **328**, 76-80.

# Chapter 3

# Switching isotropic and anisotropic graphene growth in a solid source CVD system

## 3.1 Introduction

CVD has been recognized as an ideal technique for the synthesis of graphene in wafer-scale with controllable number of layers on metal catalyst surfaces.[1-4] However, there are several factors that affect the CVD growth of graphene including the growth temperature, growth time, substrate selection, carrier gases, states and the nature of precursors, substrates pre-treatment etc.[5-10] It is well-known fact that the electrical and mechanical properties of CVD graphene are predominantly affected due to their polycrystalline nature and presence of grain boundaries.[11-16] Thus, optimization of various parameters is critical to minimize the effect of grain boundaries in CVD graphene, ideally by synthesizing large-area single crystals.[17-19]

The use of single crystalline metal substrates is common to obtain unidirectional alignment of graphene seeds to eliminate the grain boundaries.[20,21] But, it has been reported that such self-alignment of graphene domains can be well disturbed with defects and impurities affecting the single crystalline nature.[22] It was demonstrated that isotropic crystals can be grown instead of anisotropic crystals on a substrate melted to liquid state to overcome any specific grain orientation and growth along specific direction of graphene edges.[22] The obtained

graphene grains were isotopically round-shaped associated with mixed zigzag (ZZ) or armchair (AC) edges. In the liquid substrates, the orientation of adjacent graphene grains can be easily self-adjusted to smoothly match each other and thereby achieving the smooth stitching of the adjacent crystals through the edges.[23] This can be an alternative and reliable approach for synthesizing large-area single crystal graphene on Cu substrate without using single crystal metal substrates.[24,25]

Jiang et al. have demonstrated successfully that large single circular crystal graphene domains can be grown on a solid Cu substrate instead of using melted Cu with high supply rate of methane.[26] Individual isotropic graphene domains have been obtained with round smooth edges as well as axisymmetric and centrosymmetric shapes that allow seamless merging of adjacent graphene crystals.[24-26] However, these studies have dealt with isotropic graphene growth on either the liquid substrate or chemically pretreated substrates. Moreover, all these methods were designed for the graphene growth for gaseous carbon precursor like methane. Besides these, Sharma et al. have observed the growth of round-shaped crystals with waste plastic as the solid precursor.[27] However, there was no clear information described on the controllable tuning of graphene crystals growth from anisotropic to isotropic and their growth rate for synthesis of large single crystals. In contrast to previous reports, this study focuses on the controllable growth of the preferential isotropic graphene crystals in a solid source CVD process directly on the solid Cu substrate and insight on their growth rate and quality. It was found that the supply rate of solid precursor can be controlled by just controlling the carrier gases flow rate to tune anisotropic growth to isotropic and vice versa. It was also observed that the growth rate of the round-shaped graphene crystals is much faster than that of hexagonal crystals, thereby obtaining larger round-shaped graphene crystals for the same growth time compared to their anisotropic hexagonal analogs. In what follows, the details of the switchable

round-shaped (isotropic) and hexagonal-shaped (anisotropic) graphene crystals growth process in a solid source CVD method to achieve synthesis of large-area single crystals is discussed.

### 3.2 Materials and methods

Three sets of experiment were designed in a modified solid sourced CVD. In the first set (Exp. 1), the growth was performed with the supply of 100 standard cubic centimeter (sccm) of Ar and 2 sccm of $H_2$ gas as carrier gases. The second set (Exp. 2) was carried out with 75 and 1.5 sccm of Ar and $H_2$, respectively whereas in third set (Exp. 3), the flow rate was set as 50 and 1 sccm of Ar and $H_2$, respectively. In all experiments, the as received Cu foil of dimensions 2 cm × 2 cm × 25 μm (Nilaco Corporation, 99.98% purity) was heated to the growth temperature of 1050 $^oC$ at an average rate of 10.5 $^oC\ min^{-1}$ with the supply of 50 sccm of Ar inserting inside a quartz tube of diameter 4.5 cm and length about 1 m. Subsequently, the foil was annealed for 30 min. in Ar and $H_2$ environment (50 sccm of Ar and 8.5 sccm of $H_2$). In all experiments, 80 mg of the solid precursor Polyethylene (PE) (Molecular mass 35000 amu, Sigma Aldrich Co.) was heated at first above its melting point (120 $^oC$) for 2 min. and cooled down to 90 $^oC$ and again heated step wisely to 115 $^0C$ within 2 hours as this stepwise pattern was found favorable for crystal formation in solid sourced CVD.[8] The temperature of the precursor was tailored suitably by a sliding arrangement towards the hot furnace which avoids the necessity of the separate precursor heating furnace and its temperature was carefully monitored with the help of an external infrared thermometer. **Fig. 3.1(a)** reveals the structural diagram of a monomer of the precursor PE used in our experiments, Fig. 3.1(b) summarizes the overall set-up of the developed CVD system, whereas Fig 3.1(c) and (d) show the temperature profiles of heating of CVD furnace and the precursor respectively. Well after the growth, the $H_2$ supply was immediately stopped, and the foil with the quartz tube was cooled

down to the room temperature moderately within 30 min. only in the supply of Ar gas with the flow rate of 50 sccm whereas the solid precursor was slid far away from the heating furnace

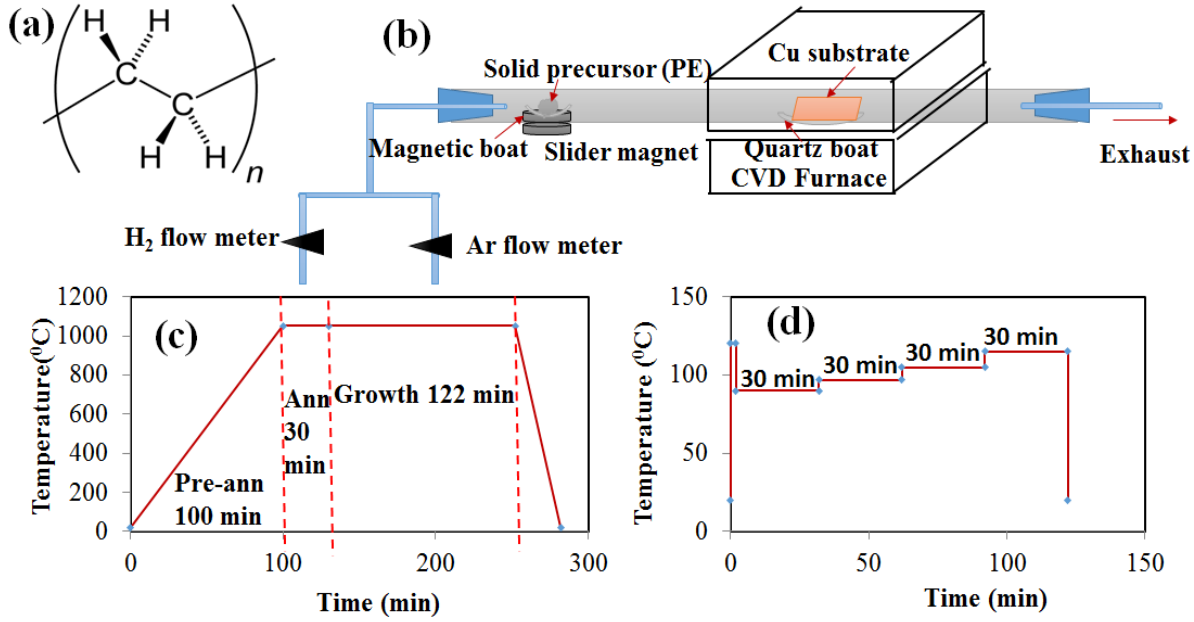


**Figure 3.1.** (a) Structural molecular formula of a monomer of the solid precursor PE, (b) schematic diagram to show the solid sourced CVD process. Temperature profile of (c) CVD furnace and (d) heating of solid precursor PE with time.

and cooled immediately within 2 min. using an external fan. The synthesized sample on Cu foil was heated on a hot plate to 200 $^0$C in the atmosphere for about 1 min. to oxidize the copper so that graphene is visible. For optical microscopic images, digital microscope VHX-500 in reflectance mode with a Moticam 2000; 2.0 M pixel camera was used, scanning electron microscopy (SEM) was performed with JEOL JSM 5600 using an accelerating voltage of 20 kV, Raman spectra were taken using NRS 3300 laser Raman spectrometer with a laser excitation energy of 532.08 nm, Atomic force microscope (AFM) study was carried out for transferred graphene crystals on $SiO_2$ using JSPM-5200 and Electron backscattered diffraction (EBSD) analysis was performed by an accelerating voltage of 20 KeV with the $70^0$ angle of incident beam equipped with an EBSD detector using JSM-7001FF. The graphene samples

were transferred onto $SiO_2$ (300 nm) coated Si substrate for confirmation of layer numbers and crystalline nature as with the wet etching method described in chapter 2 as reported elsewhere.[28] The graphene crystals were transferred with same technique with equal concentrations of solutions for equal interval of time for all sample measurements.

### 3.3 Result and discussion

The graphene crystals were synthesized with the varying amount of gas flow of Ar and $H_2$ without changing their ratio with constant amount of solid precursor. We have performed three different sets of experiments with Ar:$H_2$ gas mixture as 100: 2 (Exp. 1), 75:1.5 (Exp. 2) and 50:1 sccm (Exp. 3), where the ratio is constant. Synthesized graphene on the Cu foil was directly analyzed by optical microscope (OM) after mild oxidation at 200 $^0$C for the clear visibility of graphene crystals. **Fig. 3.2(a)** and (b) reveal the OM image and SEM image of the perfect hexagonal crystals obtained in the Exp. 1 respectively, clearly indicating the anisotropic growth. The size distribution of these hexagonal crystals was measured to be around 20-50 µm. Again, the edges of the individual hexagonal crystals are aligned with some of the crystals in their periphery (crystals 1 and 2 in Fig. 3.2(b)), while at the same time, some others were orientated with an angle (crystals 1 and 3 in Fig. 3.2(b)). This difference in edge orientation of hexagonal crystals has been also observed in several other studies, which has been explained as the effect of polycrystalline nature of Cu foil substrate.[5,22] Similarly, Fig. 3.2(c) and (d) present the OM and SEM images of hexagonal crystals with somewhat round corners to the hexagonal edges as if the growth is in the intermediate stage of anisotropic and isotropic growth for condition of Exp. 2. This evidently explains the effect of gas flow rate, as the carrier gas flow is reduced much precursor molecules can interact with catalyst substrate and thereby changing the growth dynamics. Now, further limiting the gas flow rate (Exp. 3), the growth

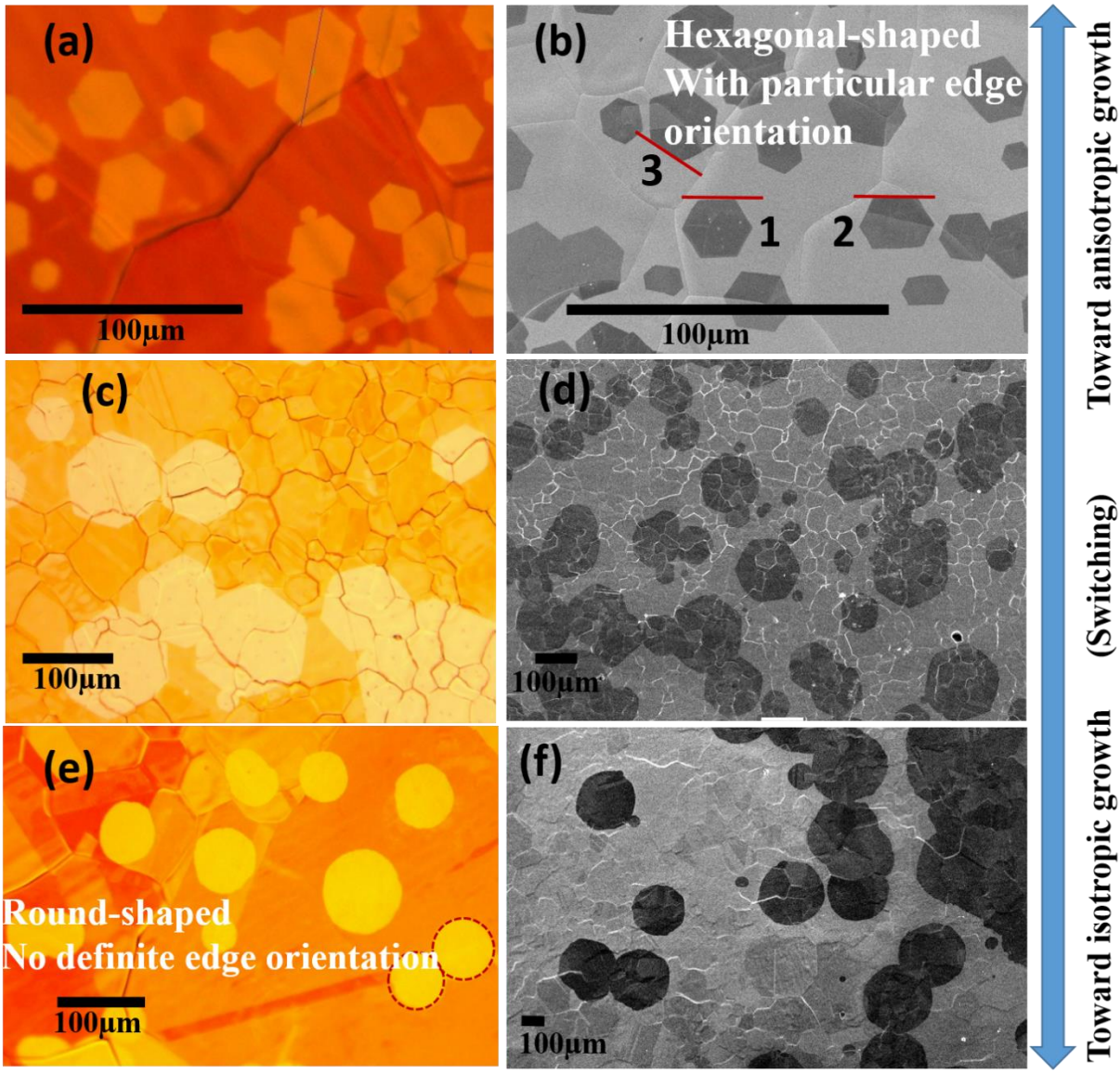


**Figure 3.2.** (a) OM image of the graphene crystals synthesized in Exp. 1 (100:2 sccm of Ar:$H_2$) and (b) respective SEM image. (c) OM image of the graphene crystals synthesized with Exp. 2 (75:1.5 sccm of Ar:$H_2$) and (d) respective SEM image. (e) OM image of the graphene crystals synthesized by Exp. 3 (50:1 sccm of Ar:$H_2$) and (f) respective SEM image.

mode was completely switched to isotropic nature. Fig. 3.2(e) and (f) sums up the OM and SEM images of almost circular crystals grown by the condition of Exp. 3. Such difference in growth behavior of the graphene crystals can be explained with the significant variation in amount of polyethylene molecules interacting with Cu surface with the change in flow rate of carrier gases. Significant differences in growth rate were observed with average graphene

domain sizes of 33.73 µm, 98.48 µm and 230.58 µm respectively in the experiments 1, 2 and 3, and the average growth speed calculated to be 0.276 µm $min^{-1}$, 0.8 µm $min^{-1}$ and 1.89 µm $min^{-1}$ respectively for the three cases (see **appendix Fig. A1** and **Table A1**). The average domain density was measured to be 2089.63 $mm^{-2}$, 70.7402 $mm^{-2}$ and 9.874 $mm^{-2}$, respectively (see **appendix Fig. A2** and **Table A2**) with evolution from anisotropic hexagonal to isotropic round-shaped crystal growth in the solid source CVD process. Again, influence in Cu grain size was also analyzed for the three experiments as average grain size increased with the decrease in Ar and $H_2$ gas composition from 100:2 to 50:1 sccm. OM analysis confirmed an average grain size of 54.85 µm, 79.83 µm and 110.54 µm, respectively with decreasing the flow rate of carrier gases (see **appendix Fig. A3** and **Table A3**). The electron back scattered diffraction (EBSD) analysis also indicated a relative increase in grain size for the polycrystalline Cu foil (see **appendix Fig. A4**). This may be due to the possible change in localized temperature and pressure of the Cu substrate with low stream of carrier gases in the CVD chamber.

Morphological analysis of individual crystals for all the experimental conditions (Exp. 1, Exp.2 and Exp.3) was performed to obtain further information of the anisotropic and isotropic growth. **Fig. 3.3(a)** shows a SEM image of single hexagonal crystal grown with Exp. 1, representing the anisotropic graphene growth. The size of the crystal is around 40 µm. Similarly, Fig. 3.3(b) shows the SEM image of large crystal grown with the intermediate condition of Exp. 2, where the crystal is neither perfectly hexagonal nor round- shaped. However, the crystals size is around ~230 µm for same growth duration as of the Exp. 1. Again, the fig. 3.3(c) shows the round-shaped crystal for the isotropic growth condition (Exp. 3). The size of the crystal further enhanced and was found to be around 410 µm. The obtained results are very conclusive that the decrease in the flow rate of carrier gases in the solid sourced CVD

system not only switch the mode of growth from anisotropic to isotropic but also increases the growth rate. The round-shaped graphene crystals size is much higher for same growth time

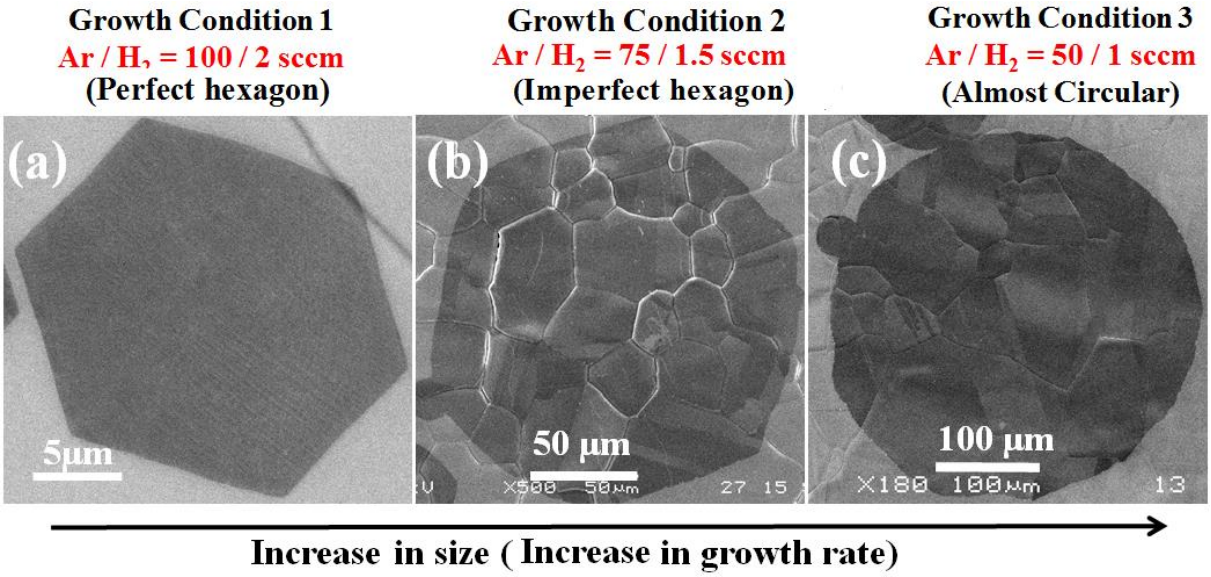


**Figure 3.3.** SEM images of individual large graphene crystal synthesized by the (a) anisotropic growth condition (perfect hexagon with Exp. 1), (b) intermediate growth condition (imperfect hexagon with Exp. 2) and (c) isotropic growth condition (round-shaped with Exp. 3) presenting the difference in size for same growth duration with change in gas flow rate.

without changing any growth condition rather than the flow rate of carrier gases. The round-shaped graphene crystals in Exp. 3 are larger almost by 10 times than that of anisotropic hexagonal crystals of Exp. 1. The increase in growth rate can be explained with higher concentration of PE precursor molecules which can react for longer duration with Cu surface as the amount of the Ar:$H_2$ gas mixture flowing as the carrier gas was reduced. This might be resulted in much higher carbon atom diffusion in the Cu surface, which led to the higher growth velocity preserve the isotropic nature to form the large round-shaped crystals. This isotropic growth nature of round-shaped crystals using PE as solid precursor is comparable with that of high flow rate methane CVD process as reported by Jiang et al.[26] and is more sustainable due to its more convex shapes exposing more edges to the incoming carbon flux as reported by Fan

et al.[29] The formation of perfect hexagonal graphene domains with six-fold symmetry by the CVD process is highly anisotropic, where growth along the axial direction is much faster than that of the radial direction. The growth of hexagonal graphene crystal with edge angle of $120^0$ is along the crystallographic direction, which can be regarded as total anisotropic growth behavior. However, the growth of an imperfect hexagon can comprise with both axial and radial directions, where the anisotropy could not be preserved due to the radial growth of the edges. In contrast, the circular graphene can be considered as the case of highly isotropic growth behavior, where the growth is independent of a particular orientation and is from all direction. Though, isotropic growth of a circular graphene has been demonstrated on isotropic amorphous liquid metal substrate in previous studies, but in these experiments the circular and hexagonal-shaped graphene domains were obtained on a polycrystalline Cu foil, where the graphene domains were grown across two or more different Cu grains. Hence, the crystallographic orientation of the Cu foil did not determine the shapes of graphene domains in each growth conditions. It was confirmed that the anisotropic and isotropic growth of the graphene crystals is strongly dependent on to the carbon flux, which determine the surface diffusion of carbon atoms and edge reaction process.[26,29,30] Reports have also shown that at a much higher carbon flow rate, sufficient carbon supply leads to diffusion in two directions producing a metastable state as a result the graphene crystals grows isotopically to form a circular domains.[26] Thus, by controlling the flow dynamics of the precursors along with the inert carrier gas as demonstrated in this work, the growth kinetics of the hexagonal and circular shaped graphene domains can be switched.

Again, high magnification SEM analysis was performed to view the specific edges of the synthesized anisotropic and isotropic crystals as shown in **Fig. 3.4(a)** and (b) for Exp. 1 and Exp. 3, respectively. The higher magnification SEM image in Fig. 3.4(a) shows the straight edges of anisotropic hexagonal crystal. It has been found that the CVD synthesized hexagonal

graphene crystals possess zigzag (ZZ) or armchair (AC) edge structures. Chen et al. has reported that the graphene synthesized by ethanol CVD possess AC edges, unlike ZZ edges of graphene synthesized by methane CVD process.[29] However, it is not clear enough of the edge structures of the hexagonal graphene obtained in the solid source CVD process using PE molecules as solid carbon source.

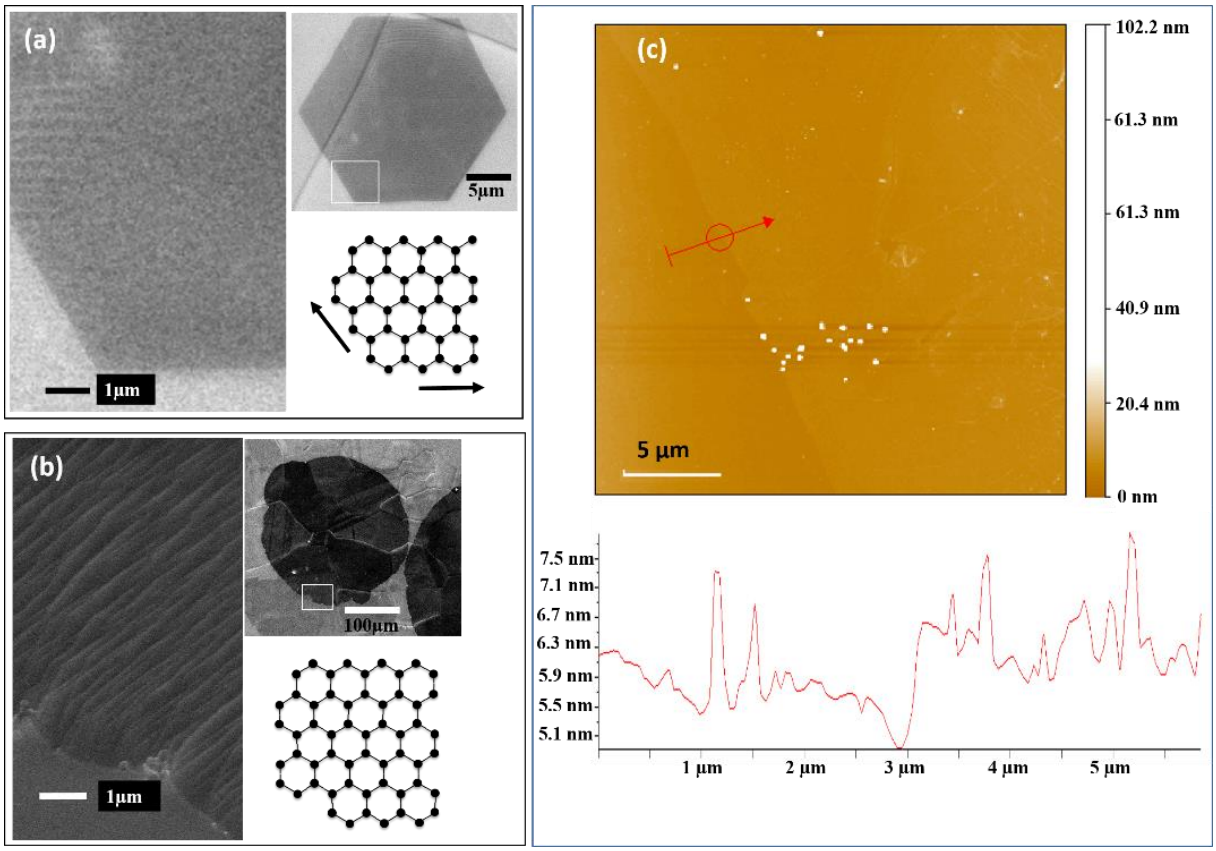


**Figure 3.4.** High magnification (a) SEM image of edge of an anisotropic graphene crystal and schematic for the edge structure, (b) SEM image of edge of the large isotropic crystal and schematics of probable atomistic arrangement of the edge with mixed AC and ZZ edges and (c) AFM image of edge of the hexagonal crystal with line profile of thickness measurement.

Fig. 3.4(b) shows high magnification SEM image of the edge of a large isotropic crystal grown with condition for Exp. 3. Semicircular edge structure can be observed for the round-shaped crystals. Such circular edges should possess both the ZZ and AC edges, where graphene growth

is independent of edge structures. This association of ZZ and AC edges also can contribute smooth merging of two or more graphene grains to achieve larger single isotropic graphene domains.[24-26, 32] Further, the smooth edge structure and thickness of the graphene crystal was confirmed by AFM study. Fig. 3.4(c) shows an AFM image for the hexagonal graphene crystal with corresponding thickness profile image at the edge. The AFM image shows an even edge of the graphene crystal without any dendrite like or uneven structure. Further, the line profile as shown in figure 3.4(c) shows a thickness of around 0.5 nm, attributing to a monolayer graphene.

Raman spectral analysis was performed to investigate the quality and layer numbers in hexagonal and round-shaped graphene crystals. The comparative study was performed at three different points (center, inside and edge) for both the anisotropic hexagonal and isotropic round graphene crystals after transferring to $SiO_2$/Si substrates. **Fig. 3.5(a)** shows the OM image of a transferred perfect hexagonal crystal on $SiO_2$/Si as obtained from the Exp.1. Fig. 3.5(b) represents the Raman spectra at three different points as indicated in Fig. 3.5(a). The Raman spectra confirmed a monolayer graphene as the 2D/G peak intensity ratio is around 2. We observed slight increase in the D peak, and this increase in the defect peak at the edge has been observed for hexagonal crystal due to the specific edge structures of ZZ or AC.[29-32] Fig. 3.5(c) shows the OM image of a transferred round-shaped crystal on $SiO_2$/Si substrate. Fig. 3.5(d) shows Raman spectra at three different points as indicated in fig. 3.5(c). These spectra confirmed a monolayer graphene with 2D/G peak intensity ratio higher than 2, where the defect is not significant. In addition, the Raman spectra also confirmed that the quality of the hexagonal and round-shaped crystal does not differ significantly. Thus, controlling the flow rate of carrier gases in the developed solid source CVD, tuning of the anisotropic and isotropic graphene growth can be achieved without compromising the quality of the graphene.

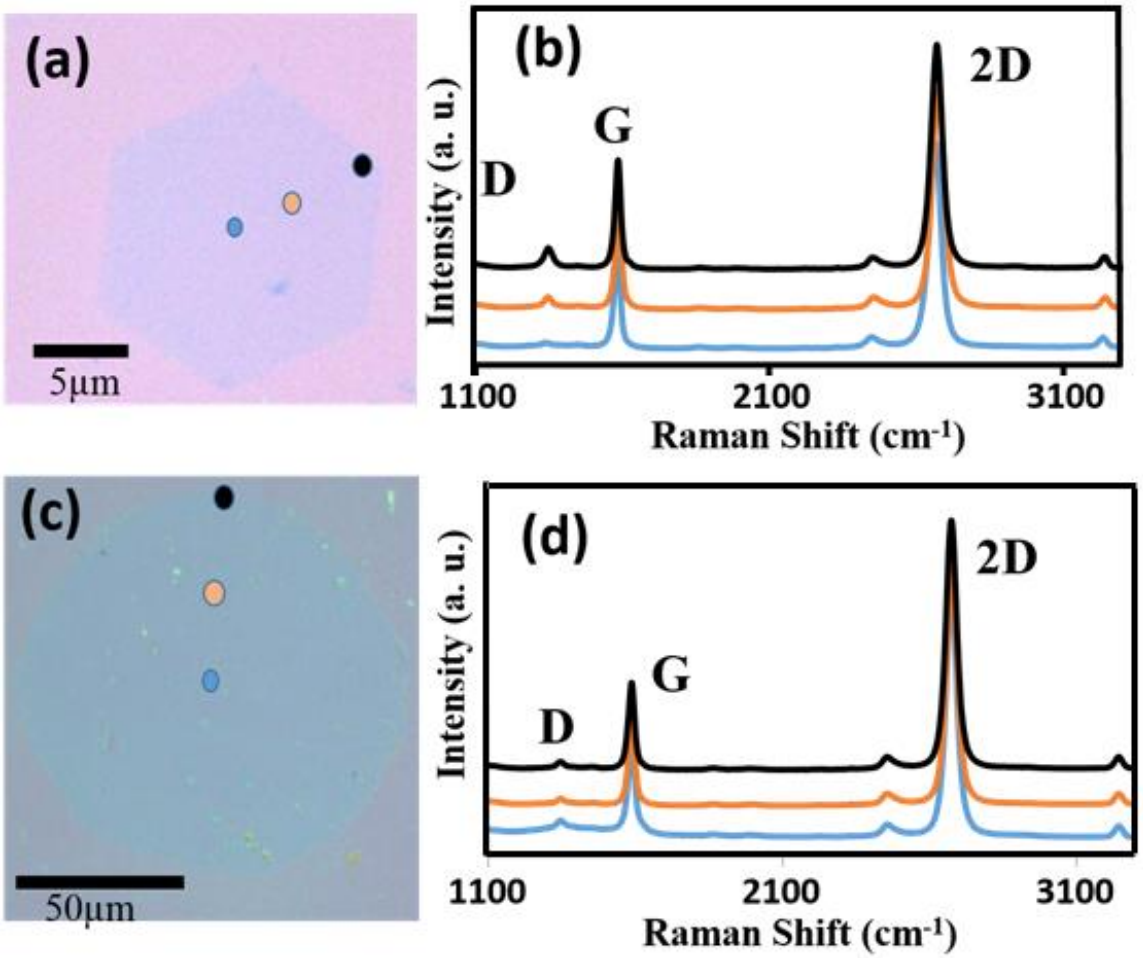


**Figure 3.5.** (a) OM image of an anisotropic hexagonal crystal grown in Exp. 1 and (b) corresponding Raman spectra at the three different points allocated as different colors. (c) OM image of an isotropic round crystal grown in Exp. 3 and (d) corresponding Raman spectra at three different points (center, inside and edge as allocated with different colors).

**Fig. 3.6(a)** shows the OM image of a large round-shaped graphene crystal transferred on $Si/SiO_2$ substrate. Raman mapping analysis of this isotropic crystal confirmed the single layer structure without any secondary nucleation within the single crystalline domain. Fig. 3.6(b) and (c) show the G and 2D peak intensity map for the transferred round-shaped crystal. The homogeneous intensity of G and 2D peak here clearly indicate the single crystalline nature with less defects. Fig. 3.6(d) shows the Raman map for the 2D/G peak ratio in which the ratio throughout the crystal is higher than 2, indicating the single layered graphene without any

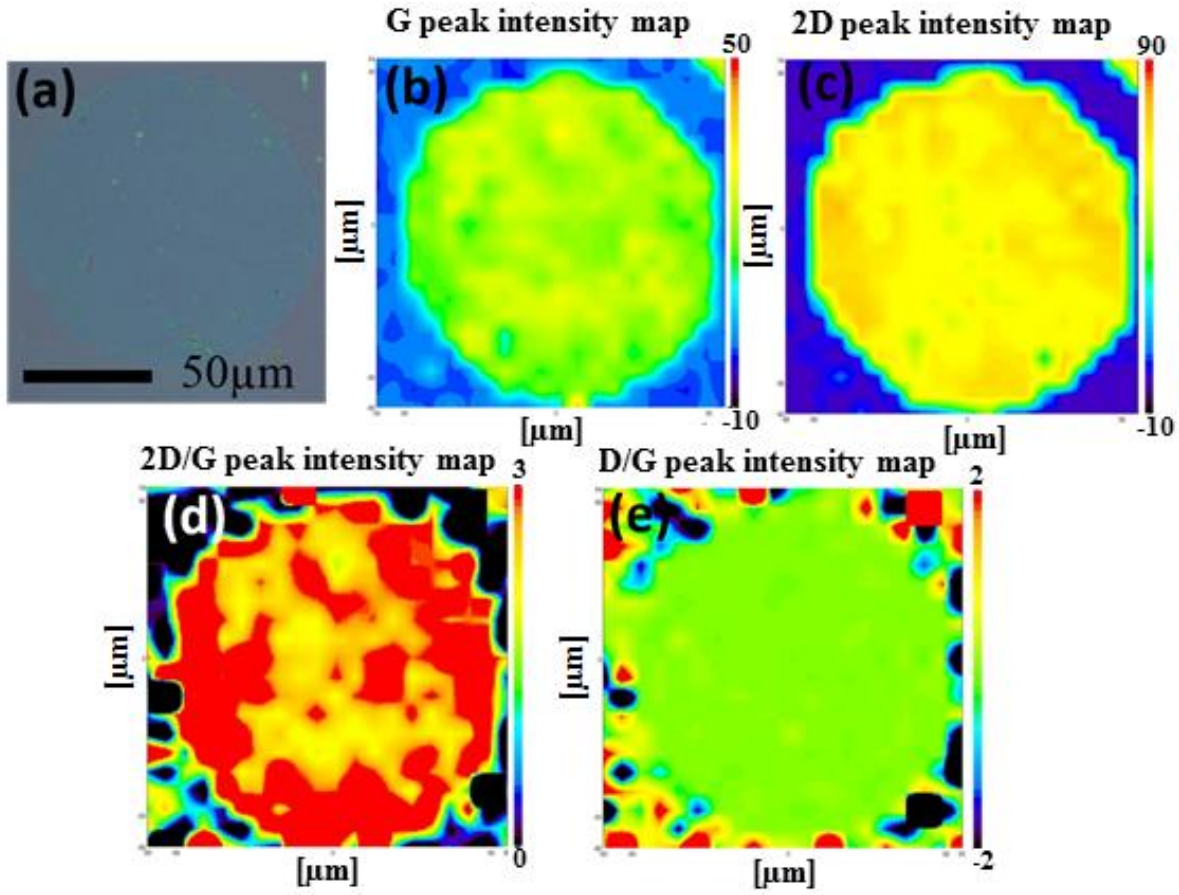


**Figure 3.6.** (a) OM image of single large isotropic crystal obtained in Exp. 3 and transferred onto the $SiO_2$/Si, Raman mapping images to show (b) G peak, (c) 2D peak, (d) 2D/G peak and (e) D/G peak intensity ratios.

secondary nucleation. Fig. 3.6(e) shows the Raman map of D/G peak ratio in which the ratio throughout the crystal is significantly less indicating minimum defect which also can be correlated with results of Raman spectra. **Fig. 3.7(a)**-(c) shows histogram plot of D/G peak ratio for the perfect hexagonal, imperfect hexagon and circular graphene crystals. Raman analysis performed at several points of the graphene crystals (see **appendix Fig A5**) consistently showed low defect induced D peak (see **appendix Table A4, A5** and **A6** for the different peak ratios). It clearly shows that the quality of graphene remains considerably preserved with the average D/G peak ratio 0.0317, 0.0549 and 0.0534 of the samples of the

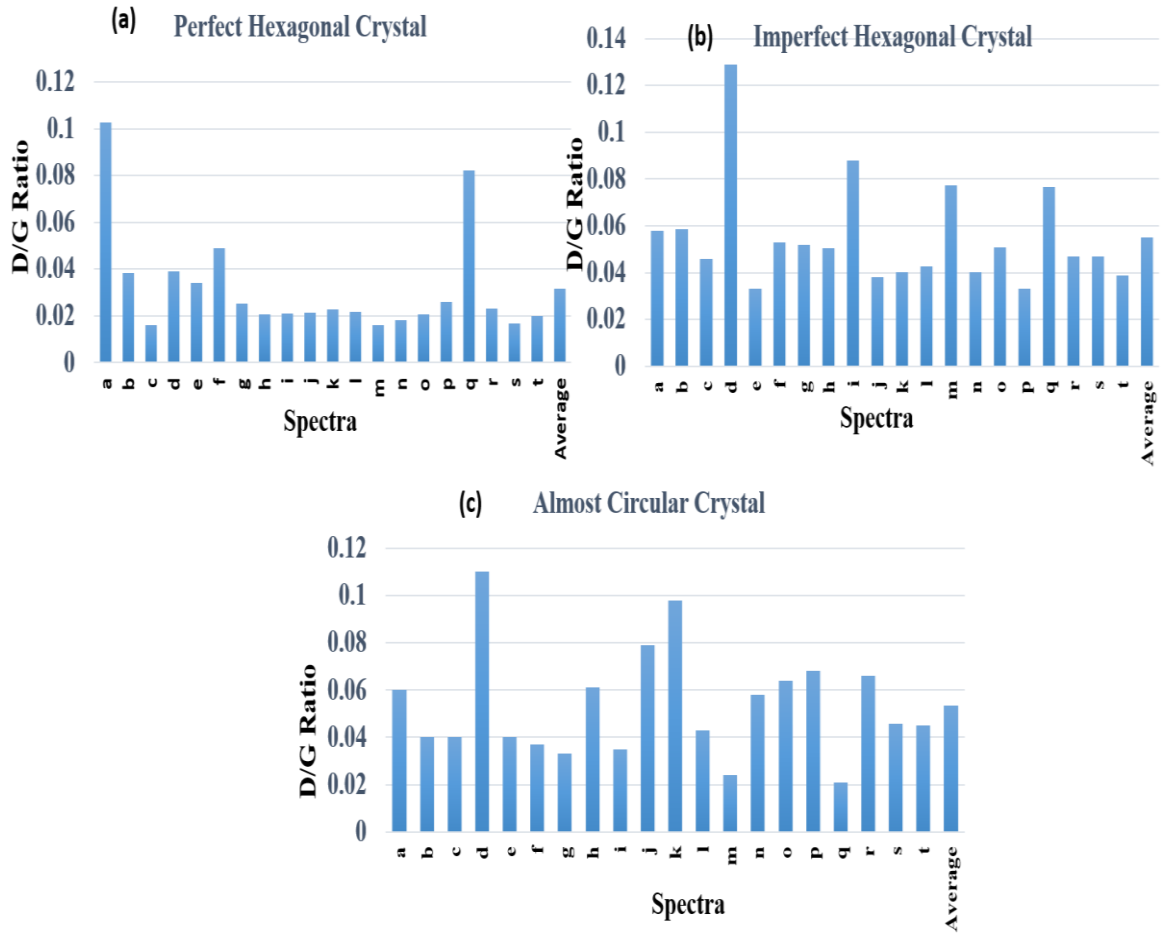


**Figure 3.7**: Histograms of D/G peak ratio of different point spectra for the (a) perfect hexagon (b) imperfect hexagon and (c) circular graphene crystals (Points of spectra were indicated in optical microscopy images of fig A5 in appendix).

Experiment 1, 2 and 3 respectively whereas the 2D/G peak ratio is averaged to be 2.2101, 2.5492 and 3.0944 respectively revealing the formation of monolayer graphene in all the three cases. Thus, the isotropic circular single layered graphene crystals with pristine quality can be grown by reducing the flow rate of carrier gases in the developed CVD system. Again, it is very interesting and promising that switching the anisotropic to isotopic growth process, the growth rate of the individual crystal enhances significantly without hindering the monolayer graphene quality.

### 3.4 Conclusions

In summary, the growth of the larger isotropic graphene crystals was achieved just by controlling the rate of flow of carrier gases and hence controlling the precursor supply rate in our solid sourced CVD system. This tuning the graphene growth from anisotropic to isotropic enlarges the graphene domains without compromising the quality of graphene. The synthesized isotropic crystals were larger than their anisotropic analogs for the same growth time signifying the faster growth rate of the round-shaped crystals. Difference in edge orientation was observed for the synthesized hexagonal crystals, while round-shaped crystals with mixed edge structure has no preferential edge orientation providing a better chance of seamless merging. These findings can be significant to understand the isotropic and anisotropic growth of graphene domains, their growth rate and quality for synthesizing large-area single crystals without any chemical pre-treatment of the substrates.

### 3.5 References of chapter 3


[1] P. R. Somani, S. P. Somani, M. Umeno, *Chem. Phys. Lett*., 2006, **430**, 56-59.

[2] S. Bae, H. Kim, Y. Lee, X. Xu, J. –S. Park, Y. Zheng, J. Balakrishnan, T. Lei, H. R. Kim, Y. I. Song, Y. J. Kim, K. S. Kim, B. Ozyilmaz, J. –H. Ahn, B. H. Hong and S. Iijima, *Nat. Nanotechnol.*, 2010, **5**, 574−578.

[3] T. Wu, G. Ding, H. Shen, H. Wang, L. Sun, D. Jiang, X. Xie and M. Jiang, *Adv. Funct. Mater.*, 2013, **23**, 198-203.

[4] Z. Yan, J. Lin, Z. Peng, Z. Sun, Y. Zhu, L. Li, C. Xiang, E.L. Samuel, C. Kittrell and J.M. Tour, *ACS Nano*, 2012, **6**, 9110-9117.

[5] E. Loginova, N. C. Bartelt, P. J. Feibelman and K. F. McCarty, *New J. Phys*., 2009, **11**, 063046 (20pp).

[6] P. Braeuninger-Weimer, B. Brennan, A. J. Pollard and S. Hofmann, *Chem. Mater*, 2016, **28**, 8905-8915.

[7] G. H. Han, F. Güneş, J. J. Bae, E. S. Kim, S. J. Chae, H. J. Shin, J. Y. Choi, D. Pribat and Y. H. Lee, *Nano Lett*., 2011, **11**, 4144-4148.

[8] K. P. Sharma, S. M. Shinde, M. S. Rosmi, S. Sharma, G. Kalita and M. Tanemura, *J. Mater. Sci*., 2016, **51**, 7220-7228.

[9] Y. Hao, M. S. Bharathi, L. Wang, Y. Liu, H. Chen, S. Nie, X. Wang, H. Chou, C. Tan, B. Fallahazad, H. Ramanarayan, C. W. Magnuson, E. Tutuc, B. I. Yakobson, K. F. Mccarty, Y. Zhang, P. Kim, J. Hone, L. Colombo and R. S. Ruoff, *Science*, 2013, **342**, 720-724.

[10] H. C. Lee, W. -W. Liu, S. -P. Chai, A. R. Mohamed, C. W. Lai, C. -S. Khe, C. H. Voon, U. Hashim and N. M. S. Hidayah, *Procedia Chem*., 2016, **19**, 916-921.

[11] L. P. Biró and P. Lambin, *New J. Phys*., 2013, **15**, 035024 (38pp).

[12] L. A. Jauregui, H. Cao, W. Wu, Q. Yu and Y. P. Chen, *Solid State Commun*., 2011, **151**, 1100-1104.

[13] Z. A. Van Veldhoven, J. A. Alexander-Webber, A. A. Sagade, P. Braeuninger-Weimer and S. Hofmann, *Phys. Status Solidi B*, 2016, **253**, 2321-2325.

[14] J. Dong, H. Wang, H. Peng, Z. Liu, K. Zhang and F. Ding, *Chem. Sci*., 2017, **8**, 2209-2214.

[15] P. Y. Huang, C. S. Ruiz-Vargas, A. M. Van Der Zande, W. S. Whitney, M. P. Levendorf, J. W. Kevek, S. Garg, J. S. Alden, C. J. Hustedt, Y. Zhu, J. Park, P. L. McEuen and D. A. Muller, *Nature*, 2011, **469**, 389-392.

[16] Q. Yu, L. A. Jauregui, W. Wu, R. Colby, J. Tian, Z. Su, H. Cao, Z. Liu, D. Pandey, D. Wei, T. F. Chung, P. Peng, N. P. Guisinger, E. A. Stach, J. Bao, S. –S. Pei and Y. P. Chen, *Nat. Mater*, 2011, **10**, 443-449.

[17] H. Wang, G. Wang, P. Bao, S. Yang, W. Zhu, X. Xie and W. J. Zhang, *J. Am. Chem. Soc*., 2012, **134**, 3627-3630.

[18] X. Xu, Z. Zhang, L. Qiu, J. Zhuang, L. Zhang, H. Wang, C. Liao, H. Song, R. Qiao, P. Gao, Z. Hu, L. Liao, Z. Liao, D. Yu, E. Wang, F. Ding, H. Peng and K. Liu, *Nature Nanotechol.*, 2016, **11**, 930-935.

[19] X. Xu, Z. Zhang, J. Dong, D. Yi, J. Niu, M. Wu, L. Lin, R. Yin, M. Li, J. Zhou, S. Wang, J. Sun, X. Duan, P. Gao, Y. Jiang, X. Wu, H. Peng, R. S. Ruoff, Z. Liu, D. Yu, E. Wang, F. Ding and K. Liu, *Sci. Bull*., 2017, **62**, 1074-1080.

[20] Y. Zhang, L. Gomez, F. N. Ishikawa, A. Madaria, K. Ryu, C. Wang, A. Badmaev, and C. Zhou, *J. Phys. Chem. Lett*., 2010, **1** (20)**,** 3101-3107.

[21] H. Ago, Y. Ohta, H. Hibino, D. Yoshimura, R. Takizawa, Y. Uchida, M. Tsuji, T. Okajima, H. Mitani, and S. Mizuno, *Chem. Mater*., 2015, **27(15)**, 5377-5385.

[22] M. Zeng, L. Tan, L. Wang, R.G. Mendes, Z. Qin, Y. Huang, T. Zhang, L. Fang, Y. Zhang, S. Yue, M. H. Rümmeli, L. Peng, Z. Liu, S. Chen and L. Fu, *ACS Nano*, 2016, **10**, 7189-7196.

[23] D. Geng, B. Wu, Y. Guo, L. Huang, Y. Xue, J. Chen, G. Yu, L. Jiang, W. Hu and Y. Liu, *Proc. Natl. Acad. Sci. U. S. A*., 2012, **109**, 7992-7996.

[24] T. Wu, X. Zhang, Q. Yuan, J. Xue, G. Lu, Z. Liu, H. Wang, H. Wang, F. Ding, Q. Yu, X. Xie and M. Jiang, *Nat. Mater.*, 2016, **15**, 43-47.

[25] I. V. Vlassiouk, Y. Stehle, P. R. Pudasaini, R. R. Unoci, P. D. Rack, A. P. Baddorf, I. N. Ivanov, N. V. Lavrik, F. List, N. Gupta, K. V. Bets, B. I. Yakobson and S. N. Smirnov, *Nat. Mater*., 2018, **17**, 318-322.

[26] B.-B. Jiang, M. Pan, C. Wang, M. H. Wu, K. Vinodgopal and G.-P. Dai, *J. Phys. Chem. C*, 2018, **122**, 13572-13578.

[27] S. Sharma, G. Kalita, R. Hirano, S.M. Shinde, R. Papon, H. Ohtani, M. Tanemura, *Carbon*, 2014, **72**, 66-73.

[28] J. W. Suk, A. Kitt, C. W. Magnuson, Y. Hao, S. Ahmed, J. An, A. K. Swan, B. B. Goldberg and R. S. Ruoff, *ACS Nano*, 2011, **5**, 6916-6924.

[29] L. Fan, J. Zou, Z. Li, X. Li, K. Wang, J. Wei, M. Zhong, D. Wu, Z. Xu and H. Zhu, *Nanotechnol.*, 2012, **23**, 115605 (8pp).

[30] X. Chen, P. Zhao, R. Xiang, S. Kim, J. Cha, S. Chiashi and S. Maruyama, *Carbon*, 2015, **94**, 810-815.

[31] Y. You, Z. Ni, T. Yu and Z. Shen, *Appl. Phys. Lett*., 2008, **93**, 2006-2009.

[32] C. Casiraghi, A. Hartschuh, H. Qian, *Nano Lett*., 2009, **9**, 1433–1441.

# Chapter 4

# The Mo catalyzed graphitization of amorphous carbon: an in situ TEM study

## 4.1 Introduction

The first exfoliated samples of graphene on $SiO_2$ were of a few μm in size and were only suitable for studying basic electronic properties and device fabrication.[1] The development of CVD made it possible for the scalable synthesis of high-quality graphene. The widely used metals as the substrate for graphene synthesis in CVD are Cu, Ni, and Pt.[2–7] In addition to CVD, the thermal annealing of amorphous carbon and the subsequent graphitization in the presence of a catalyst is also popular.[8] Of the various catalytic substrates, Cu has been widely studied due to its low carbon solubility, resulting in to the synthesis of predominantly single layer graphene films. In this context, the catalytic property of the metal like Mo is less explored and there are only a few cases reporting graphene synthesis using the Mo substrate.[9,10] In this work, the fabrication of high-quality few-layer and multilayer graphene using Mo as a catalyst in an in situ TEM experiment is explored. Also the versatility nature of in situ TEM makes it possible to observe the morphological and structural changes during the graphitization process in real-time frame.[11–13] For example, Barriero et al. showed the catalyst-free transformation of amorphous carbon to graphitic sheets.[14] Rosmi et al. observed the synthesis of graphene nanoribbons with Joule heating under the in situ TEM and reveal their current carrying capacity using Cu as a catalyst.[15] Such in situ TEM process has been successfully shown to visualize graphene sublimation and the edge reconstruction phenomenon[14] and can be exceptional in

studying the catalytic property of less explored metals, before designing experiments for large area film growth using CVD.

Though, Cu is a commonly used material as interconnects in circuits, but with the continued miniaturization of circuits, Cu suffers from the problem of electromigration and defects.[17] Mo, on the other hand, suffers less from electromigration due to its very high melting point (2623 $^{o}$C) and brittleness. Besides its higher resistivity compared to Cu, Mo is suitable for high-temperature electronics (300–400 $^{o}$C) and compatible with integrated circuit (IC) manufacturing. This work summarizes the use of in situ TEM Joule heating to study the catalytic property of Mo during the graphitization of amorphous carbon, as well as demonstrating the controlled electromigration of Mo and use it as a solder material. Mo-embedded carbon nanofiber (Mo-CNF) is taken as a starting material for the synthesis of graphene. Due to a bias voltage supplied across the CNF, Joule heat comes into play, leading to graphene formation and the electromigration of Mo.

**4.2 Materials and methods**

CNFs were grown on the edges of a graphite foil (2 cm X 5 cm). Mo foil of 25 μm thickness was used as the Mo source. Graphite foil and Mo foil were kept perpendicular to each other, as shown in schematic Fig. **4.2(a).** Ar+ was bombarded simultaneously onto the edge of graphite and Mo foil using a Kaufmann-type ion gun (Iontech. Inc. Ltd, model 3-1500-100FC). During Ar+ bombardment, Mo and C are ejected and re-deposited on the edge of the graphite foil, leading to the formation of Mo-embedded CNF (Mo–CNF).

All the in situ experiments were carried out using Transmission electron microcope (JEM ARM 200F). Specialized TEM holder EM-Z13200TSCOH from JEOL was used. In this holder, piezo-controlled W STM probe from unisoku scientific instruments was used for

electrical measurement. W probe and sample with Mo-CNF were arranged facing each other as shown in **Fig. 4.1(a)**.

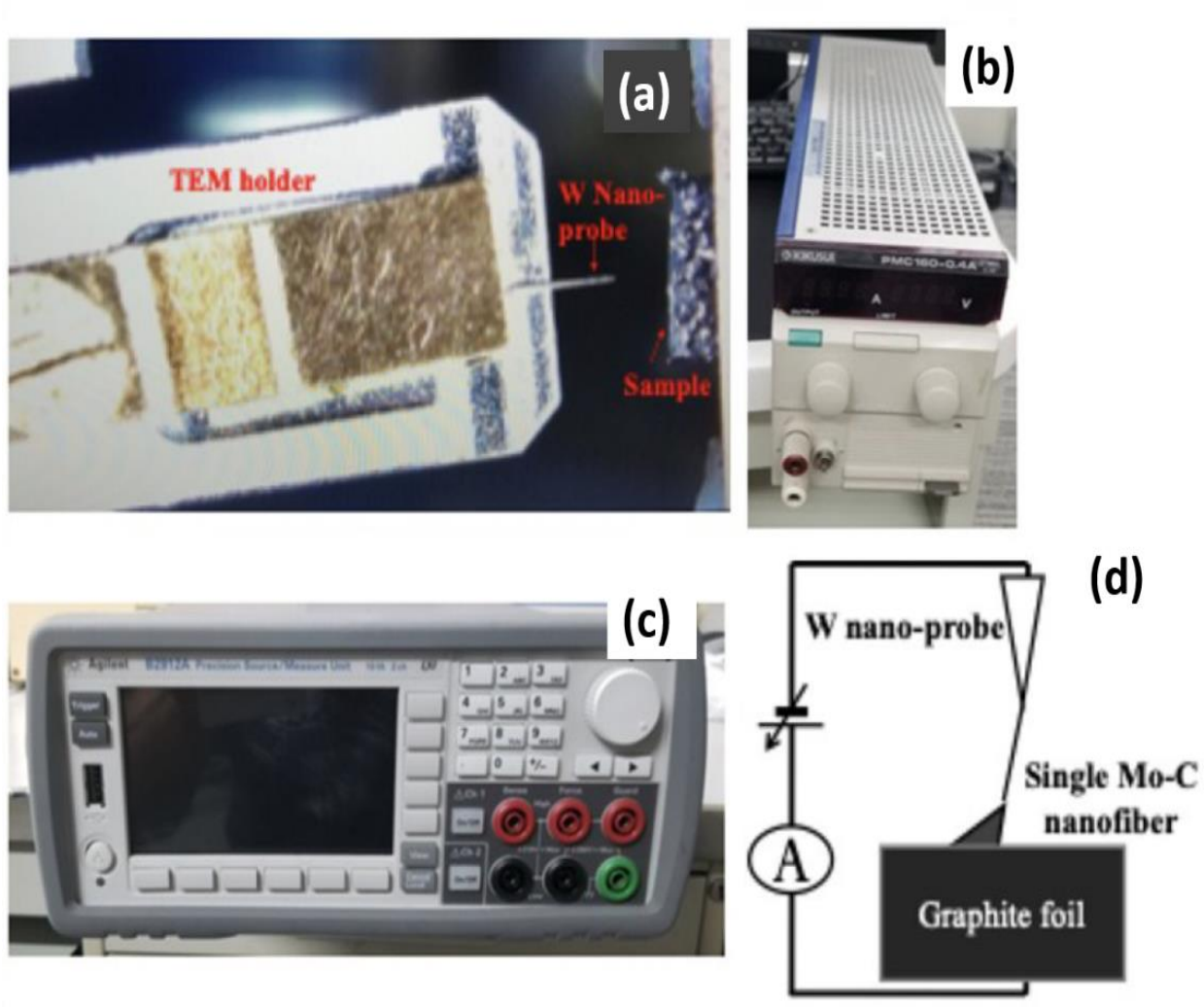


**Figure 4.1** (a) Photographic image showing arrangement of W probe and sample on in situ TEM holder, (b) regulated DC power supply for controlling piezo electric system, (c) Agilent precision source/ Measure unit for supplying bias voltage, (d) schematics showing in situ experimental setup.

Electrical measurements were carried out using Agilent precision source/ Measure unit (B2912A) (Fig. 4.1(c)). As shown by the schematic in Fig. 4.1(d), during in situ experiment, W probe is brought in the contact the Mo-CNF. Regulated DC power supply PMC160-0.4A (kikusui corp.) (Fig. 4.1(b)) was used for controlling the piezo system.

## 4.3 Results and discussion

Mo-embedded CNFs (Mo–CNFs) were synthesized using an ion beam technique. Ar+ ions were co-sputtered on graphite and Mo foil to fabricate the Mo–CNFs, as shown in the schematics of **Fig. 4.2(a)**. The details of the experimental process can be found elsewhere.[11–13,15] Fig. 4.2(b) shows a low-magnification TEM image of a vertical array of CNFs grown on the graphite edge. Fig. 4.2(c) shows a TEM image of typical CNF. CNFs have lengths in the range of 150– 200 nm, featuring thin fibers growing on a cone-like structure. Mo particles were found to be distributed uniformly, embedded inside the amorphous carbon matrix. The inset of Fig. 4.2(c) shows a Mo lattice along with the profile diagram showing a d spacing of 0.22 nm corresponding to the (110) plane (JCPDS Card no. 3-065-7442). After the fabrication of Mo–CNFs at the edge of graphite foil, a small piece of sample was cut and mounted on a TEM holder with the fibers facing towards the probe. For the in situ TEM experiment, a specialized TEM holder (via which bias can be applied) with a W STM probe was used. The TEM holder is connected externally to an electrical measurement setup with a computer where all the I-V measurements were recorded. The position of the probe can be controlled using a nano-manipulator, so that contact can be made between the probe and the CNF.

When the CNF and probe were in contact, a bias voltage was applied via the probe. During the application of a bias voltage, Joule heating came into play, leading to the melting of embedded metal particles and their movement, depending upon the direction of the applied voltage. At the same time the conversion of amorphous CNF to the graphitic form was observed. During the transformation of amorphous carbon to the graphitic form, a change in IV properties was noticed concurrently in the external computer.

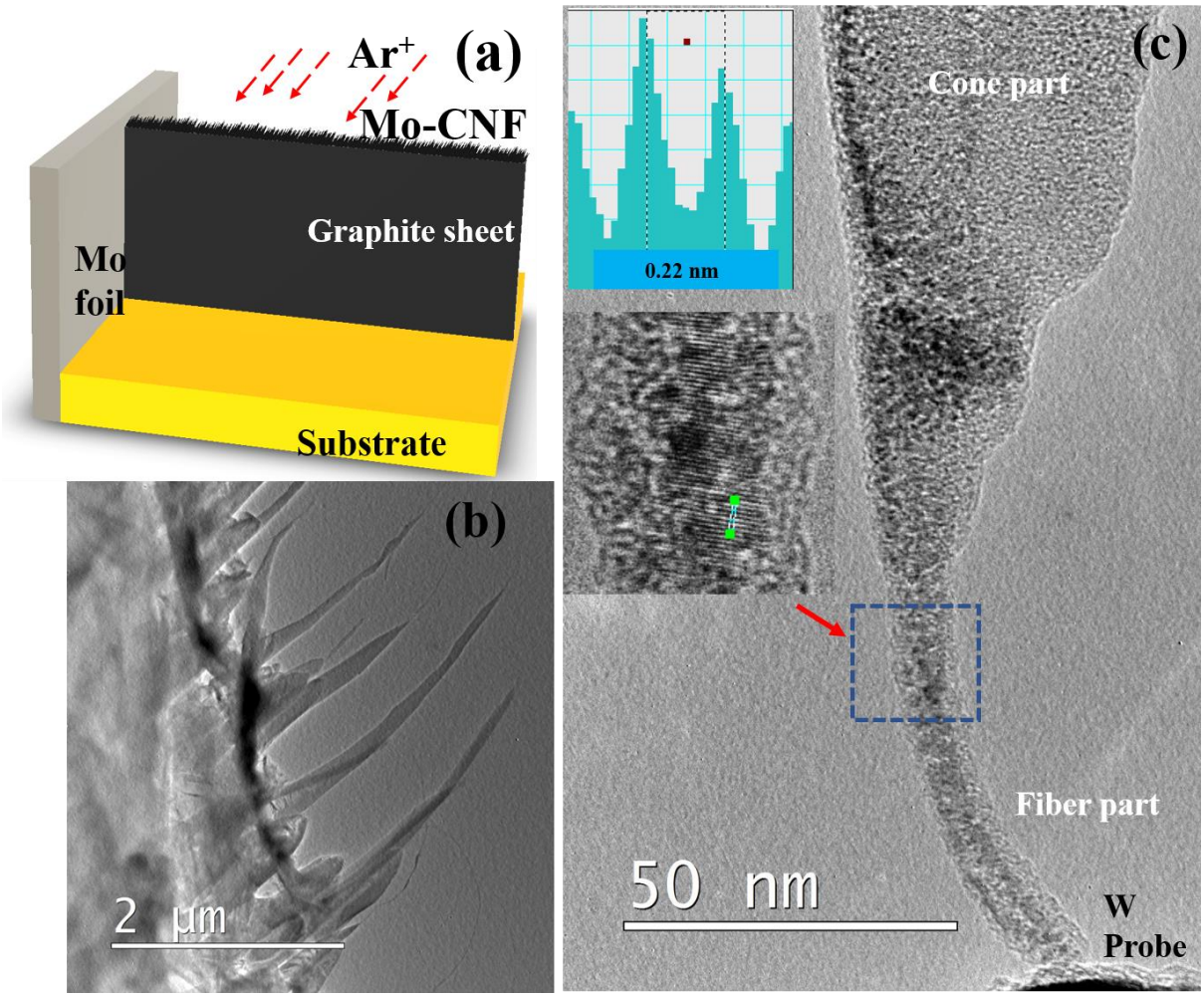


**Figure 4.2** (a) Schematic diagram of the experimental set up showing the fabrication of amorphous Mo–CNF on the edge of graphite foil by the simultaneous bombardment of Ar+ on graphite and Mo foil. (b) A low-magnification TEM image showing vertically upstanding CNFs on the edge of graphite foil. (c) TEM image of a typical Mo-CNF. The inset shows a Mo lattice with a lattice spacing of 0.22 nm corresponding to the {110} plane.

After a suitable CNF had been found, contact was established between the CNF and the W probe, as shown in **Fig. 4.3(a)**. A bias voltage of 0–2.5 V was applied across the probe and the graphite foil sample for 192 s, with the probe taken as the positive terminal and the fiber as the negative terminal. Fig. 4.3(a–h) are snapshots taken from the real time video recorded during the in situ FE processing showing the agglomeration of the Mo particles and their movement due to electromigration. No visible transformation of CNF was observed until 126

s when agglomeration of Mo began. A column of agglomerated Mo could be observed to be moving towards the tip of the fiber near the probe. The collection of Mo around the tip shows that electromigration is the dominant phenomenon, pushing Mo in the direction of the applied electric field. Around 130 s (Fig. 4.3(c)), it was observed that smaller Mo particles were agglomerated into larger particles and the number of nanoparticles on the middle part of the CNF was reduced. An earlier agglomerated metallic column on the tip expanded to a spherical shape around the CNF. From 140 s to 190 s, further agglomeration of Mo was observed around the tip with graphitization clearly observable around the middle of the CNF near the large agglomerated particle.

It was interesting to observe that the Mo bulk particle near the tip acted as a soldering agent connecting the probe and as formed multilayer graphene. During the electromigration and graphitization process of CNF, a sudden change in IV curve was also noticed. From the IV curve of Fig. 4.3(l), a steep increase in current could be seen around 125 s corresponding to the beginning of Mo electromigration at around 125 s (Fig. 4.3(b)). Due to the conversion of amorphous CNF to multilayer graphene, conductivity was suddenly increased, leading to an increase in the value of the current. A very high current of 84.5 μA was observed through the fiber. Fig. 4.3(i) shows a high-magnification TEM image near the tip of the remnant part of CNF attached to Mo, with the graphitic lattice clearly visible. As shown in the line profile (Fig. 4.3(k)) taken around the red rectangular selection of fig. 4.3(i), the magnified image is shown in Fig. 4.3(j), the lattice distance is found to be around 0.35 nm, close to the reported value for graphene. Since the direction of Mo electromigration is from CNF towards to the probe, no significant presence of W was confirmed in the synthesized graphene using electron dispersive X-ray spectroscopy (EDS) (see **appendix Fig. A6**).

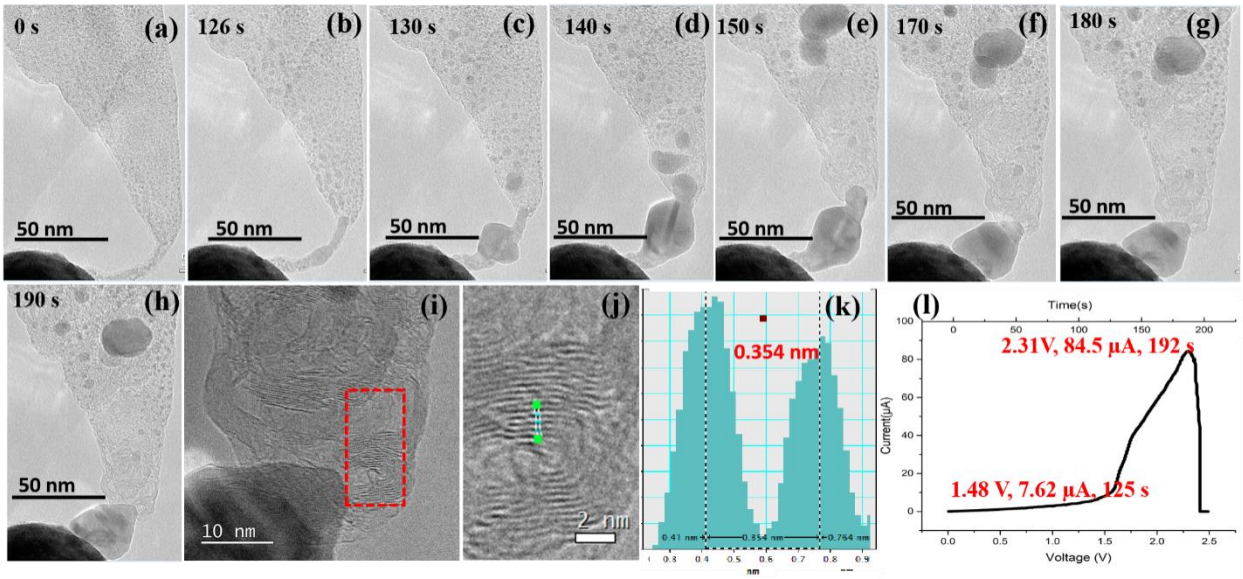


**Figure 4.3** (a–h) Screenshots taken from the real time video recorded during the in situ FE process showing the transformation of Mo–CNF induced by the electromigration of Mo under the application of a bias voltage from 0 to 190 s. (i) A high-magnification image taken at the tip of the fiber near agglomerated metal showing the graphitic layer. (j) A high-magnification image taken around the red rectangular area of (i) showing multilayer graphene and a line profile taken across the layer showing the interlayer distance to be 0.34 nm (k). (l) An IV curve corresponding to (a–h), showing the changes in the electrical properties of Mo–CNF during electromigration and graphitization.

For the further demonstration of the electromigration and graphitization process, another set of experiment was carried out. As longer CNFs are unstable and may break during Joule heating, a constant bias voltage was applied. **Fig. 4.4**(a–d), (e–g), (h–j) and (k–m) show the electromigration of Mo and the graphitization of CNF in 4 different steps. During the 1st step, triangular-shaped Mo crystal started to agglomerate near the probe. With a continuous supply of voltage, a triangular crystal started to grow (Fig. 4.4(c)) and a hexagonal-shaped crystal started to grow, as shown in Fig. 4.4(d). In the 2nd step, it was observed the further electromigration of Mo, and crystals near the probe merged to form a round shape, as shown

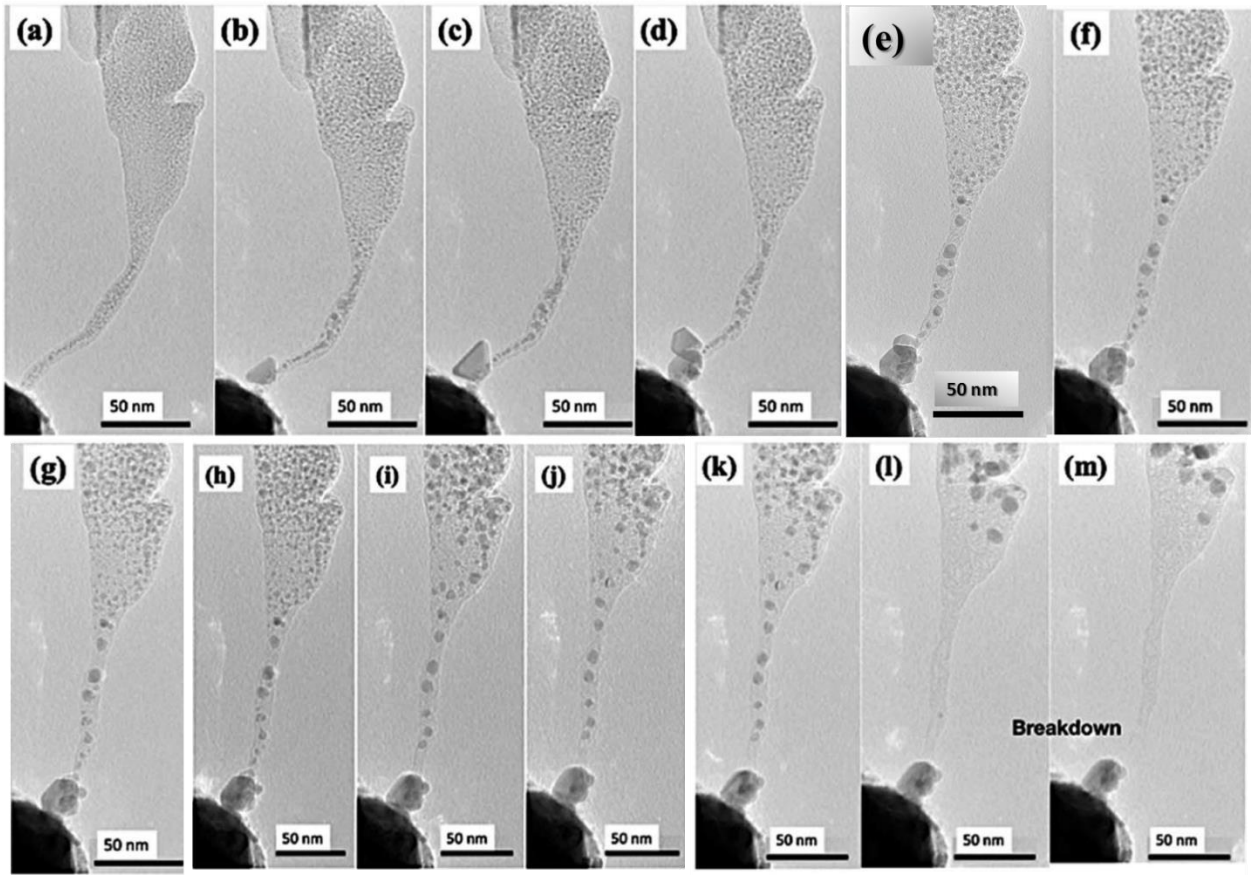


**Figure 4.4** (a–m) Screenshots taken from an in situ TEM video recorded during the FE characterization, showing the gradual formation of a metallic crystal near the tip of the probe followed by the graphitization of the fiber.

in Fig. 4.4(e–g). During the 3rd step (Fig. 4.4(h–j)), further electromigration occurred at the middle part of CNF being partially metal free with graphitization. The 4th step (Fig. 4.4(k–m)) shows complete graphitization of the CNF and its breakage.

**Fig. 4.5(a)** shows that the graphitized CNF got completely separated from the agglomerated Mo particle and got attached to the probe. Fig. 4.5(b and c) show high magnification TEM images taken near the tip of the broken CNF. It can be observed that, 5–10 layers of bamboo-like CNT were formed. Hollow structures are visible in the middle due to electromigration and evaporation of the Mo particle. Core-shell like graphitic structures remained after evaporation of Mo particles, resembling graphitic foam. Graphitization happens

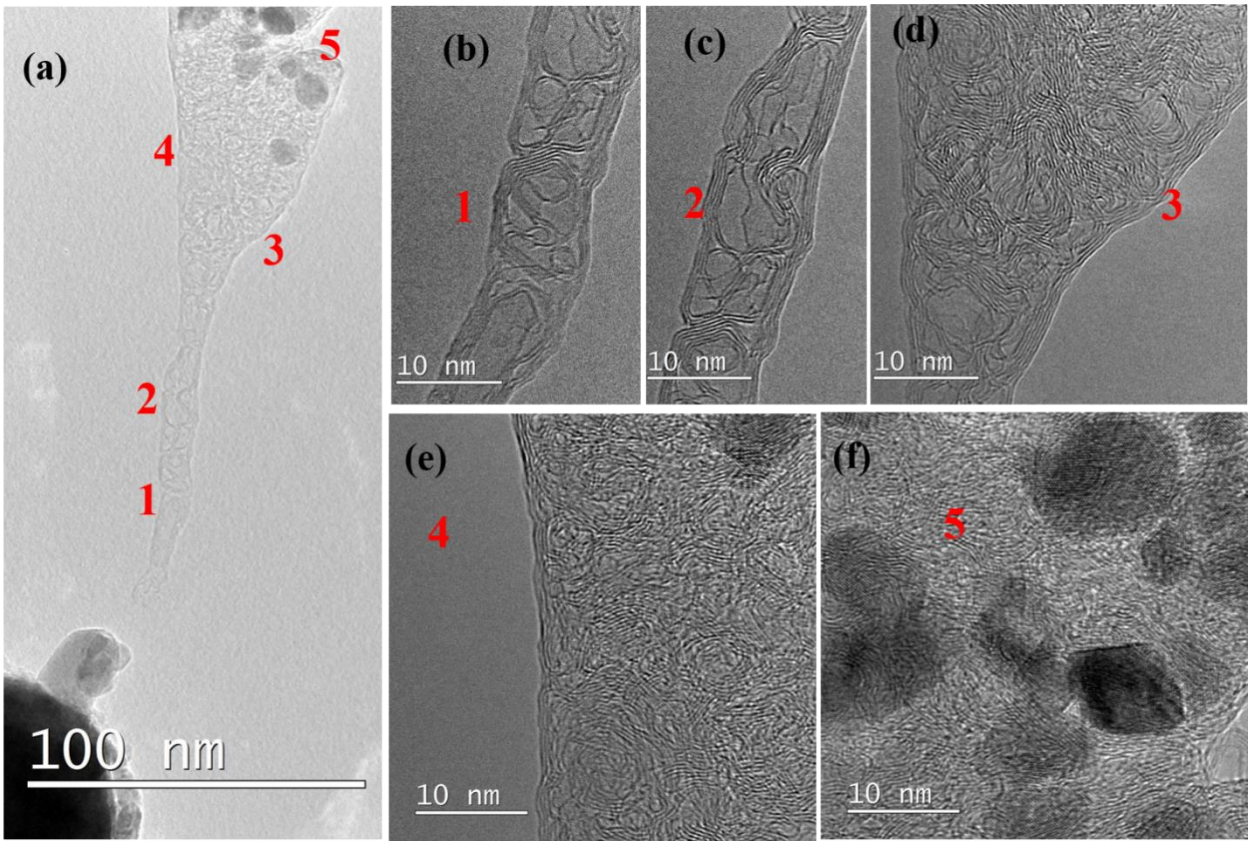


**Figure 4.5** (a) A graphitized CNF separated from the Mo particle, (b) and (c) parts of bamboo-like carbon nanotube with 3–8 layers observed near positions (1) and (2) of (a) respectively. (d) and (f) High magnification TEM images showing porous graphitized structures on the cone part of the fiber near positions (3), (4) and (5) of (a).

around the Mo particle and its sudden evaporation leads to a bamboo-like carbon nanotube structure. Fig. 4.5(d and e) show the upper areas indicated as 3 and 4 in Fig. 4.5(a). The earlier CNF was found to be completely graphitized with the graphene lattice clearly visible and with amorphous carbon present. Earlier smaller Mo particles were completely agglomerated to a size of around 10 nm, as shown in Fig. 4.5(f). It should be noted that the tip of the CNF with its small diameter was converted to bamboolike CNT structures whereas base of the CNF with a large area was graphitized into multilayered graphene. From these observations, it can be clearly stated that Mo acts as an efficient catalyst, leading to the graphitization of amorphous carbon. And agglomerated Mo are collected at the edge of the fiber.

## 4.4 Conclusions

In conclusion, the rarely explored catalytic properties of Mo via in situ TEM studies was demonstrated. It was found that high quality graphene can be synthesized using Mo as a catalyst. It was also noticed that Joule heating induced electromigration in Mo–CNF serves the double purpose of the graphitization of CNF and the controllable agglomeration of Mo near the probe, acting as a soldering agent. This work can be a lead step for further research into Mo-based single-step graphene synthesis and nano-soldering.

## 4.5 References of chapter 4


[1] K. S. Novoselov, A. K. Geim, S. V. Morozov, D. Jiang, Y. Zhang, S. V. Dubonos, I. V. Grigorieva and A. A. Firsov, *Science*, 2004, **306**, 666–669.

[2] X. Li, W. Cai, J. An, S. Kim, J. Nah, D. Yang, R. Piner, A. Velamakanni, I. Jung and E. Tutuc, S. K. Banerjee, L. Colombo and R. S. Ruoff, *Science*, 2009, **324**, 1312–1314.

[3] S. Bae, H. Kim, Y. Lee, X. Xu, J.-S. Park, Y. Zheng, J. Balakrishnan, T. Lei, H. R. Kim and Y. I. Song, Y. –J. Kim, K. S. Kim, B. Özyilmaz, J. –H. Ahn, B. H. Hong and S. Iijima, *Nat. Nanotechnol*., 2010, **5**, 574-578.

[4] S. Sharma, G. Kalita, R. Hirano, S. M. Shinde, R. Papon, H. Ohtani and M. Tanemura, *Carbon*, 2014, **72**, 66–73.

[5] X. Li, W. Cai, L. Colombo and R. S. Ruoff, *Nano Lett*., 2009, **9**, 4268–4272.

[6] K. S. Kim, Y. Zhao, H. Jang, S. Y. Lee, J. M. Kim, K. S. Kim, J. -H. Ahn, P. Kim, J. -Y. Choi and B. H. Hong, *Nature*, 2009, **457**, 706-710.

[7] L. Gao, W. Ren, H. Xu, L. Jin, Z. Wang, T. Ma, L.-P. Ma, Z. Zhang, Q. Fu, L.-M. Peng and H. –M. Cheng, *Nat. Commun*., 2012, **3**, 699 (7pp).

[8] M. Zheng, K. Takei, B. Hsia, H. Fang, X. Zhang, N. Ferralis, H. Ko, Y.-L. Chueh, Y. Zhang and R. Maboudian, *Appl. Phys. Lett*., 2010, **96**, 063110 (3pp).

[9] S. Naghdi, I. Jevremović, V. Mišković-Stanković and K. Y. Rhee, *Corros. Sci*., 2016, **113**, 116–125.

[10] Y. Wu, G. Yu, H. Wang, B. Wang, Z. Chen, Y. Zhang, B. Wang, X. Shi, X. Xie, Z. Jin and X. Liu, *Carbon*, 2012, **50**, 5226–5231.

[11] S. Sharma, M. S. Rosmi, Y. Yaakob, M. Z. M. Yusop, G. Kalita, M. Kitazawa and M. Tanemura, *Carbon*, 2018, **132**, 165–171.

[12] M. Z. M. Yusop, P. Ghosh, Y. Yaakob, G. Kalita, M. Sasase, Y. Hayashi and M. Tanemura, *ACS Nano*, 2012, **6**, 9567–9573.

[13] M. S. Rosmi, Y. Yaakob, S. Sharma, M. Z. Yusop, G. Kalita and M. Tanemura, *IEEE*, 2016, 622–623.

[14] A. Barreiro, F. Börrnert, S. M. Avdoshenko, B. Rellinghaus, G. Cuniberti, M. H. Rümmeli and L. M. K. Vandersypen, *Sci. Rep*., 2013, **3**, 1115 (6pp).

[15] M. S. Rosmi, M. Z. Yusop, G. Kalita, Y. Yaakob, C. Takahashi and M. Tanemura, *Sci. Rep*., 2014, **4**, 7563 (6pp).

[16] J. Y. Huang, F. Ding, B. I. Yakobson, P. Lu, L. Qi and J. Li, *Proc. Natl. Acad. Sci. U. S. A*., 2009, **106**(25), 0103–10108.

[17] C. S. Hau-Riege and C. V. Thompson, *Appl. Phys. Lett*., 2001, **78**, 3451–3453.

# Chapter 5

# Graphitization of Gallium Incorporated Carbon Nanofibers and Cones: In-situ and Ex-situ TEM Studies

## 5.1 Introduction

The synthesis technique of graphitized nanocarbons directly onto the desirable substrates safely and easily at preferably lower temperature is still challenging though the attempt of graphitization of amorphous carbon (αC) was accelerated well after the discovery of graphene. Fujita et al. successfully observed the graphitization of amorphous carbon at the interface of liquid Ga and carbon-contained (αC deposited on a formvar resin film) film, resulting in the formation of large area graphene sheet.[1,2] They showed also the graphene formation by Joule heating for Ga droplet on single-walled carbon nanotubes in in-situ TEM.[3] They demonstrated simultaneously the graphitization of αC pillar with flash motion of Ga droplets incorporated originally into them with focused ion beam induced CVD.[4] But no direct graphitization of αC was recorded under ordinary heating in their experiments. So, for the Ga-incorporated αC system, graphitization process including the graphitization temperature is still a chapter to be explored.

Transmission electron microscopy (TEM) can be a useful technique to elucidate the graphitization process in nanoscale. However, it remained always a problem to prepare the samples which should be thin enough to transmit the incident electrons. For this purpose, ion-

induced conical structures and CNFs fabricated on the edge of a thin carbon foil are known to be promising.[5-11] They are fabricated just by the ion irradiation to the carbon substrate without any catalyst and intentional heating. Usually, the ion induced CNFs are amorphous in crystalline state, and the composition of cones and CNFs can be controlled by a supply of the other element during the ion irradiation. They are thin enough, so that the carbon foil cut into a small piece can be used as a sample for TEM analyses without any post treatment, such as thinning process of the sample. In what follows, we will challenge this interesting topic, namely, the elucidation of the graphitization process, using simple vacuum annealing as well as in-situ TEM for Ga incorporated carbon nanofibers (Ga-CNF) and cones prepared by ion irradiation to carbon foils with a simultaneous supply of Ga.

## 5.2 Materials and methods

Commercially available carbon (graphite) foils (25 mm x 5 mm x 200 μm) was used to synthesize the Ga-CNFs by ion beam irradiation using a Kaufmann-type ion gun (Iontech. Inc. Ltd., model 3-1500-100FC). The graphite foil with its edge and small chunk of Ga were mounted perpendicular to each other were co-sputtered with argon ions ($Ar^+$) at $45^0$ from normal to carbon foil surface for 60 minutes without any intentional heat supply [**Fig. 5.1(a)**]. The ion energy applied was 600 eV and the beam current was maintained at 8 mA. One of the most important merits to use the metal-incorporated CNFs fabricated on an edge of a carbon foil is the comfortness in the sample preparation for TEM. After the growth. the carbon foil sample was cut into a small piece of about 2 mm x 5 mm to set onto the TEM sample holder without any post treatment.

The formation of the CNFs and cones was confirmed on the samples thus prepared first by using a scanning electron microscope (SEM; -JSM 5600). The samples were then heated in a

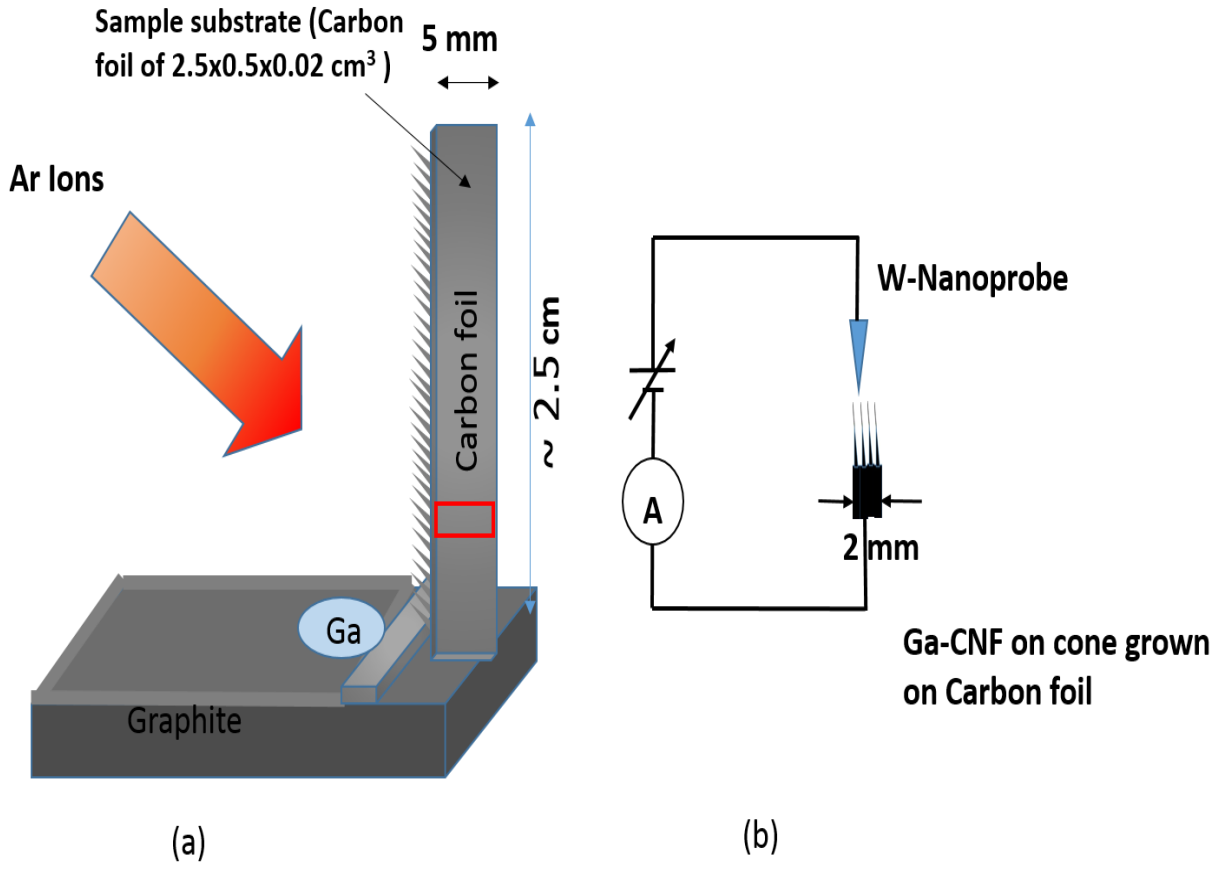


**Figure 5.1**. Schematics of (a) experimental arrangement to show the Ion beam irradiation for the synthesis of Ga-CNF and cones, and (b) the circuit diagram for the in situ I-V measurements. A red rectangular in (a) indicates a sampling piece used for the TEM observation in (b).

vacuum heater at different elevated temperatures in order to explore out the graphitization temperature of α-C in the form of CNFs and cones under the catalysis of incorporated Ga. The ex-situ and in-situ TEM characterizations were performed using TEM (JEM-ARM200F). For the in-situ TEM analysis, the samples were set on a sample holder (EM-Z02154T) equipped with a tungsten nano-probe whose motion was controlled by piezo to measure the current-voltage (I-V) properties [(Fig. 5.1(b)]. During this I-V measurement, structural transformation (graphitization) of amorphous CNF was observed simultaneously. The Raman analysis was done with an NRS 3300 laser Raman spectrometer with a laser excitation energy of 532.08 nm. The Raman measurement was done with an extra care using the spot size of 1 μm while

observing the optical microscope image at x100 magnification (objective) to analyze only the edge of the foil.

### 5.3 Result and Discussion

**Fig. 5.2 (a)** shows a typical SEM image of an as-synthesized Ga-CNF confirming the growth of a CNF on the tip of each cone which is also confirmed by a low magnification TEM image shown in Fig. 5.2(b). Similar to the other metal included CNF cases,[5-11] there was observed growth of no more than one CNF on respective cone tips. The growth mechanism of ions induced CNFs is explained in detail elsewhere.[12,13] Fig. 5.2(c) reveals a typical energy dispersive x-ray spectroscopy (EDS) spectrum obtained at a tip region of a cone, confirming the presence of Ga and the Ga content was estimated to be about 12 at%. Fig. 5.2(d) shows a magnified TEM image taken at a tip region of a cone, showing that a black contrast part is dispersed in the amorphous-like matrix which otherwise be rare in non-heated samples of Ga-CNFs. A careful inspection of Fig. 5.2(d) revealed the local crystallization mainly at the black contrast part, as is exemplified in the inset in Fig. 5.2(d). Fig. 5.2(e) shows an intensity profile obtained along the line at the crystallized region in Fig. 5.2(d), disclosing the inter-planer spacing of 0.295 nm which corresponds to Ga (111). Thus, a number of very tiny Ga nanoparticles (NPs) were dispersed in the matrix of amorphous carbon of these CNFs and cones. The Ga lattice was not always prominent at the whole black part. This may be explicable due to the elevation in the melting point specific for Ga NPs. Unlike other metals, nanocluster form of Ga is found to possess higher melting point than bulk Ga due to its covalent bonding property different from that of other metals.[14-18]

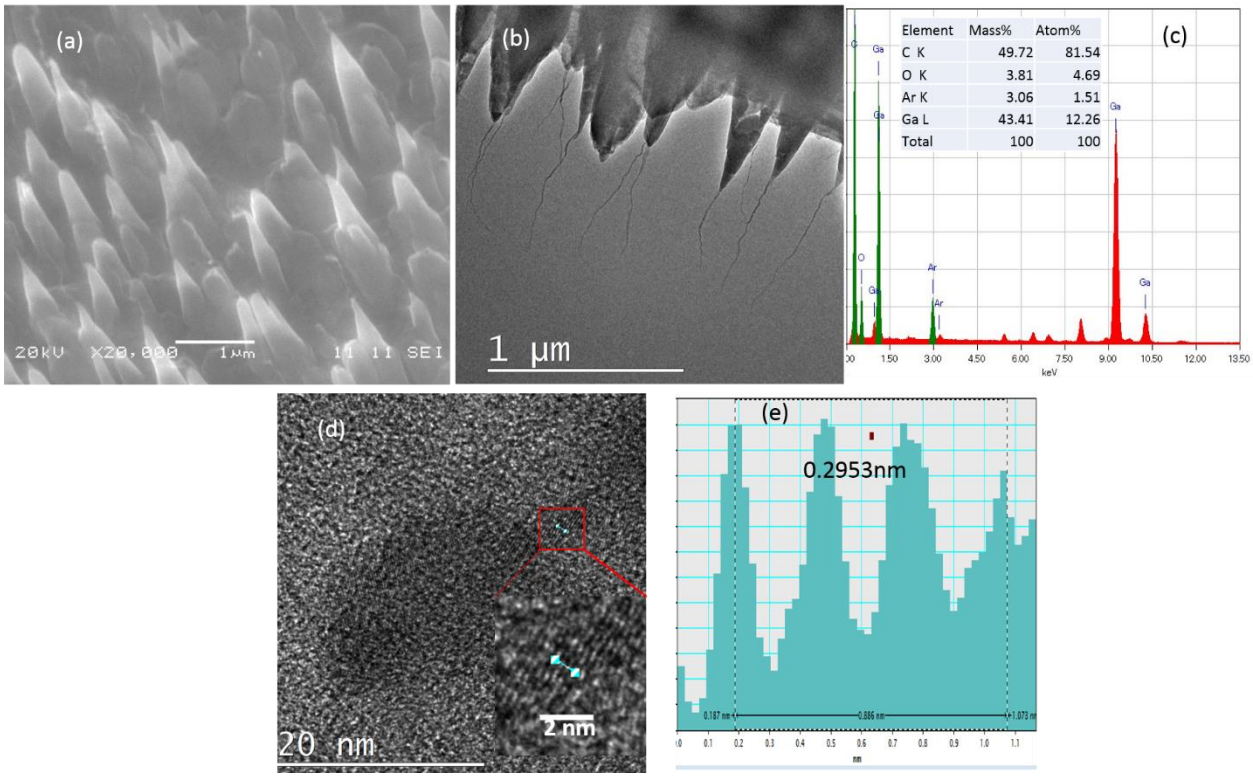


**Figure 5.2**. (a) A typical SEM image of as synthesized Ga-CNF and cones, (b) low magnification TEM image showing the distinct growth of Ga-CNFs and cones, (c) the EDS spectrum of a Ga-CNF with the composition of different elements in the inset, (d) high magnification TEM image with visible Ga lattices in the Ga-CNF with enlarged image inset, and (e) intensity profile diagram to show the inter-planar spacing of Ga lattices in fig. (d).

In order to observe the graphitization of thus synthesized Ga-CNFs and cones and to estimate the temperature of graphitization, these Ga-CNFs and cones were annealed at vacuum at different temperatures. When the annealing temperatures were lower than 500 $^{o}$C, almost no structural change was observed as shown in **Fig. 5.3(a)**. While annealing at 600 $^{o}$C, several particles with black contrast were found to be appeared at the outer surface of CNFs and cones as shown in Fig. 5.3(b). For some of those particles indicated by arrow-heads, the lattice fringes with inter-planar spacing 0.226 nm corresponding to Ga (200) were observable confirming that those protruding particles were Ga NPs. Meanwhile, the lattice fringes corresponding to graphite (002) were also observed near the Ga NPs, suggesting the local graphitization occurred.

Regarding the sample annealed at 700 $^{o}$C, as shown in Fig. 5.3(c), the size of Ga NPs was larger compared with that in Fig. 5.3(b), suggesting the agglomeration of Ga NPs. It should be noted that graphitization was prominent at the bumped region indicated by a rectangular in Fig. 5.3(c), where a Ga NP would have been located. Though the TEM contrast at the bumped region was not black, the black contrast NPs were considered still be inside the cone, suggesting the evaporation of Ga started to occur at the cone surface. The structure of a cone annealed at 800 $^{o}$C is shown in Fig. 5.3(d), disclosing the long-range graphitization not only at the surface but also in the cone. It should be also noted that Ga NPs got evaporated away almost completely. Fig. 5.3(e) shows the intensity profile of the fringe at the encircled region in Fig. 5.3(d), confirming the interlayer spacing of 0.336 nm corresponding to that of graphite (002). For the further confirmation of the graphitization, Raman analysis was performed at the edge of this sample heated at 800 $^{o}$C. The Raman spectrum distinctly showed the separated D and G peaks with a distinct 2D peak (Fig. 5.3(f)), which confirmed the graphitization of amorphous carbon induced by the catalysis of Ga NPs.

These above-described observation on the graphitization behavior at different temperatures performed for vacuum-annealed samples ex-situ, set a tentative graphitization temperature for Ga-CNFs and cones. With the knowledge of this temperature dependence of the graphitization, it would be interesting to investigate the change in the electrical property due to the graphitization by in-situ TEM. An in-situ TEM observation for a Ga-CNF during its current-voltage (I-V) measurement in the range from 0 to 4.5 V with an increment of voltage at 2 V/min was performed. **Fig. 5.4(a)-(h)** show a series of TEM images snapshotted from the real time video recorded during the process with the elapsed time from the voltage applications, along with the I-V characteristics [Fig. 5.4(i)]. During the structural observation, there was no distinct

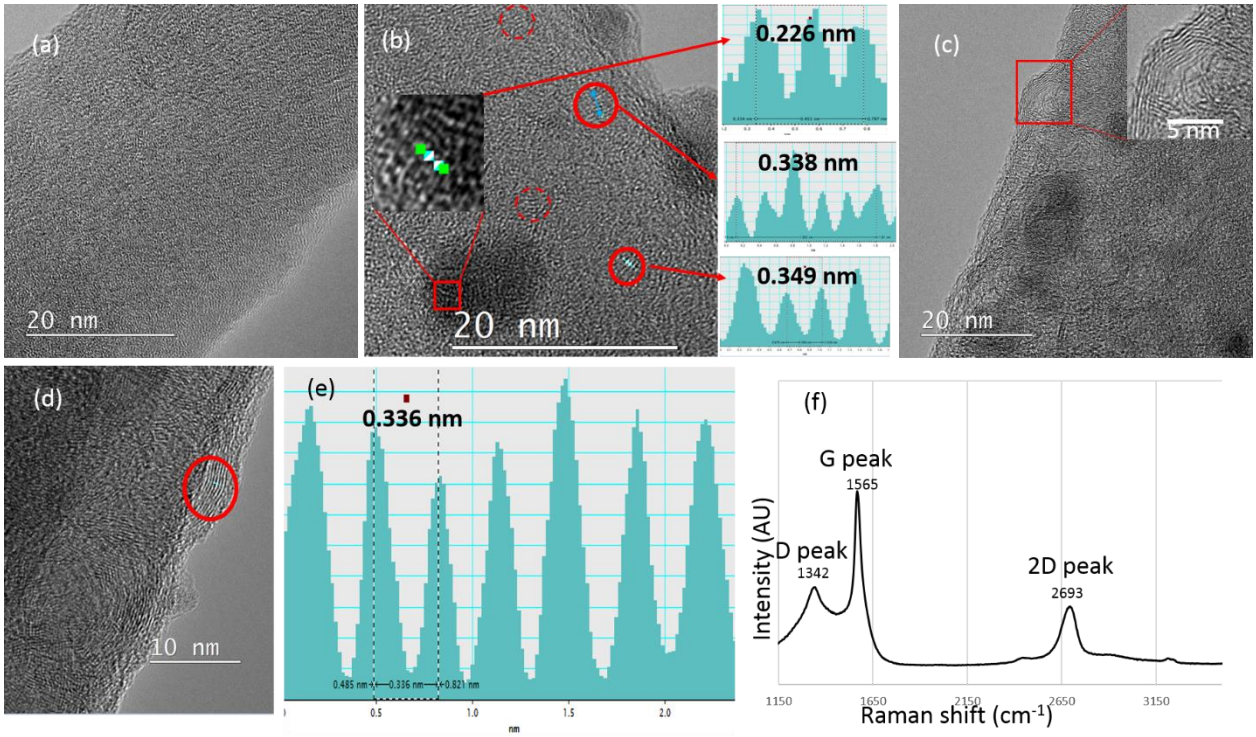


**Figure 5.3**. High magnification TEM images of Ga incorporated cone annealed ex-situ at (a) 500 $^0$C, (b) 600 $^0$C, (c) 700 $^0$C and (d) 800 $^0$C. (a) The image reveals neither the agglomeration of Ga nanoclusters nor the graphitization. (b) The image shows the distinct agglomeration of Ga nanoclusters with partial graphitization. Insets show the enlarged Ga lattices and the intensity profile of the Ga lattice. The intensity profile of the graphitic layers marked by solid red circles are also shown. The graphitic layers are visible also at several places exemplified by dashed red circles. (c) The image shows the agglomerated Ga nanoclusters with intermediate graphitization with enlarged graphitized region inset. (d) The image shows the high level of graphitization with complete evaporation of agglomerated Ga nanoclusters. (e) Intensity profile of graphitic layers marked by a red circular in fig. (d). (f) Raman spectrum obtained at the edge of the carbon foil after vacuum annealing at 800 $^0$C, verifying the graphitization of amorphous carbon under the catalysis of Ga NPs.

change noticed up to 102 sec. At around 103 sec, the small sized black contrast of Ga NPs disappeared, indicating their evaporation due to Joule heating. This disappearance of the black contrast, namely, the evaporation of Ga NPs, became more prominent with an increase of voltage (with an increase of time). Finally, all the Ga NPs in the form of black contrasts,

disappeared and suddenly the breakdown of the CNF took place from around its middle at 118 sec.

From the I-V measurement [Fig. 5.4(i)], the non-linear and steep increase in CNF current with applied voltage is seen, suggesting the conductivity increase due to the structural change of the CNF-tipped cone. It would be difficult to detect the slight change in structure like the local graphitization observed in Fig. 5.3(b) and 5.3(c) in the dynamic TEM of this high magnification. After the evaporation of Ga NPs was detectable in the dynamic TEM, especially after ~107 sec, a dramatic but unstable increase in current was prominent. The maximum current reached 15.4 µA just before the breakdown of the CNF. Fig. 5.4(j) and 5.4(k) show a

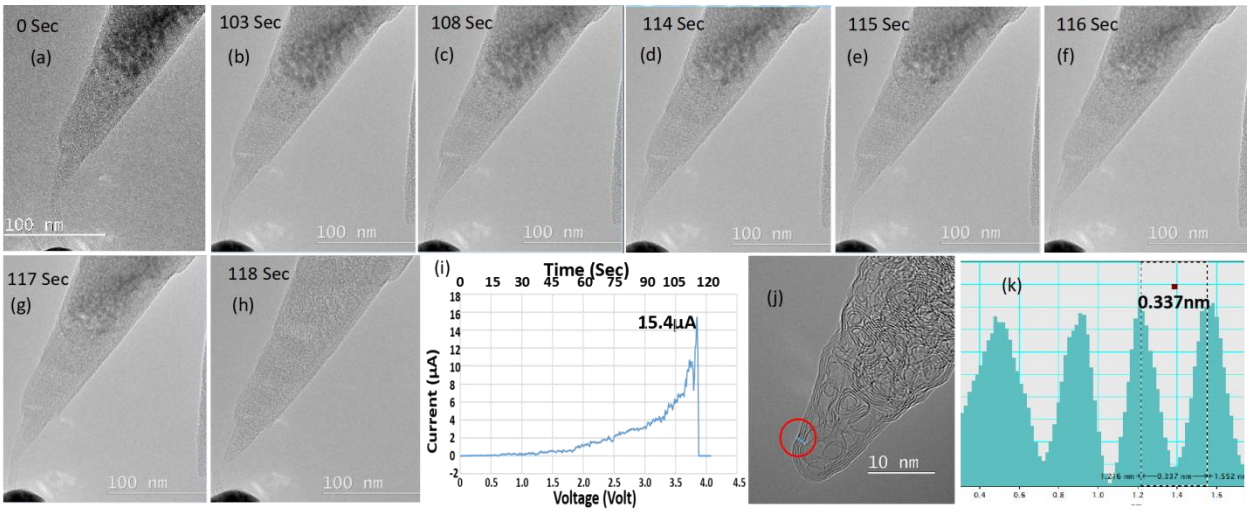


**Figure 5.4.** (a) A still image of a Ga-CNF and cone with the probe arrangement before starting the in situ operation on a fiber. (b)-(h) Still images of different stages during the in situ operation of the same fiber in fig. (a) taken from the recorded real time video. (i) I-V diagram of the in-situ operation of the fiber in fig. (a). (j) High magnification TEM image of tip of the cone after the in situ operation showing distinct graphitization, and (k) intensity profile of the marked graphitized region of fig. (j).

high resolution TEM images taken at the broken part of the CNF and an intensity line-profile measured along the line shown in Fig. 5.4(j), respectively. The intensity line-profile shows the

inter layer distance of 0.337 nm which certainly corresponds to that of graphene (002), thus confirming that the broken part of the CNF was well-graphitized. The graphitization occurred in relatively long-range compared with the very local graphitization formed under the other conditions tested here.

## 5.4 Conclusions

In summary, Ga incorporated CNFs and cones could be grown through the ion irradiation method in contrast to the quite low melting point of Ga. For the material system of the mixture of Ga and amorphous carbon, the graphitization temperature was demonstrated for the first time by the ex-situ heating experiment. In-situ TEM demonstrated that the increase in conductivity was accelerated with the graphitization. This combination of the in-situ and ex-situ TEM observations is believed to be promising to understand deeper the graphitization process and electrical property.

## 5.5 References for chapter 5


[1] J. Fujita, R. Ueki and Y. M. T. Ichihashi, *J. Vac. Sci. Technol. B*, 2009, **27** (6), 3063-3066.

[2] J. Fujita, Y. Miyazawa, R. Ueki, M. Sasaki and T. Saito, *Jpn. J. Appl. Phys.*, 2010, **49**, 06GC01 (5pp).

[3] R. Ueki, T. Nishijima, T. Hikata, S. Ookubo, R. Utsunomiya, T. Matsuba and J. Fujita, *Jpn. J. Appl. Phys.*, 2012, **51**, 06FD28 (5pp).

[4] J. Fujita, T. Ichihashi, S. Nakazawa, S. Okada, M. Ishida and Y. Ochiai, *Appl. Phys. Lett.*, 2006, **88**, 083109 (3pp).

[5] M. Z. M. Yusop, P. Ghosh, Y. Yakob, G. Kalita, M. Sasase, Y. Hayashi and M. Tanemura, *ACS Nano*, 2012, **6**, 9567-9573.

[6] Y. Yakob, M. Z. M. Yusop, C. Takahashi, M.S. Rosmi, G. Kalita and M. Tanemura, *RSC Adv.,* 2015, **5**, 5647-5651.

[7] C. Takahashi, Y. Yaakob, M. Z. M. Yusop, G. Kalita and M. Tanemura, *Carbon,* 2014, **75**, 277-280.

[8] S. Sharma, M. S. Rosmi, Y. Yaakob, M. Z. M. Yusop, G. Kalita, M. Kitazawa and M. Tanemura, *Carbon,* 2018, **132**, 165-171.

[9] Y. Yaakob, M. Z. Yusop, C. Takahashi, G. Kalita, P. Ghosh and M. Tanemura, *Jpn. J. Appl. Phys., 2013,* **52**, 11NL01 (4pp).

[10] Y. Yaakob, Y. Kuwataka, M. Z. M. Yusop, S. Tanaka, M. S. Rosmi, G. Kalita and M. Tanemura, *Phys. Status Solidi B,* 2015, **252**, 1345-1349.

[11] S. Sharma, B. P. Jaisi, M. I. Araby, S. Elnobi, M. E. Aryan, G. Kalita and M. Tanemura, *RSC Adv.*, 2019, **9**, 34377-34381.

[12] M. Tanemura, M. Kitazawa, J. Tanaka, T. Okita, R. Ohta, L. Miao and S. Tanemura, *Jpn. J. Appl. Phys.*, 2006, **45-3B**, 2004-2008.

[13] M. Tanemura, T. Okita, J. Tanaka, M. Kitazawa, K. Itch, L. Miao, S. Tanemura, S. P. Lau, H.Y. Yang, and L. Huang, *IEEE Trans. Nanotecnol.*, 2006, **5**, 587-594.

[14] F. Ercolessi, W. Andreoni and E. Tosatti, *Phys. Rev. Lett.,* 1991, **66**, 911-914.

[15] M. Schmidt, R. Kusche, W. Kronmüller, B. V. Issendorff and H. Haberland, *Phys. Rev. Lett.*, 1997, **79**, 99-102.

[16] G. A. Breaux, R. C. Benirschke, T. Sugai, B. S. Kinnear and M. F. Jarrold, *Phys. Rev. Lett.*, 2003, **91**, 215508 (4pp).

[17] A. A. Shvartsburg and M. F. Jarrold, *Phys. Rev. Lett.,* 2000, **85**, 2530-2532.

[18] S. Chacko, K. Joshi and D.G. Kanhere, *Phys. Rev. Lett.,* 2004, **92**, 135506 (4pp).

# Chapter 6

# Conclusions and Future works

## 6.1 Overall conclusions

Thus, the entire works that followed in the previous chapters of this thesis explored the graphitization process in detail. Over the countless parameters that affect the graphitization mechanism, the choice of catalytic substrate and the effect of flow rates of the carrier gases was found to play vital role while tuning the growth into isotropic in CVD. Furthermore, the convenient and feasible way of observation of graphitization of nanocarbons in nanoscale was also essential to understand the mechanism in detail. In what followed in the previous chapters of this thesis tempted to explore this mechanism in nanoscale so that the idea can be employed in other route of graphene synthesis like CVD.

The idea of tuning the growth into isotropic is found to be promising and lead step to eliminate the issue of graphene grain boundaries in CVD graphene by self-smooth stitching mechanism and hence the growth of larger isotropic single crystals graphene became possible compared to their anisotropic counterparts. Quantitative measurement showed the size of these round isotropic single crystals was around 410 μm, almost 10 times larger than the hexagonal crystals (around 40 μm only) synthesized in all other identical conditions except the flow rate of carrier gases. At the same time, a round isotropic crystal covers about 21% greater area compared to a hexagonal anisotropic counterpart even of equal dimension (distance between the two extremities). The isotropic graphene crystals synthesized through the route mentioned in chapter 3 were characterized to be single crystalline, single layered and of the equivalent quality of their anisotropic analogs which were shown to be synthesized with other routes. So,

this low flow rate of carrier gases was considered to play a role not only to increase the concentration of PE precursor molecules but also it led the precursor molecules to interact with the Cu substrate molecules for longer duration and tuned the growth process.

In situ TEM for characterizing the FE properties of metal incorporated CNFs is always remained promising to explore the graphitization process in nanoscale. Mo with its very high melting point (2623 $^{o}$C) can be suitable for the high temperature electronics and compatible with integrated circuit (IC) manufacturing besides of its higher resistivity as compared to that of Cu. The in situ TEM Joule heating of Mo incorporated CNFs (Mo-CNFs) not only demonstrated the catalytic action of this less studied metal for graphitization but also demonstrated its controlled electromigration approving it as a potential candidate of solder material. The graphitized remnant of Mo-CNF was found to be able to handle a current as high as 84.5 μA before their break down at a biasing voltage as low as 2 V during the FE process. The formation of bamboo like CNT structure at the tip and multilayered graphene at the base of Mo-CNFs after the FE process approved Mo as a potential catalytic agent for graphitization which otherwise was explored less for the purpose.

On the other hand, what followed in chapter 5, Ga with its low melting point near to the room temperature showed entirely contrasting results in graphitization. The well-stablished fact that the liquid state of metal favors graphitization was challenged by Ga due to its some anomalous characters. The Ga NPs unlike to those of other metals and general perception were found to have higher melting point than its bulk form and exist in amorphous state. But on increasing the temperature, these NPs were found to be promising in graphitization. The graphitization process for Ga-CNFs was explored both in in situ Joule heating as well as in normal vacuum heating and the graphitization temperature in the vicinity of Ga was found as low as 600 $^{o}$C for the first time. The observation of graphitized Ga-CNFs under TEM as well as the graphitization during the in situ FE process established Ga too a candidate material in

the catalysis of graphitization. Moreover, the formation of long ranged graphitized nanocarbons under the in situ TEM processing can be a lead step towards the elimination of graphene grain boundaries in the field of graphene synthesis.

### 6.2 Future Prospective

As discussed throughout this work, graphene is the best 2D material that can be used as future material. In addition to the works described in this thesis, the following additional processing can be carried out in the future.

The nano-level study of graphitization mechanism in the catalysis of Mo and Ga made clear that they also have potentials to be used in this field. In my perspective, the use of an alloy of Ga and Cu in CVD process can introduce some revolutionary ideas in the field of graphene synthesis. Furthermore, it can be better if the same process is done on the NPs of these metals coated on a viable substrate like $SiO_2$ leading towards the transfer free graphene synthesis. The tuning process of CVD graphene growth into isotropic needs to be more explored with more factors including the actual change in pressure inside the CVD tube due to the flow of low stream of carrier gases.

# Appendix

1. **Figure A1**. OM images of samples revealing the two points measurement of Graphene domain sizes along their longest diagonal at three different regions of (A1-C1) Expt 1, (A2-C2) Expt 2 and (A3-C3) Expt 3 of **chapter 3**. Scale bars: 100 µm.

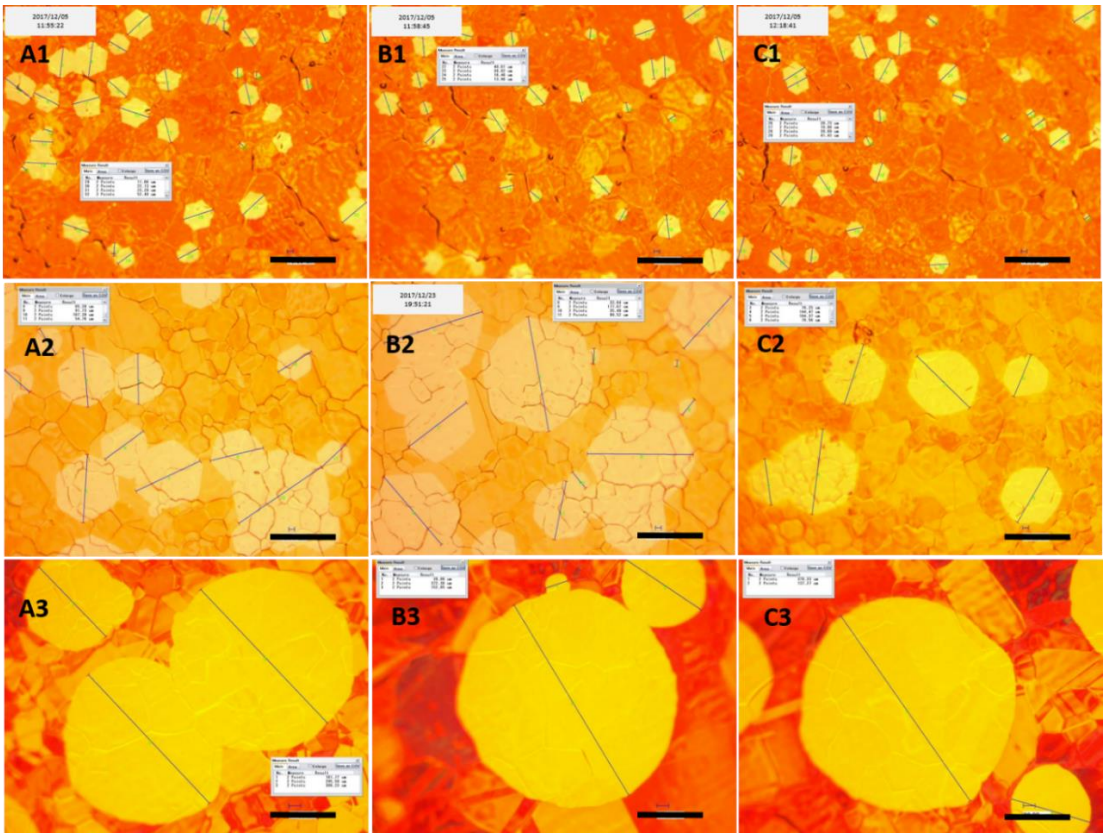


2. **Table A1.** Calculation of Average graphene domain size and growth speed of three different regions of three samples in fig. A1.

| Sample of Expt. | Region | No. of domains measured | Average Graphene domain size (µm) | Grand average (µm) | Average growth speed (µm/min) |
|---|---|---|---|---|---|
| 1 | A1 | 32 | 36.9059 | 33.7342 | 0.2765 |
| | B1 | 25 | 32.8636 | | |
| | C1 | 29 | 30.9848 | | |
| 2 | A2 | 11 | 89.4536 | 98.4779 | 0.8072 |
| | B2 | 11 | 103.7255 | | |
| | C2 | 6 | 105.4017 | | |
| 3 | A3 | 3 | 255.1967 | 230.5825 | 1.8900 |
| | B3 | 3 | 187.8233 | | |
| | C3 | 2 | 257.8000 | | |

3. **Figure A2**. SEM images of three different regions of samples of (A1-C1) Expt 1, (A2-C2) Expt 2 and (A3-C3) Expt 3 of **chapter 3** with respective area and number of graphene domains counted.

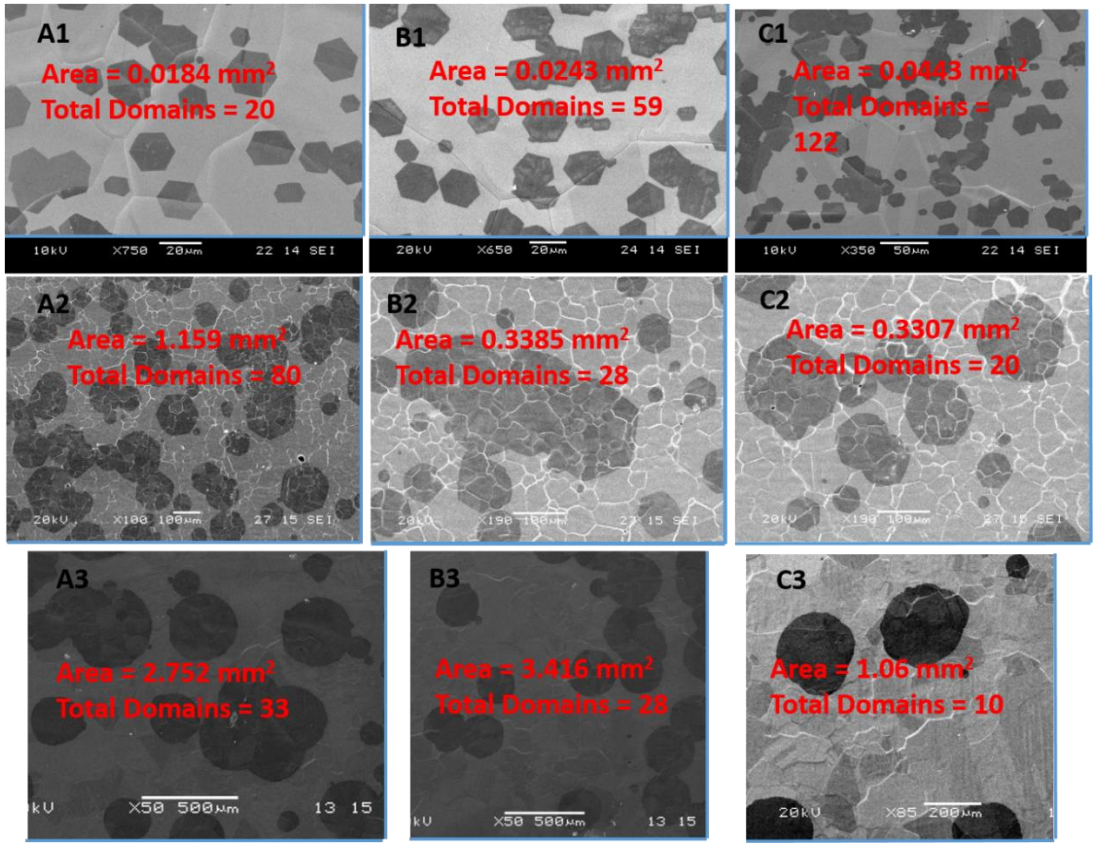


4. **Table A2**. Calculation of graphene domains density at three different regions of three samples in fig. A2.

| Sample of Expt. | Region | Area($mm^2$) | Graphene Domains Count | Domains Density ($mm^{-2}$) | Average ($mm^{-2}$) |
|---|---|---|---|---|---|
| 1 | A1 | 0.0184 | 20 | 1086.9565 | 2089.6300 |
| | B1 | 0.0243 | 59 | 2427.9835 | |
| | C1 | 0.0443 | 122 | 2753.9503 | |
| 2 | A2 | 1.1590 | 80 | 69.0250 | 70.7402 |
| | B2 | 0.3385 | 28 | 82.7179 | |
| | C2 | 0.3307 | 20 | 60.4778 | |
| 3 | A3 | 2.7520 | 33 | 11.9913 | 9.8740 |
| | B3 | 3.4160 | 28 | 8.1967 | |
| | C3 | 1.0600 | 10 | 9.4340 | |

5. **Figure A3.** OM images of annealed samples to determine Cu grains size at three different regions of (a1-c1) Expt 1, (a2-c2) Expt 2 and (a3-c3) Expt 3 of **chapter 3**. (Scale bars: 100 µm)

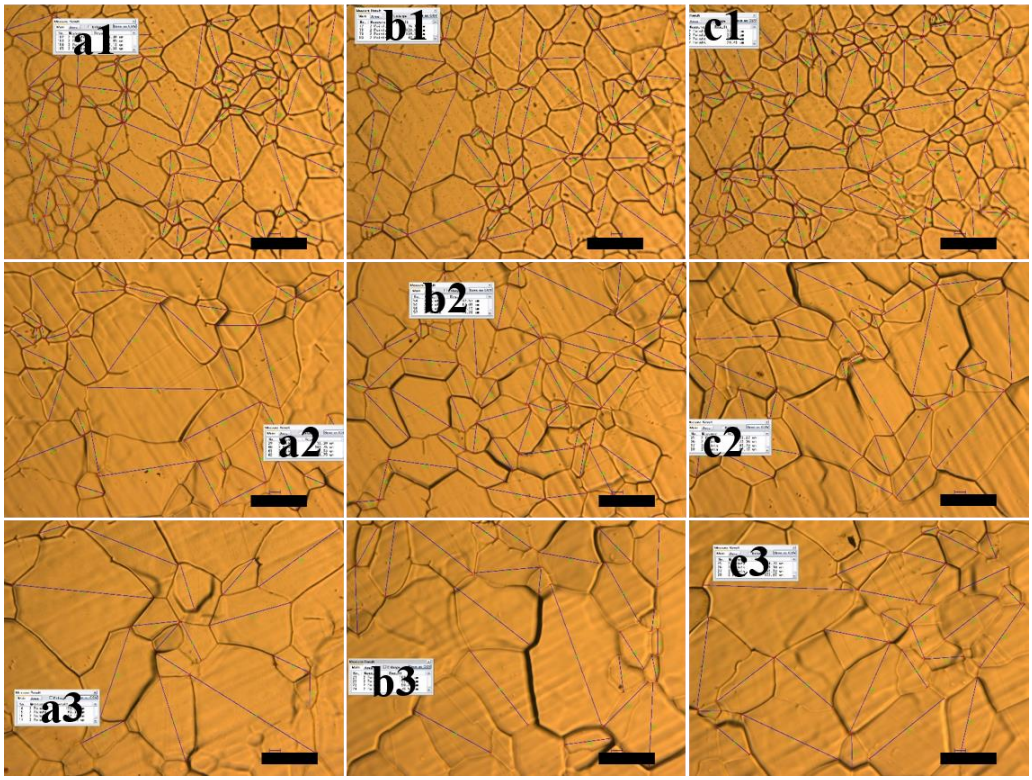


6. **Table A3.** Calculation of Average Cu-grains sizes at three different regions of three samples in fig. A3.

| Sample of Expt. | Region | No. of Grains | Average Cu-grain size (µm) | Grand Average (µm) |
|---|---|---|---|---|
| 1 | a1 | 123 | 50.3309 | 54.8547 |
| | b1 | 80 | 63.0086 | |
| | c1 | 105 | 53.9414 | |
| 2 | a2 | 42 | 79.3105 | 79.8343 |
| | b2 | 57 | 74.0811 | |
| | c2 | 38 | 89.0429 | |
| 3 | a3 | 17 | 122.6188 | 110.5355 |
| | b3 | 24 | 108.2763 | |
| | c3 | 28 | 105.1357 | |

7. **Figure A4.** EBSD images of Annealed samples revealing the comparative Cu – grains size of (a) Expt 1, (b) Expt 2 and (c) Expt 3 of **chapter 3**

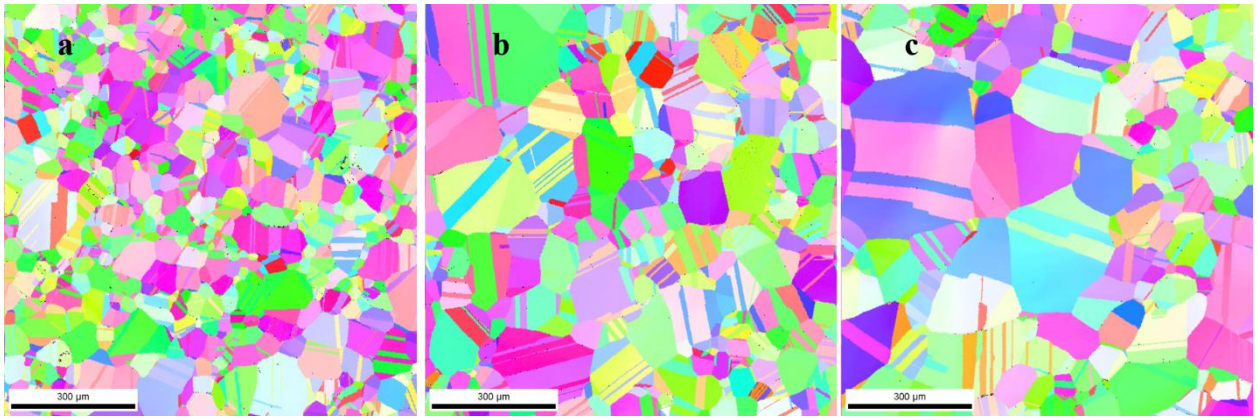


8. **Figure A5.** OM images of transferred graphene crystals on $SiO_2$/Si of (A) Expt 1, (B) Expt 2 and (C) Expt 3 of **chapter 3** with 20 points at which Raman spectra are taken for D/G and 2D/G ratios.

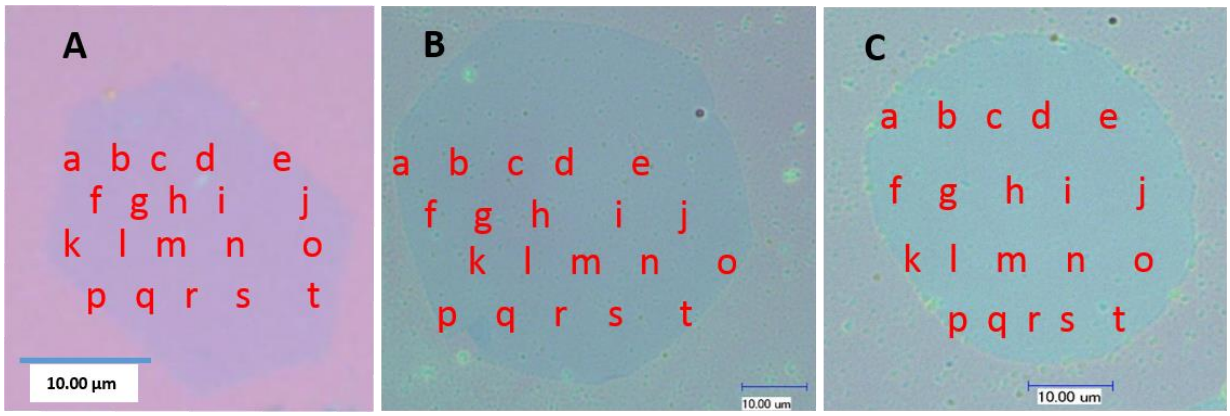

9. **Table A4.** Calculation of D/G and 2D/G peak ratio of Spectra in the crystal in fig A5 (A).

| Position of spectra | D-Peak height (au) | G-Peak height (au) | 2D-Peak height (au) | D/G peak Ratio | 2D/G peak Ratio |
|---|---|---|---|---|---|
| a | 26.33 | 256.54 | 557.54 | 0.1028 | 2.1777 |
| b | 9.19 | 239.76 | 539.65 | 0.0384 | 2.2507 |
| c | 4.21 | 262.99 | 601.94 | 0.0160 | 2.2888 |
| d | 9.03 | 230.56 | 547.04 | 0.0392 | 2.3727 |
| e | 8.09 | 238.62 | 553.35 | 0.0339 | 2.3189 |
| f | 12.20 | 249.15 | 551.87 | 0.0490 | 2.2150 |
| g | 6.47 | 254.94 | 550.31 | 0.0254 | 2.1585 |
| h | 4.84 | 232.82 | 529.69 | 0.0208 | 2.2751 |
| i | 5.06 | 240.47 | 550.77 | 0.0210 | 2.2904 |
| j | 5.33 | 249.44 | 561.06 | 0.0214 | 2.2493 |
| k | 5.57 | 245.55 | 523.82 | 0.0227 | 2.1333 |
| l | 5.29 | 253.54 | 530.82 | 0.0217 | 2.0936 |
| m | 3.49 | 218.07 | 466.82 | 0.0160 | 2.1407 |
| n | 4.17 | 231.05 | 523.15 | 0.0181 | 2.2642 |
| o | 5.12 | 247.51 | 514.39 | 0.0207 | 2.0783 |
| p | 6.35 | 243.71 | 545.16 | 0.0261 | 2.2369 |
| q | 20.06 | 243.57 | 552.93 | 0.0824 | 2.2701 |
| r | 5.60 | 243.88 | 526.84 | 0.0230 | 2.1602 |
| s | 4.11 | 244.37 | 542.06 | 0.0168 | 2.2182 |
| t | 5.03 | 252.75 | 507.85 | 0.0199 | 2.0093 |
| Average | | | | 0.0317 | 2.2101 |

10. **Table A5.** Calculation of D/G and 2D/G peak ratio of Spectra in the crystal in fig A5 (B).

| Position of spectra | D-Peak height (au) | G-Peak height (au) | 2D-Peak height (au) | D/G peak Ratio | 2D/G peak Ratio |
|---|---|---|---|---|---|
| a | 8.19 | 141.45 | 459.02 | 0.0579 | 3.2451 |
| b | 8.97 | 153.55 | 461.19 | 0.0584 | 3.0035 |
| c | 7.00 | 153.55 | 463.42 | 0.0457 | 3.0345 |
| d | 19.27 | 149.62 | 436.30 | 0.1288 | 2.9161 |
| e | 5.47 | 163.94 | 421.71 | 0.0333 | 2.5724 |
| f | 10.71 | 202.89 | 404.43 | 0.0528 | 1.9933 |
| g | 8.72 | 168.73 | 412.28 | 0.0517 | 2.4434 |
| h | 8.56 | 169.29 | 394.39 | 0.0506 | 2.3297 |
| i | 14.96 | 170.31 | 408.85 | 0.0879 | 2.4007 |
| j | 6.32 | 166.41 | 391.19 | 0.0380 | 2.3508 |
| k | 6.71 | 167.37 | 390.72 | 0.0401 | 2.3345 |
| l | 7.25 | 169.94 | 397.81 | 0.0427 | 2.3409 |
| m | 11.44 | 148.24 | 386.90 | 0.0772 | 2.6100 |
| n | 6.75 | 167.41 | 395.53 | 0.0404 | 2.3627 |
| o | 8.82 | 173.90 | 405.49 | 0.0507 | 2.3317 |
| p | 5.70 | 172.46 | 386.84 | 0.0331 | 2.2431 |
| q | 11.66 | 151.94 | 488.04 | 0.0767 | 2.9488 |
| r | 7.42 | 157.77 | 405.91 | 0.0470 | 2.5728 |
| s | 7.34 | 157.05 | 416.56 | 0.0468 | 2.6525 |
| t | 6.61 | 171.10 | 393.08 | 0.0386 | 2.2974 |
| Average | | | | 0.0549 | 2.5492 |

11. **Table A6.** Calculation of D/G and 2D/G peak ratio of Spectra in the crystal in fig A5 (C).

| Position of spectra | D-Peak height (au) | G-Peak height (au) | 2D-Peak height (au) | D/G peak Ratio | 2D/G peak Ratio |
|---|---|---|---|---|---|
| a | 123.00 | 2037.03 | 6620.49 | 0.0600 | 3.0200 |
| b | 84.02 | 2090.32 | 6596.06 | 0.0400 | 3.1500 |
| c | 85.06 | 2068.95 | 6911.76 | 0.0400 | 3.3400 |
| d | 237.22 | 2071.31 | 6719.31 | 0.1100 | 3.0240 |
| e | 86.11 | 2107.95 | 6664.94 | 0.0400 | 3.1600 |
| f | 73.22 | 1967.85 | 6661.55 | 0.0370 | 3.3800 |
| g | 70.35 | 2137.13 | 6097.07 | 0.0330 | 2.8500 |
| h | 130.19 | 2106.54 | 6321.04 | 0.0610 | 3.0007 |
| i | 76.97 | 2177.30 | 6904.94 | 0.0350 | 3.1710 |
| j | 170.23 | 2152.20 | 6718.25 | 0.0790 | 3.1200 |
| k | 207.79 | 2107.92 | 6565.71 | 0.0980 | 3.1140 |
| l | 89.38 | 2058.46 | 6368.83 | 0.0430 | 3.0930 |
| m | 51.75 | 2170.98 | 6048.15 | 0.0240 | 2.7850 |
| n | 122.17 | 2109.86 | 6433.83 | 0.0580 | 3.0490 |
| o | 138.19 | 2165.16 | 6602.20 | 0.0640 | 3.0490 |
| p | 141.16 | 2056.31 | 6455.67 | 0.0680 | 3.3190 |
| q | 47.84 | 2267.83 | 6468.70 | 0.0210 | 2.8520 |
| r | 140.46 | 2126.67 | 6519.18 | 0.0660 | 3.0650 |
| s | 97.03 | 2123.48 | 6751.75 | 0.0457 | 3.1760 |
| t | 98.59 | 2181.38 | 6915.42 | 0.0450 | 3.1700 |
| Average | | | | 0.0534 | 3.0944 |

12. **Figure A6**: (a) Mo-CNF converted to (b) graphitic structure under application of bias. (c) EDS measurement taken around the circled area of Fig (b) showing almost no presence of W of **chapter 4**.

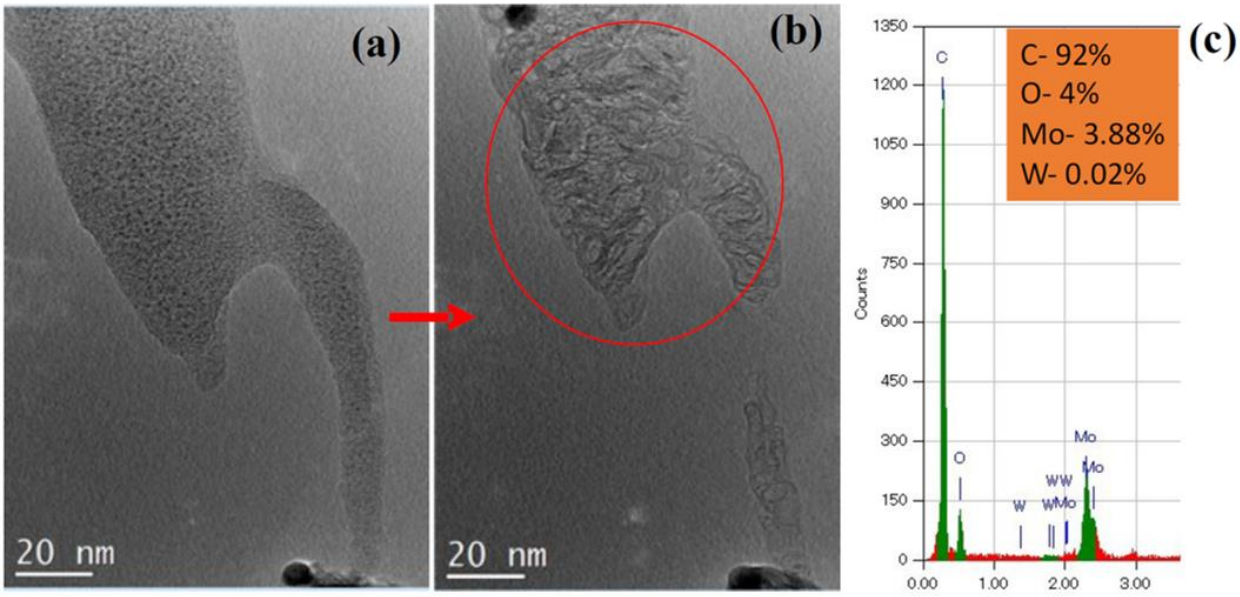

# List of the Publications

1. G. Kalita, M. D. Shaarin, **B. Paudel**, R. Mahyavanshi and M. Tanemura; Temperature dependent diode and photovoltaic characteristics of graphene-GaN heterojunction, *Appl. Phys. Lett*., 2017, **111**, 013504 (5pp).
2. S. Sharma, **B. Paudel Jaisi**, K. P. Sharma, M. I. Araby, G. Kalita and M. Tanemura; Synthesis of Freestanding WS2 Trees and Fibers on Au by Chemical Vapor Deposition (CVD), *Phys. Status Solidi A*, 2018, **215**, 1700566 (4pp).
3. K. P. Sharma, S. Sharma, A. Khaniya Sharma, **B. Paudel Jaisi**, G. Kalita and M. Tanemura; Edge controlled growth of hexagonal boron nitride crystals on copper foil by atmospheric pressure chemical vapor deposition, *CrystEngComm*., 2018, **20**, 550-555.
4. **B. Paudel Jaisi**, K. P. Sharma, S. Sharma, R. D. Mahyavanshi, G. Kalita and M. Tanemura; switching isotropic and anisotropic graphene growth in a solid source CVD system, *CrystEngComm.*, 2018, **20**, 5356-5363.
5. S. Sharma, **B. Paudel Jaisi**, M. I. Araby, S. Elnobi, M. E. Ayhan, G. Kalita and M. Tanemura; The Mo catalyzed graphitization of amorphous carbon: an in situ TEM study, *RSC Adv*., 2019, **9**, 34377-34381.
6. S. Elnobi, S. Sharma, M. I. Araby, **B. Paudel**, G. Kalita, M. Z. M. Yusop, M. E. Ayhan and M. Tanemura; Room-temperature graphitization in a solid-phase reaction, *RSC Adv.*, 2020, **10**, 914-922.
7. S. Sharma, T. Osugi, S. Elnobi, S. Ozeki, **B. Paudel Jaisi**, G. Kalita, C. Capiglia and M. Tanemura; Synthesis and Characterization of Li-C Nanocomposite for Easy and Safe Handling, *Nanomater.*, 2020, **10**, 1483 (8pp).

8. **B. Paudel Jaisi**, S. Sharma, S. Elnobi, A. A. Abuelwafa, Y. Yaakob, G. Kalita and M. Tanemura; Graphitization of Gallium-Incorporated Carbon Nanofibers and Cones: In Situ and Ex Situ Transmission Microscopy Studies, *Phys. Status Solidi B*, 2020, **257**, 2000309 (5pp).
9. S. Elnobi, S. Sharma, T. Oshugi, **B. Paudel**, G. Kalita, M. Z. M. Yusop, M. E. Ayhan, Z. Q. C. Ng, D. H. C. Chua and M. Tanemura; One-step synthesis of spontaneously graphitized nanocarbon using cobalt-nanoparticles, *SN Appl. Sci*., 2020, **2**, 2147 (7pp).

# List of Conferences

1. **Balaram Paudel Jaisi**, Golap Kalita and Masaki Tanemura; Effect of carrier gases flow rate on isotropic and anisotropic growth of graphene crystals by chemical vapor deposition, (Oral), *JSAP 65$^{th}$ Spring meeting*, Waseda University, Tokyo, Japan, Mar. 17-21, 2018.
2. **Balaram Paudel Jaisi**, Kamal Prasad Sharma, Subash Sharma, Rakesh D. Mahyavanshi, Golap Kalita and Masaki Tanemura; Tuning isotropic and anisotropic graphene growth in a solid source Chemical Vapor Deposition (CVD) with carrier gases flow rate, (Oral), *International Conference for Leading and Young Materials Scientists (IC-LYMS 2018)*, Zhuhai, China, Dec. 23-26, 2018.
3. **Balaram Paudel Jaisi**, Subash Sharma, Golap Kalita and Masaki Tanemura; Observation of graphitization of Gallium incorporated Carbon Nanofibers and cones under In-situ TEM and their I-V characteristics, (Oral), *JSAP 80$^{th}$ Autumn meeting*, Hokkaido University, Sapporo, Japan, Sep. 18-21, 2019.

# List of Figures

# List of Tables